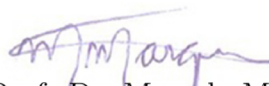Dissertation presented to the Instituto Tecnológico de Aeronáutica, in partial fulfillment of the requirements for the degree of Master of Science in the Graduate Program of Physics, Field of Atomic and Molecular Physics.

Fernando Valadares Calheiros de Siqueira

COMPOSITIONAL TUNING OF PEROVSKITE SYSTEMS FOR PHOTOVOLTAICS: AN *AB INITIO* STUDY

Dissertation approved in its final version by signatories below:

Prof. Dr. Marcelo Marques
Advisor

Prof. Dr. Pedro Teixeira Lacava
Pro-Rector of Graduate Courses

Campo Montenegro
São José dos Campos, SP - Brazil
2020

COMPOSITIONAL TUNING OF PEROVSKITE SYSTEMS FOR PHOTOVOLTAICS: AN *AB INITIO* STUDY

Fernando Valadares Calheiros de Siqueira

Thesis Committee Composition:

Prof. Dr.	Rene Felipe Keidel Spada	Chairperson	-	ITA
Prof. Dr.	Marcelo Marques	Advisor	-	ITA
Prof. Dr.	André Jorge Carvalho Chaves	Internal Member	-	ITA
Dra.	Ana Flávia Nogueira	External Member	-	Unicamp

ITA

Acknowledgments

Things were much different six months ago when I wrote the Acknowledgements section of my undergraduate thesis. Specifically, there wasn't a pandemic obliging anyone to lockdown inside their houses. Despite all related complications, our group hasn't stopped working or scheduling meetings to discuss this research. I want to express gratitude to my professors Marcelo Marques, Lara Teles, and Ivan Guilhon. Your efforts for teaching and research are yet to find boundaries.

I also want to thank everyone who welcomed me back home after so many years. I had lots of fun and company with Alícia, Daniel and so many old and new friends in Recife. In my family, I found the guidance and care that were essential to the conclusion of this dissertation. My mother, grandmother, and sister share the same passions for the studies than I and have always given me full support for achieving my objectives. Even when these require me to be away.

At last, I thank CAPES for the financial support.

*"Pleasure to me is wonder —
the unexplored, the unexpected, the thing that is hidden
and the changeless thing that lurks behind superficial mutability"*
— HOWARD PHILLIPS LOVECRAFT

Resumo

Haletos de perovskita AMX_3 são semicondutores de alto interesse para aplicações foto-voltaicas, tendo mostrado células solares com eficiência de conversão luminosa comparável à da bem-estabelecida tecnologia de silício. No entanto, ainda há obstáculos na comercialização desses dispositivos, como a necessidade de estabilidade a longo prazo e aperfeiçoamento da absorção luminosa. Comumente, esses problemas são abordados com a substituição completa ou parcial dos elementos nas posições A, M e X da rede cristalina. Nesse trabalho, apresentamos cálculos *ab initio* de uma serie de perovskitas incluindo correção de quasipartícula DFT-1/2 e acoplamento spin-órbita. O objetivo principal é investigar o papel de cada elemento nas propriedades eletrônicas e estruturais e estabilidade de cada material. É reportado o cálculo de 48 perovskitas em fase cúbica (A = CH_3NH_3, $CH(NH_2)_2$, Cs, Rb; M = Pb, Sn, Ge, Si; X = I, Br, Cl), das quais 16 apresentam gap de banda adequados para células solares de junção única. As tendências de gap são então explicados metodicamente com base na rede, no caráter orbital das bandas e na magnitude do acoplamento spin-órbita. Três programas foram criados em Python para o cálculo de alto rendimento de ligas multinárias. Com base no conhecimento adquirido com células puras e nas soluções desenvolvidas, são reportados os cálculos das ligas $CsPb_{1-x}Sn_xI_3$ e $CsSn_{1-x}Ge_xI_3$. Em ambos os casos, a desordem estrutural, estabilidade de fase e a estrutura eletrônica são investigados. No primeiro caso, a forte não-linearidade na evolução do band gap é quantificada e explicada em termos de alinhamento de bandas. Na segunda liga, é observada uma transição contínua entre as simetrias romboédrica e cúbica, afetando diretamente a estabilidade de fase e o gap de banda. Em resumo, esse trabalho aborda sistemas de grande impacto na literatura e de difícil descrição teórica. Desenvolve-se um programa computacional avançado que reúne várias técnicas para a modelagem eficiente de materiais, comparável ao estado da arte. São fornecidos resultados em ótimo acordo com o experimento e previsões confiáveis de novas perovskitas, evidenciando os mecanismos físicos que regem o ajuste de composição dessa classe de semicondutores.

Abstract

AMX_3 halide perovskites are semiconductors of burgeoning interest for photovoltaic applications, showing solar cells with light conversion efficiencies comparable to the well-established silicon technologies. However, there still are challenges for the commercialization of those devices, including long-term stability and optimal optical absorption. These obstacles are commonly surpassed with the partial or complete substitution of the A, M and X site elements. In this work, we present *ab initio* calculations of a series of perovskite systems with DFT-1/2 quasiparticle and spin-orbit corrections. The ultimate objective is to evidence the role played by each composing element in the material's electronic structure, lattice geometry and stability. The calculation of 48 cubic halide perovskites (A = CH_3NH_3, $CH(NH_2)_2$, Cs, Rb; M = Pb, Sn, Ge, Si; X = I, Br, Cl) is reported, of which 16 materials present gaps suitable for integrating single-junction solar cells. The gap trends are methodically explained based on lattice geometry, orbital character, and spin-orbit magnitude. The formation of pyramidal MX_3 units was identified as the cause of unexpectedly broad gaps. Three Python programs were created for the high-throughput calculation of multinary alloys. Based on the knowledge acquired with pristine perovskites and using these computational solutions, the calculation of $CsPb_{1-x}Sn_xI_3$ and $CsSn_{1-x}Ge_xI_3$ alloys is reported. In both cases, the structural disorder, phase stability, band gap and band orbital character are obtained and correlated. In the first alloy, the peculiar bowing in the band gap evolution was quantified and explained in terms of band alignment. In the second case, it is observed a continuous transition from rhombohedral to cubic symmetries that affect both phase diagram and band gap evolution. In summary, this dissertation addresses systems of great impact and of sophisticated theoretical description. Aiming for and efficient modelling, the developed computational solutions unite many techniques comparable to the state-of-the-art. The results are in close agreement with experiment and thus provide reliable predictions on new perovskite systems, evidencing the underlying physical mechanisms of compositional engineering of this class of semiconductors.

List of Figures

List of Tables

List of Abbreviations and Acronyms

DFT	Density functional theory
VASP	Vienna *Ab initio* Simulation Package
GQCA	Generalized quasi-chemical approximation
PAW	Projector Augmented-Wave
SOC	Spin-orbit coupling
PSC	Perovskite solar cell
PV	Photovoltaic
VBM	Valence band maximum
CBM	Conduction band minimum
LDA	Local Density Approximation
GGA	Generalized Gradient Approximation

Contents

1 Introduction

The development of clean energy sources is a topic of worldwide interest, figuring between the United Nations Sustainable Development Goals. The ultimate objective is to mitigate the use of non-renewable sources such as fossil fuels, which have severe medium- and long-term impacts on the environment, economy, and human health. Global attention to the subject contributes to increasingly significant investments in the wind, biomass, solar energy, and others. Solar photovoltaic (PV) energy receives a significant share of this investment, amounting to 47% of the total in 2016 (RITCHIE; ROSER, 2020). Concomitantly, its yearly energy consumption has rocketed from 1.13 TWh in 2000 to 584.63 TWh in 2018, but still corresponds to 0.95% of the total.

Crystalline silicon is currently the most common technology for photovoltaic devices, early reports tracing back to 1941 (OHL, U.S. Patent 2443542, 27 May 1941). The following decades of development of semiconductor physics and novel fabrication techniques lead to a good comprehension of its functioning and efficiency. Polycrystalline and Monocrystalline silicon now reach solar-to-electric power conversion efficiencies (PCE) of 21.2% and 27.6%, respectively (NREL, Access date: 2020). However, the bad light absorption properties of silicon wafer-based cells sparked interest in the investigation of alternative materials, leading to the development of second and third-generation thin-film technologies (SAHOO *et al.*, 2018).

Kojima *et al.* (2009) reported the first perovskite solar cell (PSC). Composed of an absorptive layer of methylammonium lead iodide (MAPbI$_3$), it showed a PCE of 3.8%. Although initially low, it developed rapidly until reaching values of up to 25.2% a decade later, a position comparable to those of the well-established silicon technologies.

Even more impressive is the MAPbI$_3$ resistance to defects, a result of its high dielectric constant and low effective masses (YIN *et al.*, 2014). It can thus be manufactured with solution-processing techniques, much cheaper when compared to silicon wafer fabrication. The most common method is the spin-coating of perovskites, consisting of spraying a solution of the precursor materials onto a spinning substrate (ANSARI *et al.*, 2018). The high angular speed results in rapid evaporation of the solvents and deposition of the crystal, but it leads to high material waste since most of the solution spills out of the substrate.

Although it is useful for low production volumes, there is on-going development of roll-to-roll perovskite printing methods aiming at large-scale production and commercialization (SWARTWOUT *et al.*, 2019).

These promising characteristics were sufficient for arresting the attention of the solar photovoltaics community. Nevertheless, MAPbI$_3$-based devices still face major setbacks. They rapidly degrade under operating conditions: humidity, oxygen, and high temperatures cause it to decompose into the optically inactive PbI$_2$ (SALHI *et al.*, 2018). Also, lead is a toxic material, harmful for the environment and human health (BABAYIGIT *et al.*, 2016). There are thus many challenges to overcome before perovskite-based solar cells are commercially available.

In this scenario, the scientific community directs much effort towards the research of alternative halide perovskite compositions. These are semiconductors of general formula AMX$_3$, where X is a monovalent halogen anion, M is a divalent cation, and A is a monovalent cation. The lead metal is often substituted by other group-IV elements, most commonly Sn and Ge. Other halogens such as Br, Cl, and F can replace the iodine ion. The A cation, on the other hand, is much more versatile. It can be an organic molecule such as methylammonium (MA), formamidinium (FA) or guanidinium (GA), or an alkali metal such as Rb and Cs. Even larger molecules are possible, allowing the dimensionality reduction of the crystalline lattice (LIU *et al.*, 2020).

Such flexibility in composition offers a powerful tool for tuning the optoelectronic properties, as well as the possibility of bypassing stability and toxicity issues. All-inorganic Cs perovskites can reduce the thermal decomposition (KRISHNAMOORTHY *et al.*, 2015), Sn and Ge are promising candidates for lead-free solar cells without loss in performance (MUTALIB *et al.*, 2018), and halide ion exchange was proven useful for tuning the light absorption spectrum (YUAN *et al.*, 2015). Since effectively reaching optimal properties requires a profound understanding of these materials, many publications perform comprehensive theoretical studies on the band gap and structural properties on a large number of perovskites (GOESTEN; HOFFMANN, 2018; PRASANNA *et al.*, 2017; PISANU *et al.*, 2018).

The vast compositional space of perovskites can be further extended by mixing two or more materials, a technique known as alloying (ZARICK *et al.*, 2018). Alloying possibly produces materials with more suitable properties than those of its components. MAPb$_{1-x}$Sn$_x$I$_3$, for example, has minimum band gap value around x = 0.75 (HAO *et al.*, 2014), allowing the absorption of higher wavelengths than MASnI$_3$ or MAPbI$_3$ alone. MAPb(I$_{1-x}$Br$_x$) presents a significantly enhanced resistance to humidity even at small bromide inclusion (x = 0.20) (NOH *et al.*, 2013). The A cation control in FA$_{1-x}$Cs$_x$Pb$_{1-y}$Sn$_y$I$_3$ allows for phase selection and tuning of structural distortions in the lattice (PRASANNA *et al.*, 2017). The use of mixed systems is thus a promising approach for building practical perovskite solar cells, although they are much more complicated to study in both the

experimental and the theoretical sense.

This work aims to study the fundamentals of compositional engineering in perovskite systems for photovoltaic devices. The lattice geometry, thermodynamics, band gap, orbital character and relativistic effects in the bandstructure of pristine and mixed systems will be analyzed using *ab initio* methods. These intrinsic properties will be calculated, correlated, and discussed given previous literature. The results should shed light on the shared characteristics of perovskites and the particularities of each material.

Chapter 2 opens this text with a discussion of the theoretical and computational methodologies. The calculations performed in this work utilize the density functional theory (DFT) (KOHN; SHAM, 1965), a quantum mechanical formulation that simplifies the description of the ground state of many-body systems. The application of these methods to periodic systems such as the perovskite crystals will be explained. Moreover, the Generalized Quasi-Chemical Approximation (GQCA) is used to extend the tools applicable to crystals to crystalline alloys (SHER *et al.*, 1987). This method provides information on the entire range of mixtures x, on the contrary to more conventional methods.

The combination of DFT and GQCA for the *ab initio* calculation of semiconductor alloys have long been used by the Group of Semiconductor Materials and Nanotechnology at the Aeronautics Institute of Technology. Despite the accumulated expertise, no unified and automatized solution had yet been developed for the group. Through the course of this dissertation, three programs were developed in Python for performing high-throughput alloy calculations. These were designed to contemplate alloys with arbitrary lattice and composition, as well as significantly reduce human effort. A solution of the kind is even more critical for the study of complex systems such as mixed perovskites. Calculations of such systems are of high computational costs, for they require the consideration of spin-orbit coupling (SOC), band gap quasiparticle correction, and cells with a large number of atoms, often comprising rotating molecules. Without the aid of algorithms, this becomes an extenuating task. The programs, briefly described in Section 2.3, are also expected to be of use for future works of the group on diverse alloyed systems.

The study of perovskite systems starts with the calculation of 48 cubic perovskites AMX_3 with composition A = MA, FA, Cs, Rb; M = Pb, Sn, Ge, Si; and X = I, Br, Cl, as detailed in Chapter 3. This selection covers the most common compositions for PV cells. It also includes the less studied rubidium- and silicon-containing perovskites, making predictions on their electronic structure. All materials were calculated in the cubic (α) phase for allowing the proper comparison between different compositions, while still offering meaningful information on other possible phases. The trends in band gap are explained in terms of orbital interaction and structural deformation, as well as chemical factors such as halogen electronegativity. The gap values obtained are used to propose possible materials for constituting the absorptive layer in single-junction cells.

Based on the knowledge acquired, some perovskites were selected for the study of their alloys. Chapter 4 reports the account of cubic $CsPb_{1-x}Sn_xI_3$, quantifying its phase stability, oxidation resistance, and band gap. Tin-lead perovskites are notorious for their very accentuate gap bowing, resulting in intermediate compositions ($x \approx 0.75$) having a lower band gap than those of the end components. This interesting effect is not yet fully understood, and this study seeks to provide further insights into the topic.

In Chapter 5, $CsSn_{1-x}Ge_xI_3$ is studied. This perovskite is exceptionally stable and relatively efficient at $x = 0.5$ (CHEN *et al.*, 2019). Since it has only recently been discovered as a promising material for lead-free solar cells, there is no detailed composition-dependent study of this alloy in the literature to the best of the author's knowledge. Careful analysis of structural, thermodynamical, and electronic properties of this system are reported for the first time.

This dissertation offers many insights into the compositional engineering of perovskite materials for photovoltaics. Many mechanisms here described are transferable to analogous systems. It should serve as an introduction to band gap tuning, as well as a guide for future theoretical and experimental research. Also, the tools developed are expected to be useful for future studies on any mixed system.

2 Methodology

The objective of this chapter is to introduce the well-established theoretical principles and computational tools that will be addressed throughout this text. The first topic is Density Functional Theory (DFT) (KOHN; SHAM, 1965), a set of quantum mechanics theorems that go beyond the Schrödinger's equation and simplify the electronic structure calculation of many-body systems. Following, the application of DFT to crystalline systems is discussed. The Bloch's theorem simplifies the problem of finding the electronic states of a periodic potential, while the projector augmented wave method (PAW), as used by the Vienna *Ab initio* Simulation Package (VASP), eases the computational costs (BLöCHL, 1994; KRESSE; FURTHMüLLER, 1996). The DFT-1/2 method is presented as a way of correcting well-known errors in the bandstructure of semiconducting crystals (FERREIRA *et al.*, 2008; FERREIRA *et al.*, 2011). In the third and last section, it is explained how the methods developed for perfectly periodic systems can be useful for quantifying properties of crystalline alloys, which are periodic in structure but disordered in atomic composition. Three programs were written in Python code, namely *autoalloy.py*, *simclusters.py* and *MGQCA.py*, with the objective of fully automating the application of these tools to the *ab initio* calculation of alloys.

2.1 Density Functional Theory

The physics of quantum mechanics stems from Schrödinger's equation. It determines the time evolution of any given state, represented by a vector $|\Psi(t)\rangle$ in Hilbert's space, of a system described by the hamiltonian operator $\hat{H}$:

$$\hat{H}\,|\Psi(t)\rangle = i\hbar\frac{\partial}{\partial t}\,|\Psi(t)\rangle\,. \tag{2.1}$$

The quantum hamiltonian $\hat{H}$ is an hermitian operator (assumed to be independent of time) directly related to the system's classical hamiltonian H. The quantization process consists in substituting the canonical conjugated pairs of variables of the system by pairs of operators associated to the degrees of freedom. The general solution to Eq. 2.1 can be

expressed as

$$|\Psi(t)\rangle = e^{-\frac{i}{\hbar}\hat{H}(t-t_0)} |\Psi(t_0)\rangle \,, \tag{2.2}$$

where the exponential is an unitary operator also refered to as the propagator $U(t - t_0)$. An interesting case happens when $|\Psi(t_0)\rangle$ is an eigenvector of $\hat{H}$ with eigenvalue E, in which case it is also an eigenvector of $U(t - t_0)$ with eigenvalue $\exp\{-iE(t - t_0)/\hbar\}$ and, therefore, evolves in time following a simple relation:

$$\hat{H}|\Psi(t_0)\rangle = E|\Psi(t_0)\rangle \rightarrow |\Psi(t)\rangle = U(t - t_0)|\Psi(t_0)\rangle = e^{-\frac{i}{\hbar}E(t-t_0)}|\Psi(t_0)\rangle \,. \tag{2.3}$$

The state of the system thus evolves with a phase shift. The eigenvalue E, correspondent to the energy of the state, is constant with time. These are thus known as the stationary states.

The standard problem of quantum mechanics is to obtain the electronic structure described by the set of pairs of stationary states and energies $\{|\Psi_E\rangle, E\}$. Any arbitrary state can then be written as a linear combination of the basis $\{|\Psi_E\rangle\}$, and the expression 2.2 can be calculated directly. Analogously to classical mechanics, the solution is obtained by (i) defining the hamiltonian $\hat{H}$ that suitably describes the physical system of interest and (ii) solving the time-independent Schrödinger's equation (2.3).

Although simple to state, the process of obtaining the electronic structure easily becomes an excruciating task. If, for example, the state $|\Psi\rangle$ describes a number N of interacting electrons, Eq. 2.3 translates into a nonlinear partial differential equation with 3N independent variables. For N of the order of Avogadro's number, even numerical approximations are well beyond any computing power currently available. Due to this difficulty, the methods involving many-body systems focus on finding an alternative hamiltonian that will simplify the solution and give information on the original system. This is the role of the density functional theory.

DFT is founded on the theorems proved by Hohenberg and Kohn (1964) that establish the importance of the electron density to the ground state of a system. The first theorem establishes a biunivocal relationship between an external potential V_{ext} applied to the system and the corresponding ground-state (GS) density ρ_0 of the solution $|\Psi_{E_0}\rangle$, where E_0 is the lowest possible energy a state can occupy. For the non-degenerate case, any given V_{ext} will generate a single ground-energy state $|\Psi_{E_0}\rangle$ as solution of (2.3), which in turn has a unique electronic density given by

$$\rho_0(\vec{r}) = \langle\Psi_{E_0}|\sum_{j=1}^{N} \delta(\vec{r} - \vec{r}_j)|\Psi_{E_0}\rangle \,. \tag{2.4}$$

The $\vec{r}_j$ variables represent the positions of each particle. Hohenberg and Kohn prove that

the opposite path is also true. That is, if $\rho(\vec{r})$ is the ground state solution of a given external potential V_{ext}^1 (and is, therefore, v-representable), no other potential V_{ext}^2 that differs from V_{ext}^1 by more than a constant value can generate the same GS density $\rho(\vec{r})$.

The consequence of the first theorem is that all information regarding the ground state is included in the electronic density. The external potential, as well as the electronic state, are functionals $V_{ext}[\rho_0]$ and $|\Psi[\rho_0]\rangle$. The expected value of any observable $\hat{O}$ can be written as a functional of density

$$\left\langle \hat{O} \right\rangle [\rho] = \langle \Psi[\rho]|\hat{O}|\Psi[\rho]\rangle. \tag{2.5}$$

Similarly, for a given system's hamiltonian $\hat{H}$ there exists a functional of energy $E[\rho] = \langle \Psi[\rho]|\hat{H}|\Psi[\rho]\rangle$, whose domain is the set of v-representable density functions.

The second Hohenberg-Kohn (HK) theorem proves that the minimum value of the functional $E[\rho]$ is obtained for the system's ground-state density ρ_0. That is:

$$E[\rho] = \langle \psi[\rho]|\hat{H}|\psi[\rho]\rangle \geq \langle \psi[\rho_0]|\hat{H}|\psi[\rho_0]\rangle = E[\rho_0] = E_0. \tag{2.6}$$

Now suppose one wants to obtain the ground state energy and electronic density of a system described by the hamiltonian $\hat{H}$. One option is to solve Equations 2.3 and 2.4. The alternative route is to obtain the system's functional $E[\rho]$ and minimize it with respect to ρ.

The HK theorems show that the energy is a functional of density and that it is possible to use it to obtain the ground-state properties of a system. However, they offer no practical method for doing so, and the general form of the functional $E[\rho]$ is unknown. It can be decomposed as

$$E[\rho] = T[\rho] + U_{ee}[\rho] + V[\rho], \tag{2.7}$$

where T, U_{ee} and V are respectively the kinectic, electron-electron interaction and potential energies. The potential energy can be written as the simple relation

$$V[\rho] = \int V(\vec{r})\rho(\vec{r})d^3r. \tag{2.8}$$

The U_{ee} term, on the other hand, is partly composed of the classical coulombic energy (also known as Hartree energy), which is given by

$$J[\rho] = \frac{1}{2} \int \int \frac{\rho(\vec{r})\rho(\vec{r'})}{|\vec{r} - \vec{r'}|} d^3r d^3r'. \tag{2.9}$$

The remaining interaction energy $U_{ee} - J$, along with the kinectic energy T, does not

count with an explicit expression in terms of ρ.

The method proposed by Kohn and Sham (1965) intends to treat separately the unknown functionals from those for which an exact description is available. This method leads to eigenvalue problems much simpler to solve than time-independent Schödinger's equation (2.3). It begins by substituting the N-electron state $|\Psi\rangle$ by a fictitious state of uncorrelated electrons $|\Psi_f\rangle$. This alternative state can be written as the tensor product of N one-electron states $|\Psi_f\rangle = |\psi_1\rangle \bigotimes |\psi_2\rangle ... \bigotimes |\psi_N\rangle$. Both states are required to have the same electronic density. If each state $|\psi_j\rangle$ is represented by a wavefunction in real space $\psi_j(\vec{r})$, its electronic density can be written, according to 2.4 in the simplified form

$$\rho(\vec{r}) = \sum_{j=1}^{N} |\psi_j(\vec{r})|^2. \tag{2.10}$$

The kinetic energy of uncorrelated states are, in fact, much simpler to calculate. It is expressed as the sum of kinetic energies of the one-electron states:

$$T_f = \sum_{j=1}^{N} T_{f,j} = -\frac{\hbar^2}{2m} \sum_{k=1}^{N} \int \psi_j^*(\vec{r}) \nabla_j^2 \psi_j(\vec{r}) d^3r. \tag{2.11}$$

The kinetic energy of the original system $T[\rho]$ can then be written as a sum of the kinetic energy T_f of the fictitious uncorrelated system and the remaining $T[\rho] - T_f$. The so-called exchange-correlation functional is then defined as

$$E_{xc} = (T - T_f) + (U_{ee} - J), \tag{2.12}$$

and Eq. 2.7 can be rewritten as

$$\begin{aligned}
E[\rho] =& T_f + J + V + E_{xc} \\
=& -\frac{\hbar^2}{2m} \sum_{j=1}^{N} \int \psi_j^*(\vec{r}) \nabla_j^2 \psi_j(\vec{r}) d^3r + \frac{1}{2} \int \int \frac{\rho(\vec{r})\rho(\vec{r}')}{|\vec{r} - \vec{r}'|} d^3r d^3r' \\
&+ \int V(\vec{r})\rho(\vec{r}) d^3r + E_{xc}[\rho],
\end{aligned} \tag{2.13}$$

with $E_{xc} = (U_{ee} - J) + (T[\rho] - T_f)$. In exception for E_{xc}, every term can be written explicitly in terms of ρ and, consequently, in terms of the functions ψ_j. Following the second HK theorem, the ground-state energy and density can be obtained by minimizing the energy functional while obeying the constraint of a fixed number N of electrons. This minimization reads as

$$\delta \left(E[\rho] - \mu \left(\int \rho(\vec{r}) d^3r - N \right) \right) = 0, \tag{2.14}$$

where μ is a lagrange multiplier. Assuming the existence of the functional derivative $\epsilon_{xc}(\vec{r}) = \delta E_{xc}/\delta\rho(\vec{r})$ and proceeding with the variational calculations, one arrives at the Kohn-Sham equations

$$\left[-\frac{\hbar^2}{2m}\nabla_j^2 + V_{KS}(\vec{r}) \right] \psi_j = \mu\psi_j, \; j = 1, ..., N. \tag{2.15}$$

The Kohn-Sham equations constitute an eigenvalue problem at first sight similar to the time-independent Schrödinger's equation 2.3, with the N-particle state being substituted by a one-particle wavefunction. However, for (2.15), the hamiltonian itself depends on the electronic density ρ. The effective Kohn-Sham potential V_{KS} substitutes the actual potential energy experienced by the electrons in the system, being

$$V_{KS} = V(\vec{r}) + \frac{1}{2} \int \frac{\rho(\vec{r})}{|\vec{r} - \vec{r'}|} d^3r' + \epsilon_{xc}. \tag{2.16}$$

The method to solve KS equations must, therefore, be self-consistent. The steps are (1) assuming an initial trial electronic density, (2) calculating the corresponding V_{KS}, (3) obtaining a set of one-electron orbitals with Equation 2.15, (4) calculating the new electronic density with Equation 2.10, and repeating the process from (2) until some convergence criteria are met. The Projector Augmented-wave method (PAW), discussed in the next section, is a common technique for solving the Kohn-Sham equations.

The problem is thus entirely reduced to the determination of the exchange-correlation term, and there are many alternatives available in the literature (see, for example, Filippi *et al.* [1994]). The simplest form of obtaining ϵ_{xc} is approximating the energy of the real system by that of an electron gas with the same local density, method known as the Local Density Approximation (LDA) (KOHN; SHAM, 1965). The Generalized Gradient Approximation (GGA) tries to improve on LDA, taking into consideration the first-order variations on the density:

$$E_{xc}^{GGA} = \int f(\rho(\vec{r}, \nabla\rho(\vec{r}))d^3r. \tag{2.17}$$

There are many possible formulations for the GGA functional, and the publication by Espíndola *et al.* (2015) provides a good introduction to the topic. The DFT calculations done in this work use the version developed by Perdew, Burke and Ernzerhof (PBE-GGA) (PERDEW *et al.*, 1996).

Another important physical result obtained by the Kohn-Sham equations is the orbital occupation energy, given by the orbital's Lagrange multiplier $\mu = \epsilon_j$. Janak's theorem (JANAK, 1978) states that the total energy of the system (2.13) is affected by the occu-

pation of the k-th orbital f$_j$ by a rate

$$\frac{\partial E}{\partial f_j} = \epsilon_j(f_j). \tag{2.18}$$

The occupation f$_j$ is unitary when the orbital is completely occupied and null when completely unoccupied, possibly assuming values in-between. In Section 2.2.2, it will be shown how it is possible to take advantage of Janak's theorem to improve upon the DFT predictions on semiconductor's band gaps.

2.2 Electronic structure calculations in crystals

The theories discussed above are general and can be applied to a myriad of systems. This work is concerned with the study of the particular case of crystalline alloys. Before understanding disordered systems, though, it is first necessary to discuss how the Kohn-Sham equations are solved for perfectly periodic crystalline structures.

2.2.1 Bloch's theorem

Crystals are defined by the spatial repetition of identical cells. These primitive cells contain the atoms that make up the crystal's composition. The cell edges are known as the primitive lattice vectors $\{\vec{R}_j\}$, which define the spatial periodicity. For tridimensional crystals, there are three linearly independent lattice vectors. Since the atomic arrangement is periodic, it is natural that the potential energy $V(\vec{r})$ at any point in the crystal lattice also shares this property:

$$V(\vec{r}) = V(\vec{r} - n_1\vec{R}_1 - n_2\vec{R}_2 - n_3\vec{R}_3), \; n_1, n_2, n_3 \in \mathbb{Z}. \tag{2.19}$$

The values of $V(\vec{r})$ can be interpreted as the diagonal matrix elements of the potential energy operator $\hat{V}$ in the basis of position vectors $|\vec{r}\rangle$: $V(\vec{r}) = \langle\vec{r}|\hat{V}|\vec{r}\rangle$. Defining an arbitrary translation operator $\hat{R}$ with translation $\vec{a} = \sum_{j=1}^{3} n_j\vec{R}_j$, so that

$$\hat{R}|\vec{r}\rangle = |\vec{r} - \vec{a}\rangle, \tag{2.20}$$

the following conclusion is immediate:

$$\hat{R}\hat{V} - \hat{V}\hat{R} = [\hat{R}, \hat{V}] = 0. \tag{2.21}$$

The potential energy operator commutes with any translation operator following the crystal's periodicity. The same property is valid for the kinetic energy operator $\hat{T}$, since its

matrix elements $\langle \vec{r} | \hat{T} | \vec{r} \rangle$ do not depend on the value of $\vec{r}$. Therefore, for the hamiltonian of the crystal:

$$\hat{H} = \hat{T} + \hat{V} \rightarrow [\hat{R}, \hat{H}] = 0. \tag{2.22}$$

This commutation relation implies that the hamiltonian eigenstates $|\Psi_E\rangle$ are also eigenstates of $\hat{R}$. Expanding $|\Psi_E\rangle$ in terms of the position basis $|\vec{r}\rangle$ and using Equation 2.20:

$$
\begin{aligned}
\hat{R} |\Psi_E\rangle = \hat{R} \int \psi_E(\vec{r}) |\vec{r}\rangle \, d^3r &= \int \psi_E(\vec{r}) |\vec{r} - \vec{a}\rangle \, d^3r \\
&= \int \Psi_E(\vec{r} + \vec{a}) |\vec{r}\rangle \, d^3r = |\Psi_E^T\rangle ,
\end{aligned}
\tag{2.23}
$$

where $|\Psi_E^T\rangle$ is the translated electron state and

$$\hat{R} |\Psi_E\rangle = C |\Psi_E\rangle = |\Psi_E^T\rangle \rightarrow C\psi_E(\vec{r}) = \psi_E(\vec{r} + \vec{a}), \tag{2.24}$$

where C is the translation operator eigenvalue. Since both $|\Psi_E\rangle$ and $|\Psi_E^T\rangle$ are required to have the same norm, $|C|^2 = 1$ and C can be written as a phase factor $C = e^{i\theta_{\vec{a}}}$. For n successive translations in $\vec{a}$, the phase shifts add together as

$$\psi(\vec{r} + n\vec{a}) = e^{in\theta_{\vec{a}}} \psi(\vec{r}). \tag{2.25}$$

Defining the phase shifts due to translations by primitive lattice vectors $\vec{R}_1$, $\vec{R}_2$ and $\vec{R}_3$ as θ_1, θ_2 and θ_3, respectively, and further defining the vector $\vec{k} = \sum_{j=1}^{3} \theta_j \vec{R}_j / \left| \vec{R}_j \right|^2$, without loss in generality

$$\psi(\vec{r} + \vec{a}) = e^{i\vec{k}.\vec{a}} \psi(\vec{r}), \tag{2.26}$$

for any $\vec{a}$ given as a sum of integer multiples of the primitive lattice vectors. Notice that $\vec{k}$ is still arbitrary, and in that sense it indexes the different possible solutions that obey Eq. 2.26. Multiplying both sides by $\exp\left\{ -i\vec{k}(\vec{a} + \vec{r}) \right\}$:

$$e^{-i\vec{k}(\vec{r} + \vec{a})} \psi_{\vec{k}}(\vec{r} + \vec{a}) = e^{-i\vec{k}.\vec{r}} \psi_{\vec{k}}(\vec{r}) = u_{\vec{k}}(\vec{r}). \tag{2.27}$$

The quantity defined as the function $u_{\vec{k}}(\vec{r})$ is consequently invariant under any translation by lattice vectors. Any wavefunction of an electron placed in a periodic crystal must then have the form of the so-called Bloch wavefunction (BLOCH, 1929)

$$\psi_{\vec{k}}(\vec{r}) = e^{i\vec{k}\vec{r}} u_{\vec{k}}(\vec{r}). \tag{2.28}$$

The general solution of (2.15) should, therefore, have the form of (2.28). Taking Bloch's theorem into consideration, the problem of solving the Kohn-Sham equations for ψ in an

infinitely extended region of space simplifies to finding the form of $u_{\vec{k}}$ in a primitive cell. For each value of $\vec{k}$, there will be a discrete number of solutions $\psi_{n,\vec{k}}$ indexed by an integer n. The space of wavevector values (also known as kpoints), is known as the reciprocal space, which also possesses translational periodicity. The first Brillouin zone is the unit cell of reciprocal space, comprising all kpoints of physical interest.

The set of eigenvalues $E_{n,\vec{k}}$ obtained for the crystal constitutes its bandstructure, and the band gap of the crystal is the energy difference between the most energetic occupied orbital (the valence band maximum, VBM) and the less energetic unoccupied orbital (the conduction band minimum, CBM). Both concepts of bandstructure and band gap will be recurrent in this text. However, the density functional theory, as discussed in the last section, is designed for the study of ground-state properties. This leads to well-known errors in the determination of excited states. Band gap, an important parameter for solar cell design, is known to be systematically underestimated by the LDA functional. Next section, it will be shown how the DFT-1/2 method can correct this error, leading to gap values comparable to experiment with a low computational cost.

2.2.2   DFT-1/2 quasiparticle correction

Many approaches have been proposed with the objective of correcting the well-known DFT band gap underestimation, such as the GW approximation and hybrid funtional methods (HEDIN, 1999). Although accurate in many cases, both methods often come with a high computational cost even for simple crystalline systems. In the context of alloys and large supercells calculations, this cost becomes an impediment.

The DFT-1/2 method was developed in the Group of Semiconductor Materials and Nanotechnology by Ferreira, Marques, and Teles (2008, 2011) to fulfill this demand for a more efficient solution. It is based on the Slater's half-occupation scheme, which uses the eigenvalue of the valence band maximum after removing half electron as an approximation to the ionization energy of the molecule or solid. In this section, the general ideas and assumptions for extending Slater's idea to the density functional theory framework are discussed.

An immediate implication of Janak's theorem (2.18) is that

$$\frac{\partial E}{\partial f_\alpha} = \epsilon_\alpha \rightarrow E(1) - E(0) = \int_0^1 \epsilon_\alpha(f_\alpha)df_\alpha, \qquad (2.29)$$

where f_α represents the occupation of the orbital ψ_α, with value $f_\alpha = 1$ (0) when totally occupied (unoccupied). The Hellmann-Feynman theorem (FEYNMAN, 1939; HELLMANN,

1941) can be used to obtain the derivative of ϵ_α with respect to the occupation:

$$\frac{\partial \epsilon_\alpha}{\partial f_\alpha} = \frac{\partial}{\partial f_\alpha} \langle \psi_\alpha | \hat{H} | \psi_\alpha \rangle = \langle \psi_\alpha | \frac{\partial \hat{H}}{\partial f_\alpha} | \psi_\alpha \rangle = 2S_\alpha. \tag{2.30}$$

If the Kohn-Sham hamiltonian is used (2.15, 2.16) and the electron number density ρ is expanded in partial densities ρ_β associated with each atomic orbital β in the form $\rho = \sum_\beta f_\beta \rho_\beta$, the S$_\alpha$ coefficient is given by:

$$\begin{aligned}
S_\alpha = \int \int &\left[\frac{\rho_\alpha(\vec{r})\rho_\alpha(\vec{r'})}{|\vec{r}-\vec{r'}|} + \frac{1}{2}\rho_\alpha(\vec{r})\frac{\delta^2 E_{xc}}{\delta\rho(\vec{r})\delta\rho(\vec{r'})}\rho_\alpha(\vec{r'}) \right. \\
&\left. + \frac{\rho_\alpha(\vec{r})}{|\vec{r}-\vec{r'}|}\sum_\beta f_\beta \frac{\partial\rho_\beta(\vec{r'})}{\partial f_\alpha} + \frac{1}{2}\rho_\alpha(\vec{r})\frac{\delta^2 E_{xc}}{\delta\rho(\vec{r})\delta\rho(\vec{r'})}\sum_\beta f_\beta \frac{\partial\rho_\beta(\vec{r'})}{\partial f_\alpha} \right] d^3r d^3r'.
\end{aligned} \tag{2.31}$$

S$_\alpha$ is called the orbital self-energy due to the first term of Eq. 2.31. It is known that that ϵ_α is up to a good approximation a linear function of f$_\alpha$ (LEITE *et al.*, 1972), so the last two terms of (2.31) can be neglected. Under this consideration, a self-energy potential V$_S(\vec{r})$ can be defined as

$$S_\alpha = \int \rho_\alpha(\vec{r})V_S(\vec{r})d^3r \rightarrow V_S(\vec{r}) = \int \frac{\rho_\alpha(\vec{r'})}{|\vec{r}-\vec{r'}|}d^3r' + \frac{1}{2}\int \frac{\delta^2 E_{xc}}{\delta\rho(\vec{r})\delta\rho(\vec{r'})}\rho_\alpha(\vec{r'})d^3r'. \tag{2.32}$$

Back to Equation 2.30, the derivative of ϵ_α is approximately a constant value 2S$_\alpha$. Therefore, considering I$_\alpha$ as the ionization potential, Equation 2.29 results in

$$-I_\alpha = E(1) - E(0) = \int_0^1 \epsilon_\alpha(f_\alpha)df_\alpha = \epsilon_\alpha(1/2); \tag{2.33}$$

$$\epsilon_\alpha(1/2) = \epsilon_\alpha(0) + S_\alpha = \epsilon_\alpha(1) - S_\alpha. \tag{2.34}$$

These relations offer a direct way of calculating the ionization potential of an orbital given its half-occupancy energy. The band gap can actually be expressed in terms of ionization potentials of the CBM and VBM.

Consider the total energy as a function of the orbital occupancies E(f$_{CBM}$, f$_{VBM}$). The band gap of a crystal is the energy necessary to promote the electron at the VBM to the CBM:

$$\begin{aligned}
E_g = E(1,0) - E(0,1) &= (E(1,0) - E(0,0)) - (E(0,1) - E(0,0)) = -I_{CBM} + I_{VBM} \\
&= \epsilon_{CBM}(1/2) - \epsilon_{VBM}(1/2) = \epsilon_{CBM}(0) - \epsilon_{VBM}(1) + S_{CBM} + S_{VBM}.
\end{aligned} \tag{2.35}$$

Equation 2.35 tells us that the standard DFT band gap given by $\epsilon_{CBM}(0) - \epsilon_{VBM}(1)$ is

not exactly equal to the actual band gap E_g due to the self-energy terms $S_{CBM} + S_{VBM}$. But it can be obtained directly from the DFT band gap when considered half occupancy of both CBM and VBM.

Ferreira *et al.* also show how the half-occupancy can be calculated. Using Equations 2.32 and 2.34 for removing half electron from an occupied orbital:

$$
\begin{aligned}
\epsilon_\alpha(1/2) = \epsilon_\alpha(1) - S_\alpha &= \langle \psi_\alpha(1)|\hat{H}|\psi_\alpha(1)\rangle - \langle \psi_\alpha(1/2)|V_S|\psi_\alpha(1/2)\rangle \\
&\approx \langle \psi_\alpha(1/2)|\hat{H} - V_S|\psi_\alpha(1/2)\rangle .
\end{aligned}
\tag{2.36}
$$

The DFT-1/2 correction then consists in including the self-energy potential V_S to the Kohn-Sham hamiltonian in (2.15). The corrected Kohn-Sham equations are

$$
[-\frac{\hbar^2}{2m}\nabla_j^2 + V_{KS}(\vec{r}) - V_S(\vec{r})]\psi_j = \mu\psi_j, \; j = 1, ..., N.
\tag{2.37}
$$

However, this is problematic due to the charge disequilibrium induced by the removal of half an electron. In a crystal, the periodic addition of a $e/2$ charge causes the potential to diverge due to the coulombic interaction. To correct this problem, V_S is multiplied by a trimming function

$$
\Theta(r) = \begin{cases} [1 - (\frac{r}{CUT})^8]^3, \; r \leq CUT \\ \qquad 0, \; r > CUT \end{cases},
\tag{2.38}
$$

where CUT is a length parameter (henceforth expressed in atomic units) obtained variationally so to maximize the band gap.

The validity of the DFT-1/2 correction for halide perovskites has been previously discussed by Tao *et al.* (2017) for numerous systems, showing great correspondence to experiment and to other *ab initio* correction methods. Guedes *et al.* (2019a) later used this method for the study of the $MAPb_{1-x}Sn_xI_3$ mixed system. The DFT-1/2 correction will be applied for every band gap calculation presented in this text. The CUT parameter is obtained variationally for the primitive cells of the pure perovskites with a resolution of 0.05Å, with the removal of half electron from the halogen p orbital, which constitutes the top of the valence band. For $A(M_{1-x}M'_x)X_3$ alloys, the CUT adopted for all supercell calculations is the average $(CUT_{AMX_3} + CUT_{AM'X_3})/2$. The correction has a great transferability, so the CUT value for X_p is almost unaffected when the halogen is placed in different environments.

The accurate and efficient description of the electronic structure of crystals with density functional theory is now clearer. However, there are still many techniques used to ease down the computational effort. The projector augmented-wave method (PAW), for example, aims in transforming the Kohn-Sham wavefunctions ψ on related pseudofunctions $\tilde{\psi}$ that are more easily described with plane-wave expansion. This approach, used by the VASP software, is discussed in the following section.

2.2.3 Projector augmented-wave method

The computational description of the wavefunctions and electron densities in crystals often resorts to the plane wave basis. This representation involves several advantages due to its simplified implementation, fast calculation of Fourier transforms, and tractable convergence criteria. However, problems appear when describing electrons close to the atomic nucleus: due to the strong potential produced by the inner-shell electrons, the valence wavefunctions are highly oscillating. Such behavior requires a large number of plane waves to reach convergence, consequently raising memory and CPU requirements.

The solution proposed by the PAW method consists in finding a linear transformation $\hat{\mathcal{T}}$ that bridges the actual state $|\Psi_n\rangle$ and an auxiliary state $|\Phi_n\rangle$ whose pseudofunction presents a smoother behavior close to the nucleus:

$$|\Psi_n\rangle = \hat{\mathcal{T}} |\Phi_n\rangle, \tag{2.39}$$

which, using Eq. 2.15, leads to

$$\hat{\mathcal{T}}^\dagger \hat{H} \hat{\mathcal{T}} |\Phi_n\rangle = \epsilon_n \hat{\mathcal{T}}^\dagger \hat{\mathcal{T}} |\Phi_n\rangle. \tag{2.40}$$

This allows to calculate $|\Phi_n\rangle$ with efficiency using the transformed Kohn-Sham equations (2.40) and then retrieve the information of $|\Psi_n\rangle$ using $\hat{\mathcal{T}}$.

The atom-centered transformations $\hat{\mathcal{T}}^a$ are defined for each atomic orbital so that

$$|\Psi_n^a\rangle = (1 + \hat{\mathcal{T}}^a) |\Phi_n^a\rangle, \ \hat{\mathcal{T}} = (1 + \sum_a \hat{\mathcal{T}}^a), \tag{2.41}$$

where $|\Psi_n^a\rangle$ denotes each atomic orbital and $|\Phi_n^a\rangle$ their respective pseudo-orbitals. Since the sharpness of $|\Psi_n\rangle$ resides in the proximity to the nucleus, the linear transformations $\hat{\mathcal{T}}$ are meant to affect only the region inside a certain radius r_n^a, so the wavefunctions of $|\Psi_n^a\rangle$ and $|\Phi_n^a\rangle$ coincide outside this sphere. The total wavefunction and the respective pseudofunction are supposed to be linear superpositions of the atomic orbitals:

$$\psi_n(\vec{r}) = \sum_a c_n^a \psi_n^a(\vec{r}), \tag{2.42}$$

$$\phi_n(\vec{r}) = \sum_a c_n^a \phi_n^a(\vec{r}). \tag{2.43}$$

The expansion coefficients are equal as a requirement of the linear transformation in Eq.

2.41. Using Equations (2.41-2.43):

$$\begin{aligned}
|\Psi_n\rangle = \hat{\mathcal{T}}|\Phi_n\rangle &= |\Phi_n\rangle + \sum_a c_n^a \hat{\mathcal{T}}^a |\Phi_n^a\rangle \\
&= |\Phi_n\rangle + \sum_a c_n^a (|\Psi_n^a\rangle - |\Phi_n^a\rangle).
\end{aligned} \tag{2.44}$$

The transformation in Eq. 2.44 then consists in first removing the pseudofunction behavior $\sum_a c_n^a |\Phi_n^a\rangle$ from the proximities of the nuclei and then adding back the real orbital behavior given by $\sum_a c_n^a |\Psi_n^a\rangle$. Given the superposition shown in Eq. 2.43, the coefficients c_n^a are obtained by choosing proper projector functions $|p_n^a\rangle$ so that $\langle p_n^{a'}|\Phi_n^a\rangle = \delta_{a'a}$ and, consequently

$$c_n^a = \langle p_n^a | \Phi_n \rangle. \tag{2.45}$$

The result is that the linear transformation $\hat{\mathcal{T}}$ can be expressed in terms of the projector functions using Equations 2.44 and 2.45:

$$\hat{\mathcal{T}} = 1 + \sum_a (|\Psi_n^a\rangle - |\Phi_n^a\rangle) \langle p_n^a|. \tag{2.46}$$

The PAW formulation allows one to assume a frozen core approximation by excluding from the summation of $\hat{\mathcal{T}}$ the inner-shell orbitals, which do not interact strongly with their surroundings. The core wavefunctions are tabulated, and so the transformed Kohn-Sham equations are reduced to the calculation of the valence electrons. As the VASP software uses PAW, this method is applied to all calculations reported in this work.

From Bloch's theorem and the quasiparticle correction of the semiconductor band gap to the frozen-core approximation as implemented by the projector augmented-wave method, the proper application of density functional theory to semiconducting crystals is well outlined. In the following section, it will be explained how these theories can be expanded to describe crystalline alloys.

2.3 Developed solutions for the DFT study of crystalline alloys

The simplifications discussed so far for many-body problems rely especially on Bloch's theorem, which assumes the spatial periodicity of the system. The alloyed systems here reported, however, break this symmetry. When mixing two different semiconductors of formulas AMX_3 and $AM'X_3$, for example, there is, in principle, no order in the arrangement of the M ions. Moreover, M and M' interact differently with the environment, causing structural disorder as well.

Nonetheless, the behavior of semiconductor alloys is, in general, similar to that of their components. So, even though the translational symmetry is broken, some assumptions are still valid (CHEN; SHER, 1996). In fact, the electron and hole wavefunctions in semiconductors are often assumed to span over a large number of unit cells, which implies that these carriers are affected by a macroscopic average of the lattice interaction. The alloy itself can be approximated as a material with the average properties of the local disordered regions.

The intuitive approach for the theoretical description of alloys then consists in three steps: (i) defining the alloy's building blocks, the supercells (SC), that take into consideration the local disorder; (ii) calculating the electronic structure and physical properties of each SC using DFT; and (iii) utilizing a meaningful statistical method for determining the average property of the material. This section will briefly explain how each step is implemented. Three scripts were written in the Python programming language to solve each step, named *autoalloy.py*, *simclusters.py* and *MGQCA.py*, respectively. Their implementation and use are reported elsewhere (VALADARES, 2019).

2.3.1   Supercell expansion

The simplest way of inferring any property of a mixed system is to characterize its end components and interpolate their properties. Suppose one wants to study an $A_{1-x}B_x$ alloy, where A and B are different materials. One could simply run primitive cell calculations of both A and B, and, for a property P of any composition x,

$$P(x) = (1 - x)P_A + xP_B. \qquad (2.47)$$

This is an extremely crude approximation since it does not take into account the interactions between A and B that occur in the mixed material. In the real system, properties often do not evolve linearly.

The natural improvement for this model is to adopt larger cells (also referred to as supercells or clusters) in the DFT calculations, made up of stacking of primitive cells (PC). Suppose a supercell defined as containing N PCs. Mixed supercells can have N_A primitive cells of A and $N_B = N\text{-}N_A$ cells of B, thus having a corresponding $x = (N_B/N)$. The higher the N, the finer is the sampling of the compositional space $0 \leq x \leq 1$, and the more interactions and mixing disorder are taken into account. On the other hand, large values of N can lead to prohibitive computational costs.

There would be 2^N possible supercell configurations in the $A_{1-x}B_x$ system. The number of calculations, however, can be drastically reduced with symmetry considerations. Many of these cells, in fact, represent the same material, being related by the symme-

try operations of the crystal, such as translations, rotations, reflections, etc. Using the crystal's space group - the group of symmetry operations of a given crystal - the set of SC can then be divided into subsets of degenerate supercells. All cells belonging to the same group have the exact same properties, and only one representative cell must be calculated to characterize the rest. As an example, Figure 2.1 illustrates the 4 possible SC configurations for a $CsPb_{1-x}Sn_xI_3$ alloy with two primitive cells stacked in a crystalline direction. The two configurations at the right can be easily identified as being degenerate since one can be transformed onto another by a reflection operation. In this case, only three supercells must be calculated to characterize the system.
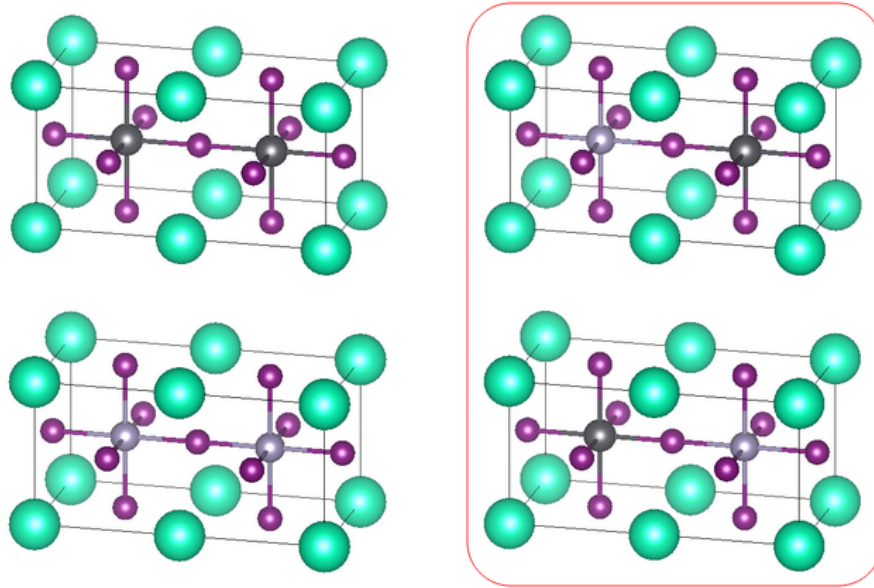
FIGURE 2.1 – Supercell configurations for $CsPb_{1-x}Sn_xI_3$ with N = 2. The highlighted cells are degenerate and connected by a reflection operation. Lead and tin ions are depicted in black and light gray, respectively.

The entire process of applying the symmetry operations and preparing the representative clusters for DFT calculations was implemented in the *autoalloy.py* program. It covers tridimensional crystalline alloys of arbitrary composition and lattice geometry, as well as arbitrarily-shaped supercells. Figure 2.2 exemplifies the input file for a wurtzite $Al_{1-x}Ga_xN$ alloy, with a supercell defined as a stacking of two layers in the first and second crystalline directions, totaling N = 4 PCs and 8 group-III atoms. The program uses the pymatgen Python library (ONG *et al.*, 2013) to find the space group of the defined lattice. In this example, the output reports 22 representative supercells, a number significantly lower than the $2^8 = 256$ possible configurations.

```
lattice constants:
AlN: 3.112
GaN: 3.178

stacking: 2 2 1

1.000000   0.000000   0.000000
0.500000   0.866026   0.000000
0.000000   0.000000   1.632993

0.000000   0.000000   0.000000 ; Al Ga
0.333333   0.333333   0.500000 ; Al Ga
0.000000   0.000000   0.375000 ; N
0.333333   0.333333   0.875000 ; N
```
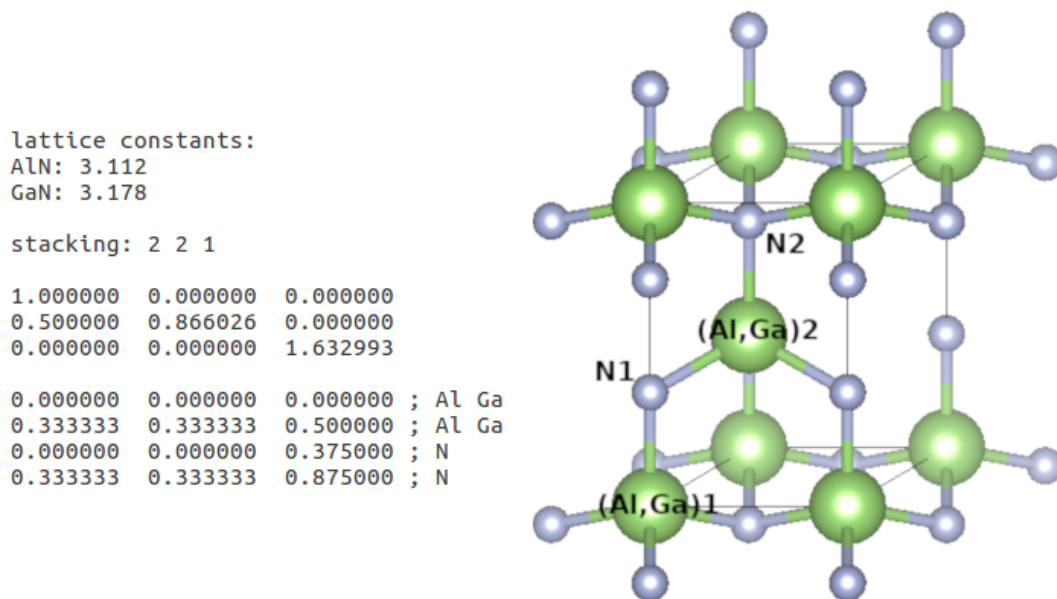
FIGURE 2.2 – Example of input file of the *autoalloy.py* program for defining the representative clusters of the $Al_{1-x}Ga_xN$ alloy.

2.3.2 Coordination of VASP runs

Once the representative cells have been obtained, it is then necessary to calculate the ground state of each using density functional theory. This task can be very demanding not only computationally but also to the operator, who needs to set-up, execute, and wait for the ending of multiple VASP runs for each supercell. The solution was to write the *simclusters.py* program, which is designed to be easy to use, adaptable to different systems, and robust to errors. It was designed to run in a machine that uses Slurm Workload Manager (YOO *et al.*, 2003) as a job scheduler for VASP executions and allows all calculations to be executed uninterruptedly.

The user may select a number of calculations to be performed for each cluster, such as (1) relaxation of atomic positions, calculation of (2) density of states, (3) band gap, (4) effective mass tensor, and (5) elastic constants. The code can be easily adapted to include more protocols such as dielectric function calculation and is compatible with the DFT-1/2 correction. Once these have been defined, the *simclusters.py* program builds a dynamical list of tasks (VASP runs) to be performed for each cluster, as seen in Figure 2.3. This task list is continuously revisited, and new tasks may be included during the run if the program identifies the necessity. The user may also define the parallel calculation of multiple alloys.

Once the electronic structure of the j-th supercell is calculated, a given property P_j (for example, band gap) can be obtained by reading VASP output files. Equation 2.47
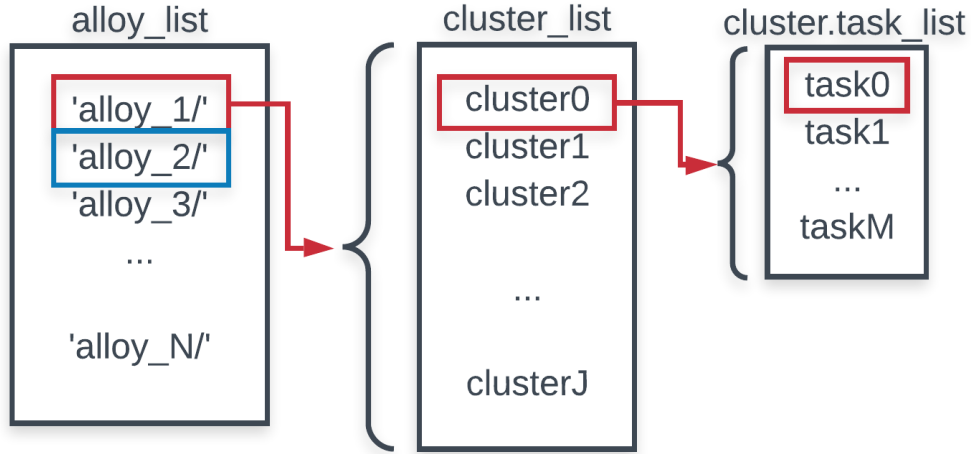
FIGURE 2.3 – Tasks list for each cluster of each alloy defined by the *simcluster.py* program for coordinating VASP calculations.

can then be upgraded to

$$P(x) = \sum_{j=0}^{J} x_j P_j, \tag{2.48}$$

where J + 1 is the number of representative supercells, and x_j is the probability of formation of the j-th cluster during the crystallization process. The set of probabilities x_j are governed by the ratio x of materials in the precursor solution, the formation energy of each supercell, and the fabrication temperature T of the alloy. The problem of determining these values is discussed in the following section.

2.3.3 Generalized quasi-chemical approximation

The Generalized quasi-chemical approximation (GQCA) is a statistical theory developed and reported by Sher *et al.* (1987) in the context of theoretical calculations of binary alloys. It has been applied to a variety of systems, including hybrid organic-inorganic perovskites (GUEDES-SOBRINHO *et al.*, 2019b; GUEDES-SOBRINHO *et al.*, 2019a), III-nitrides (MARQUES *et al.*, 2003), and zinc oxides (ATAÍDE, 2016).

The third and final program developed, named *MGQCA.py*, aims at defining and solving the equations for the probabilities x_j. The abbreviation stands for Multinary GQCA since the original GQCA formulation for binary alloys is extended for multinary mixed systems. Moreover, it acts as a post-processing tool of VASP outputs, retrieving the P_j properties of all clusters.

The GQCA formulation consists in modelling the fabrication of the alloy $A_{1-x}B_x$ as occurring in an environment with an infinite source of atoms. The composition of this

precursor solution comes from the composition of A and B and follows a proportion determined by x. Suppose the supercell formation energies ϵ_j, with $\epsilon_0 = \epsilon_A$ and $\epsilon_J = \epsilon_B$. Suppose also the formation probabilities x_j, yet unknown. They must follow the constraints

$$xN = \sum_{j=0}^{J} x_j N_{B,j}, \ \sum_{j=0}^{J} x_j = 1, \tag{2.49}$$

where $N_{B,j}$ is the number of B primitive cells in the j-th supercell.

The mixing energy of the alloy is defined as the difference in energy necessary for the crystallization of M supercells of the mixed system and the energy of the precursors:

$$\Delta E = M(\sum_{j=0}^{J} x_j \epsilon_j - (1-x)\epsilon_A - x\epsilon_B), \tag{2.50}$$

The mixing entropy is defined as

$$\Delta S = -Nk_B(x \ln x + (1-x)\ln(1-x)) - Mk_B \sum_j x_j \ln \frac{x_j}{x_j^0}, \tag{2.51}$$

k_B is the Boltzmann constant and x_j^0 are the *a priori* supercell probabilities, which disregard any thermodynamical effects. Denoting the number of configurations in each group of degenerate supercells as g_j,

$$x_j^0 = g_j(1-x)^{N-N_{B,j}} x^{N_B}. \tag{2.52}$$

The set of solutions x_j is obtained with the minimization of the free energy in the crystallization process. The fabrication usually occurs at constant temperature T and pressure p, minimizing Gibbs mixing free energy $\Delta G = \Delta E - T\Delta S - p\Delta V$. Neglecting the volume variation ΔV, the problem is equivalent to minimizing Helmholtz mixing free energy

$$\Delta F = \Delta E - T\Delta S. \tag{2.53}$$

The phase diagram can be obtained by identifying the spinodal and binodal points in the ΔF curves as a function of temperature. The procedure is detailed elsewhere (VALADARES, 2019). The minimization should be constrained to (2.49), leading to the equations

$$\frac{\partial}{\partial x_i} \left\{ \frac{\Delta F}{M} - \lambda_1 \sum_j x_j - \lambda_2 \left[\sum_j N_{B,j} x_j - Nx \right] \right\} = 0, \ i = 0, 1, ..., J. \tag{2.54}$$

This results in

$$x_j = \frac{x_j^0 \eta^{N_{B,j}} \exp(-\Delta\epsilon_j/k_B T)}{\sum_j x_j^0 \eta^{N_{B,j}} \exp(-\Delta\epsilon_j/k_B T)}, \tag{2.55}$$

where η is a real positive solution to the polynomial equations

$$\sum_{j=0}^{J} g_j(Nx - N_{B,j})\eta^{N_{B,j}} e^{-\Delta\epsilon_j/k_B T} = 0, \qquad (2.56)$$

and the excess energies $\Delta\epsilon_j$ are defined as

$$\Delta\epsilon_j = \epsilon_j - \frac{N_{A,j}}{N}\epsilon_A - \frac{N_{B,j}}{N}\epsilon_B. \qquad (2.57)$$

There is always a single real positive solution of Eq. 2.56, avoiding ambiguity.

The procedure to obtaining the average property of the alloy is then (i) defining the set of representative clusters, g_j, $N_{B,j}$, $\Delta\epsilon_j$, (ii) solving (2.56) for a given (x, T), (iii) obtaining the cluster populations x_j with Equation 2.55 and the cluster properties P_j, and (iv) calculating the alloy property P(x,T) using Eq. 2.48.

As both alloys $CsPb_{1-x}Sn_xI_3$ and $CsSn_{1-x}Ge_xI_3$ are binary, the derivation will be restricted to the original GQCA formulation. The derivation and formulas of Multinary GQCA are described elsewhere (VALADARES, 2019).

3 Cubic AMX$_3$ perovskite systems

3.1 Motivation

Methylammonium lead iodide MAPbI$_3$ is the prototype perovskite for photovoltaic applications. The initial success of this material is due to its very unique set of properties. Its band gap of 1.57 eV is suitable for sunlight absorption, while its low electron and hole effective masses increase the carrier mobility (EPERON *et al.*, 2014; MIYATA *et al.*, 2015). The strong spin-orbit coupling (SOC) effect present in the lead ions produces a Rashba-Dresselhaus splitting in its conduction and valence bands, inducing a unusual recombination mechanism that enhances carrier lifetime (AZARHOOSH *et al.*, 2016). It shows considerable carrier diffusion lengths, reaching up to 1μm (SARDASHTI *et al.*, 2017). Moreover, the high dielectric constant value makes the charge traps (excitons and defects) shallow, so that efficient solar cells can be produced with the relatively less sophisticated solution-processed methods, lowering production costs (GALKOWSKI *et al.*, 2016).

Despite these qualities, future advancements in perovskite solar cells must venture beyond MAPbI$_3$. The investigation of new compositions is crucial to bypass the instability issues and the lead toxicity, which pose as the major problems of this material. Also, besides single-junction solar cells, there is demand for tandem devices. These require the fine manipulation of the band gap of each perovskite absorptive layer.

The most straightforward approach in compositional engineering is to substitute the constituting elements for others with similar chemical behaviour. In the MAPbI$_3$ crystal, the bivalent Pb is commonly substituted for other group-IV bivalent cations such as Sn^{2+} and Ge^{2+}. In addition, the less-studied Si^{2+} will also be considered in this chapter. Its much smaller ionic radius and negligible SOC helps to investigate how the crystal's properties react in more extreme cases. Similarly, the iodine monovalent anion I$^-$ can be substituted by other halogens, which will here be limited to the more usual cases of Br$^-$ and Cl$^-$. Finally, the monovalent cation MA$^+$ can be substituted by other organic molecules, as well as inorganic ions such as the alkali metals. Here, the study will include the most commonly used methylammonium MA (CH$_3$NH$_3$), formamidinium FA (CH(NH$_2$)$_2$), cesium Cs, and also the less common rubidium Rb compositions. This selection amounts to

48 compositions, ranging from well-known to yet hypothetical perovskites.

Not every composition explored in this chapter has been synthesized until the present date. The results aim to predict their properties and encourage further experimental research. Similarly, many of these perovskites are not stable in the cubic phase at room temperature. The choice for the cubic symmetry is due to two considerations. First, the lattice geometry is a determinant factor for the optoelectronic properties in perovskite materials. Therefore, to better isolate and investigate the effects of compositional engineering, it is indispensable to compare different materials while in the same phase. Second, the cubic phase is often sought after due to its increased stability and enhanced properties. As will be seen in the following sections, this higher-symmetry phase broadens the light absorption spectrum, an attractive effect in current perovskite solar cell research. The study of the cubic phase is even more interesting for mixed perovskites, where this state can be stabilized with bond length tuning (LI *et al.*, 2015) or with small-dose incorporation into other materials (NOH *et al.*, 2013).

This chapter will first start by presenting the results of the structural relaxation, including bond lengths, angles and unit cell shape. Following, the orbital origins of the perovskite bandstructure will be explored and the band energy level tuning will be linked to the lattice geometry. Then, Section 3.4 presents the band gaps as obtained by the DFT-1/2 method and compares these results to experiment and to other *ab initio* techniques, validating the model. The study ends with the elaboration on how these structural and orbital factors influence the band gap trends with element substitution.

All calculations were performed by solving the Kohn-Sham equations using the projector augmented-wave method (PAW) as implemented by VASP code. (BLöCHL, 1994; KRESSE; FURTHMüLLER, 1996) The lattice relaxation procedure followed the same parameters: a 500 eV plane wave cut-off energy, 10^{-5} eV break condition for the electronic self-consistent loop, a 0.01 eV/Å break condition for the Hellmann-Feynman forces in the relaxed structure and a gamma-centered k-mesh with eight divisions along each reciprocal lattice vector. The inclusion of spin-orbit coupling into calculations is crucial for an accurate description of the bandstructure due to the presence of heavy elements Pb and Sn, and so it is considered in every case. In order to ease computational costs, each cell was initially relaxed without SOC and subsequently relaxed with the incorporation of SOC. For the exchange-correlation energy the Perdew-Burke-Ernzerhof generalized gradient approximation (GGA-PBE) was employed (PERDEW *et al.*, 1996).

3.2   Structural parameters

In the cubic AMX_3 perovskite, the bivalent metal cation M^{+2} is surrounded by 6 halogens X^-, forming a MX_6 octahedron. Each halogen is shared between two metal cations M and M' located in adjacent octahedra and, in the perfectly cubic system, the MX bonds are aligned so that the $\angle MXM'$ angle equals $180°$. The A^+ cation rests in the cuboctahedral cage and plays an important role in filling the vacancies and maintaining charge equilibrium. Such crystalline lattice belongs to the space group Pm-3m (number 221). Figures 3.1a and 3.1b illustrate both the MX_6 octahedron and the cuboctahedron cage delineated by its surrounding octahedra. The first Brillouin zone is also cubic, as shown in 3.1c. The high-symmetry kpoints X, M and R are positioned respectively in reciprocal coordinates $(\frac{1}{2}, 0, 0)$, $(\frac{1}{2}, \frac{1}{2}, 0)$ and $(\frac{1}{2}, \frac{1}{2}, \frac{1}{2})$.
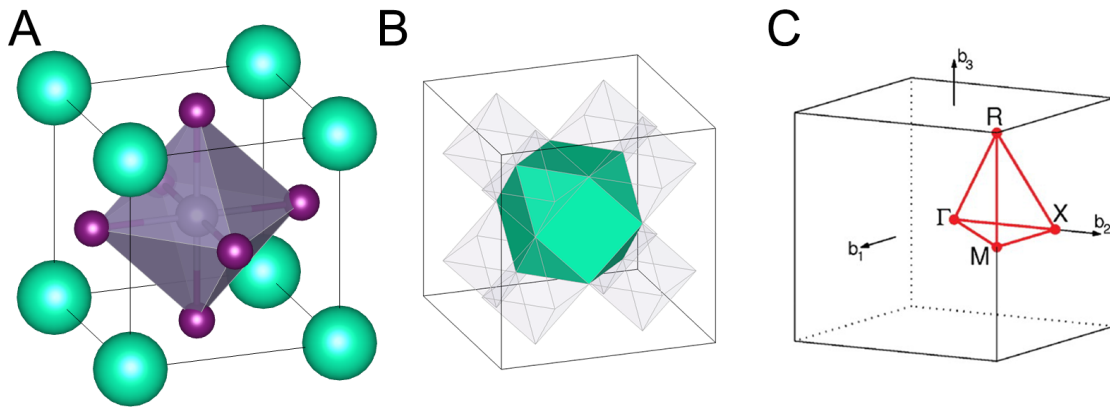
FIGURE 3.1 – Schematic diagram for the cubic perovskite phase of (a) primitive cell, highlighting the MX_3 octahedron; (b) cuboctahedron cage centered by the A-cation, and (c) first Brillouin zone with high symmetry k-points shown. Green, gray and purple spheres represent the A, M and X ions, respectively.

Tables 3.1 and 3.2 display the cell volume and mean lattice constant in comparison to experimental results. The MX framework information is also shown, including mean, maximum and minimum bond lengths and M-X-M bonding angles for each lattice direction. The calculated lattice constant is in good agreement with experiments, giving a maximum and average errors of 2.6% and 1.0%, respectively. This demonstrates that PBE is suficciently accurate to determine the lattice geometry.

The cell dimensions (lattice parameter and volume) follow the expected trend regarding ionic size (FA > MA > Cs > Rb; Pb > Sn > Ge > Si; and I > Br > Cl). But there are two noteworthy exceptions: in spite of the smaller ionic size of Sn with relation to Pb, both $FASnBr_3$ and $FASnCl_3$ have greater volume than their respective lead counterparts $FAPbBr_3$ and $FAPbCl_3$. This odd behaviour was confirmed experimentally for the bromide perovskites (PISANU *et al.*, 2018) and will be seen in Section 3.4 to affect a similarly

irregular trend in their band gap values.

In the hybrid perovskites, the cubic symmetry is disturbed due to the size and geometry of the organic cations MA and FA. There is a consequent deformation in the MX$_6$ octahedra, leading to an uneven distancing between the M ion and some of the halogens. This is expressed in the ratio between the maximum and minimum MX bond lengths as shown in Tables 3.1 and 3.2, which is greater in the more distorted perovskites. Interestingly, between Pb- and Sn-based perovskites, FASnBr$_3$ and FASnCl$_3$ present the highest ratios of 1.43 and 1.55, respectively, whereas the other compositions have lower ratios ranging from 1 to 1.21. This is possibly associated to their anomalously large unit cell volume. Germanium and silicon perovskites, on the other hand, present much higher ratios, reaching up to 2.08 in the case of FASiCl$_3$.

This bond ratio distortion is shown by molecular dynamics calculations in FASnBr$_3$ to be constantly changing. The metal and halogen ions oscillate and the time-averaged bond length equals its arithmetic mean (PISANU *et al.*, 2018). Higher ratios might indicate a structural instability for pure compounds and poor mixing in solid solutions (GUEDES-SOBRINHO *et al.*, 2019b).

The higher distortion for Ge and Si perovskites is also evidenced by the ∠MXM' bonding angles, which are labeled accordingly to each crystallographic direction (a, b and c). FAGeI$_3$ and FASiCl$_3$ show angle values down to 159°, whereas the minimum value amongst tin and lead perovskites is 168°. This difference in distortion can be explained considering the smaller ionic radii of Ge and Si, which contract the inorganic network and makes them more susceptible to A-cation distortion.

3.3   Orbital character

The sophisticated electronic structure of a crystal emerges from the interactions between ionic orbitals (HOFFMANN, 1987). The higher the spatial overlap between the orbitals of different ions, the stronger is their interaction, rearranging the energy levels of the total system. To understand how the structural parameters discussed can influence the band gap, it is thus necessary to determine the orbital character at the valence and conduction bands.

3.3.1   The orbital origin of the valence and conduction bands

The electronic structures of all halide perovskite systems present some common characteristics. The A cation orbitals are known not to participate directly on the formation of bands close to the Fermi level. Therefore, the analysis can be limited the inorganic

TABLE 3.1 – Cell volume ($\mathring{A}^3$), mean lattice constant ($\mathring{A}$), mean, maximum and minimum MX bond length ($\mathring{A}$) and ∠MXM' angle (°) values for APbX$_3$ and ASnX$_3$ perovskites.

PVK	Volume Calc.	Exp.	a Calc.	Exp.	MX bond Max.	Mean	Min.	Angle a	b	c
FAPbI3	270		6.46		3.27	3.23	3.15	177	180	174
FAPbBr3	227	219.7 [a]	5.99	5.99 [a]	3.10	3.05	2.98	177	180	174
FAPbCl3	200		5.86		2.99	2.93	2.83	177	180	175
MAPbI3	265		6.42		3.34	3.22	3.09	172	168	170
MAPbBr3	220		6.04		3.14	3.03	2.90	171	168	171
MAPbCl3	192		5.77	5.7 [b]	3.04	2.90	2.82	169	168	171
CsPbI3	260		6.39	6.289 [c]		3.19			180	
CsPbBr3	215	202.2 [d]	5.99	5.874 [d]		3.00			180	
CsPbCl3	187	176.5 [d]	5.73	5.605 [d]		2.86			180	
RbPbI3	258		6.37			3.18			180	
RbPbBr3	212		5.97			2.99			180	
RbPbCl3	185		5.70			2.85			180	
FASnI3	261		6.39		3.34	3.20	2.98	179	180	172
FASnBr3	233	219.7 [a]	6.16	6.03 [a]	3.86	3.09	2.69	178	170	170
FASnCl3	211		5.97		3.93	2.99	2.53	176	173	172
MASnI3	246	243 [e]	6.35	6.245 [e]	3.43	3.19	2.95	172	170	170
MASnBr3	216		6.01	5.90 [f]	3.32	3.01	2.73	172	170	170
MASnCl3	192		5.78		3.26	2.90	2.56	173	169	171
CsSnI3	248		6.28	6.183 [g]		3.14			180	
CsSnBr3	204	194.8 [h]	5.89	5.797 [h]		2.95			180	
CsSnCl3	178		5.62	5.56 [i]		2.81			180	
RbSnI3	245		6.26			3.13			180	
RbSnBr3	202		5.87			2.93			180	
RbSnCl3	175		5.60			2.80			180	

[a](PISANU et al., 2018); [b](KITAZAWA et al., 2002); [c](TROTS; MYAGKOTA, 2008); [d](MØLLER, 1958); [e](STOUMPOS et al., 2013); [f](FERRARA et al., 2017); [g](SHARMA et al., 1992); [h](SABBA et al., 2015); [i](BARRETT et al., 1971) .

TABLE 3.2 – Cell volume ($\mathring{A}^3$), mean lattice constant ($\mathring{A}$), mean, maximum and minimum MX bond length ($\mathring{A}$) and $\angle$MXM' angle (°) values for AGeX₃ and ASiX₃ perovskites.

| | Volume | | a | | MX bond | | | Angle | | |
PVK	Calc.	Exp.	Calc.	Exp.	Max.	Mean	Min.	a	b	c
FAGeI3	257		6.37	6.25 [a]	4.24	3.22	2.73	180	162	159
FAGeBr3	223		6.09		4.26	3.07	2.50	177	163	162
FAGeCl3	201		5.88		4.25	2.96	2.33	174	164	167
MAGeI3	241		6.23	6.12 [a]	3.65	3.14	2.73	167	165	165
MAGeBr3	202		5.88		3.55	2.96	2.49	169	165	169
MAGeCl3	180		5.66	5.69 [b]	3.49	2.84	2.32	171	167	170
CsGeI3	216	221.4 [c]	6.00	6.05 [c]		3.00			180	
CsGeBr3	176	184.2 [c]	5.61	5.69 [c]		2.81			180	
CsGeCl3	152	163.7 [c]	5.34	5.47 [c]		2.67			180	
RbGeI3	212		5.97			2.98			180	
RbGeBr3	172		5.57			2.78			180	
RbGeCl3	148		5.29			2.65			180	
FASiI3	253		6.34		4.34	3.19	2.63	180	163	161
FASiBr3	221		6.07		4.35	3.05	2.37	174	164	166
FASiCl3	203		5.93		4.54	2.99	2.18	161	159	173
MASiI3	237		6.20		3.68	3.12	2.64	167	167	165
MASiBr3	198		5.85		3.65	2.94	2.37	170	167	170
MASiCl3	186		5.72		3.55	2.87	2.20	172	170	169
CsSiI3	203		5.88			2.94			180	
CsSiBr3	165		5.49			2.75			180	
CsSiCl3	142		5.22			2.61			180	
RbSiI3	198		5.83			2.92			180	
RbSiBr3	161		5.44			2.72			180	
RbSiCl3	138		5.16			2.58			180	

[a](KRISHNAMOORTHY *et al.*, 2015); [b](YAMADA *et al.*, 2002); [c](THIELE *et al.*, 1987).

MX framework. It is also of common understanding in the literature that the valence band maximum (VBM) and the conduction band minimum (CBM) are located at the high-symmetry kpoint R in reciprocal space, with the VBM being originated from an antibonding σ^* state of M$_s$ and X$_p$ orbitals.

There is, however, discussion on the nature of the bottom of the conduction band. In the CBM of MAPbX$_3$ (X = I, Br, Cl), Crespo (2019) observed an antibonding σ^* interaction of M$_p$ and X$_p$. Yuan *et al.* (2015) confirms this result for AMX$_3$ (A = MA, Cs; M = Sn, Pb; X = I, Br, Cl). In apparent contradiction, Kim *et al.* (2015) finds that the conduction band minimum in MAPbI$_3$ is formed by an antibonding Pb$_p$-I$_s$ character, instead of Pb$_p$-I$_p$. By studying the electronic structure of CsMBr$_3$ perovskites (M = Pb, Sn, Ge), the work of Goesten and Hoffmann (2018) concluded that the known direct gap at the R point is a direct consequence of M$_p$-X$_p$ $\sigma^*\pi^*\pi^*$ character at the conduction band. Suppose the metallic ion and the 3 halogens in the unit cell. At the conduction band, the metallic p_x orbital produces two π^* interactions with the Xp_x orbitals of the halogen ions located in the plane transversal to the x axis, and one σ^* interaction with the Xp_x orbitals of the halogen ions aligned in the x direction. At the Γ point, the periodic repetition of these orbitals amounts to a completely antibonding crystal orbital. As the wavefunction kpoint transits continuously from Γ to R, some of these interactions transforms from antibonding to bonding, lowering the energy of the band. At R, the orbitals of neighboring unit cells become completely out of phase, so the number of bonding interactions equals that of antibonding interactions. Thus, R presents a net nonbonding interaction, having a minimal energy and forming the CBM.
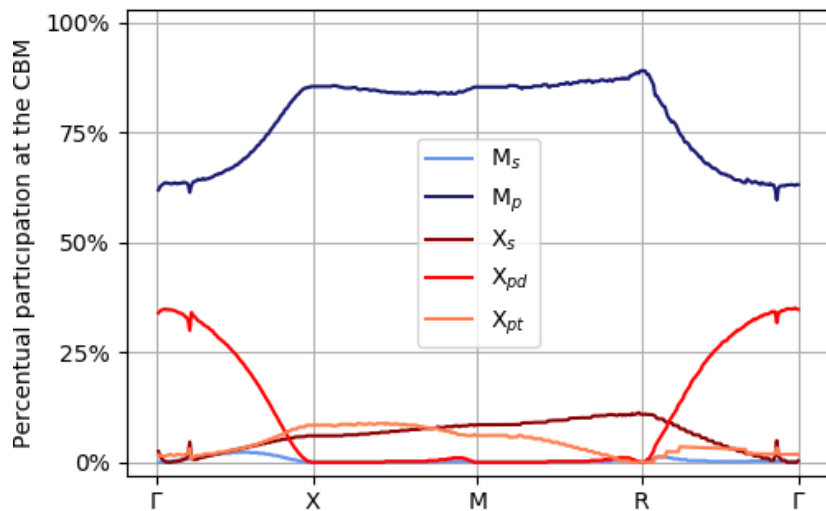
FIGURE 3.2 – Percentual participation of ionic orbitals in the conduction band for CsGeI$_3$. A similar profile is found for all perovskites. The X$_p$ character is divided between those orbitals responsible for σ (X$_{pd}$) and π (X$_{pt}$) bonds with the M ion.

With the objective of testing the literature findings, the electronic structures of the 48 compositions were analysed. As expected, all perovskites show direct gaps at the R point and M$_s$-X$_p$ σ^* interaction at the VBM. The conduction band, on the other hand, discloses much more information. The percentual participation of each ionic orbital of CsPbI$_3$ in the conduction band is shown in Figure 3.2. The X$_p$ orbitals that produce transversal (π) and direct (σ) interactions with M$_p$ orbitals are labeled respectively as X$_{pt}$ and X$_{pd}$. The M$_p$-X$_p$ $\sigma^*\pi^*\pi^*$ character shows up as expected, but it disappears at the CBM. At this point, the net nonbonding equilibrium decouples M$_p$ and X$_p$ orbitals, so X$_p$ is taken out of the mix. However, the X$_s$ orbital becomes predominant at R, for there is no nonbonding equilibrium in the M$_p$-X$_s$ interaction. When looking at the projected density of states, as done by Yuan *et al.* (2015) and Crespo (2019), one may have the impression that X$_p$ is predominant at the CBM due to its strong presence at the conduction band, which explains the confusion.

Given the reasoning above, the existence of the nonbonding equilibrium should be associated to a perfectly cubic lattice. The structural deformation for hybrid perovskites reported in the previous section will then reflect a change in orbital character at the CBM.

A careful analysis of the X$_p$ character in the vicinity of the CBM was conducted for all perovskites, and four general behaviours were identified. Figure 3.3 shows the profile for one representative of each type: CsPbI$_3$ (I), FAPbI$_3$ (II), FAGeCl$_3$ (III) and MASiI$_3$ (IV). Type I was observed in all inorganic perovskites (CsMX$_3$ and RbMX$_3$), and is the ideal behaviour of cubic symmetry as discussed above. Type II is seen in hybrid perovskites with small distortion (long/short bond ratios between 1.21 and 1), where the X$_p$ character makes an almost imperceptible appearance at R. This small breaking of the nonbonding equilibrium occurs in all MAPbX$_3$, FAPbX$_3$ and MASnX$_3$ perovskites, as well as in FASnI$_3$. Interestingly, the most distorted compositions are classified into types III and IV. In type III, the X$_{pd}$ orbital character remains almost or entirely null at R, whereas X$_{pt}$ presents a considerable participation. For type IV compositions, both X$_{pt}$ and X$_{pd}$ orbitals have relevant participations at R.

Only MASiI$_3$ and MASiCl$_3$ fall into type IV. A closer look to their unit cell geometry reveal a common factor: both present high long/short MX bond ratios in all three crystallographic directions in the inorganic lattice. Figure 3.4 (left) shows how this causes the formation of MX$_3$ pyramidal units in the unit cell. In this situation, the bonding and antibonding interactions in R will have different magnitudes, and the nonbonding equilibrium is entirely broken.

The remaining FASnBr$_3$, FASnCl$_3$, MAGeX$_3$, FAGeX$_3$, FASiX$_3$ and FASiBr$_3$ are all of type III. In these cases, the bond ratio is seen to be close to 1 in one or two crystallographic directions (Figure 3.4, right). This causes the nonbonding equilibrium to be conserved for the σ interaction, relative to X$_{pd}$, but broken for π overlaps, relative to X$_{pt}$. One may
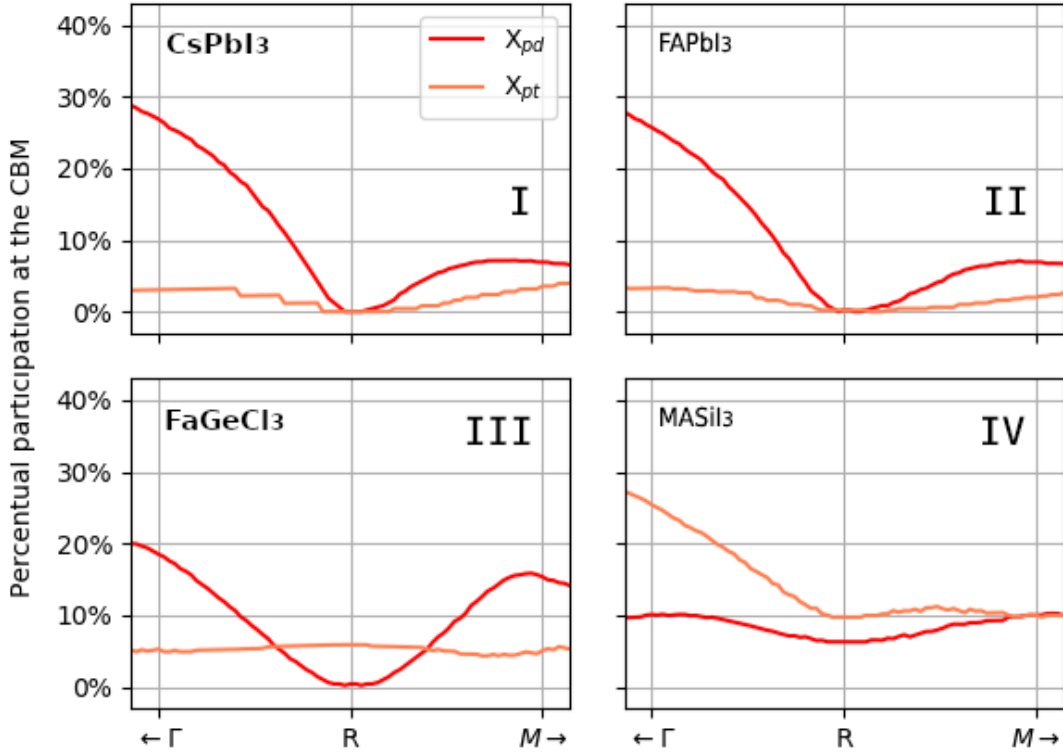
FIGURE 3.3 – Percentual participation of ionic orbitals in the conduction band at the vicinity of R for CsPbI$_3$. A similar profile is found for all perovskites. The X$_p$ character is divided between those orbitals responsible for σ (X$_{pd}$) and π (X$_{pt}$) bonds with the M ion.

ask why the CBM is constituted by σ interactions specifically in the directions with the lowest bond ratio. That is, due to the triple degeneracy of p orbitals, there must be a σ interaction for each x, y and z directions, and in Figure 3.4 (right) only one of the three do not have a nonbonding equilibrium. This is in fact true. However, as will become clearer in the following subsection, the energy increase of the states where the σ nonbonding interaction is broken is much more significantly than the increase caused by breaking the π nonbonding. Therefore, the lowest-lying band, which constitutes the CBM, is the one for which the σ overlap is most nonbonding.

Now the nature of the bandstructure of AMX$_3$ perovskites is understood in detail. Following, it will be shown how changing the interaction between orbitals can affect the energy levels of the CBM and the VBM, consequently tuning the band gap.

3.3.2 Band energy level manipulation

When two orbitals interact, they give origin to pairs of bonding and antibonding states. Increasing the orbital overlap (and consequently the strength of interaction) causes the
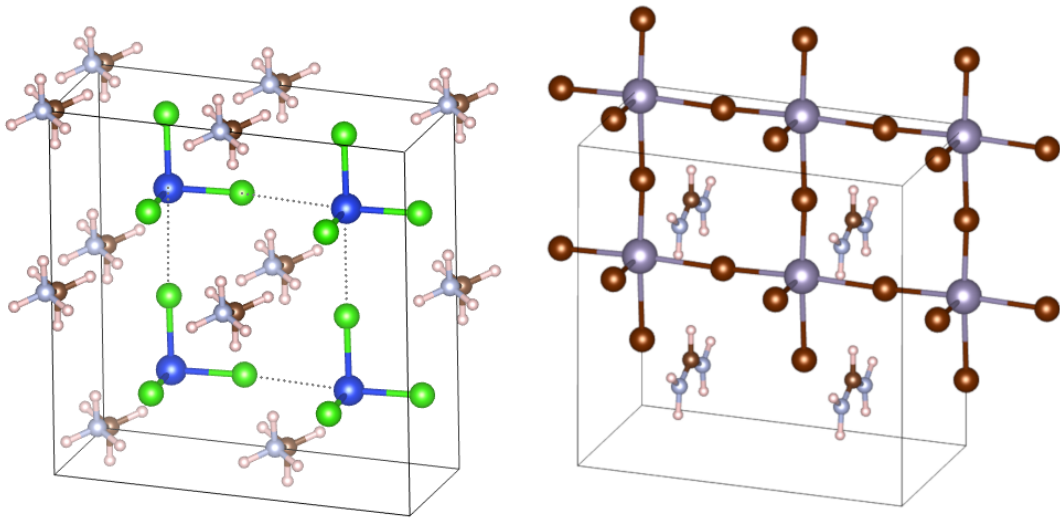
FIGURE 3.4 – Relaxed structure of MASiCl$_3$ (left) and FASnBr$_3$ (right), exemplifying complete and partial MX$_3$ segregation, respectively.

bonding states to decrease in energy, whereas the antibonding states are shifted to higher energies. Both VBM and CBM in halide perovskites are known to be antibonding states. And the orbital overlap in the crystal can be manipulated by changing the structural parameters of the inorganic lattice.

The most straightforward way of manipulating the bandstructure of perovskites is by contraction or expansion of the lattice. Lower MX bond lengths cause both CBM and VBM to destabilize. However, due to the higher metal-halogen orbital mixing in the VBM, its increase in energy surpasses that of the CBM, leading to a decrease in the band gap (PRASANNA et $al.$, 2017).

Another structural parameter that influences the overlap is the ∠MXM' bonding angle. Figure 3.5a is a diagram of the spatial arrangement of X$_p$ and M$_s$ orbitals in a MX array in the valence band maximum. Orbital lobes are represented either as filled or hollow; orbital lobes of the same kind are in phase, whereas out-of-phase lobes have distinct filling. Therefore, the crystal state represented in the figure is completely antibonding, only presenting σ interaction between dephased lobes. When the crystal is distorted and the ∠XMX' angle is lowered (Fig. 3.5b), the ions become misaligned and the orbital overlap is reduced. This causes the VBM energy to stabilize. An analogous reasoning can also be applied to the M$_p$-X$_s$ antibonding interaction in the CBM. However, as for the case of lattice contraction, the larger influence at the CBM results in a net opening of the band gap.

The last element of distortion to be discussed is the partial and complete formation of MX$_3$ units, observed in the last section. Figure 3.6a shows a similar orbital diagram for the M$_p$ and X$_p$ orbitals in the tridimensional MX network. Differently to the X$_p$-M$_s$
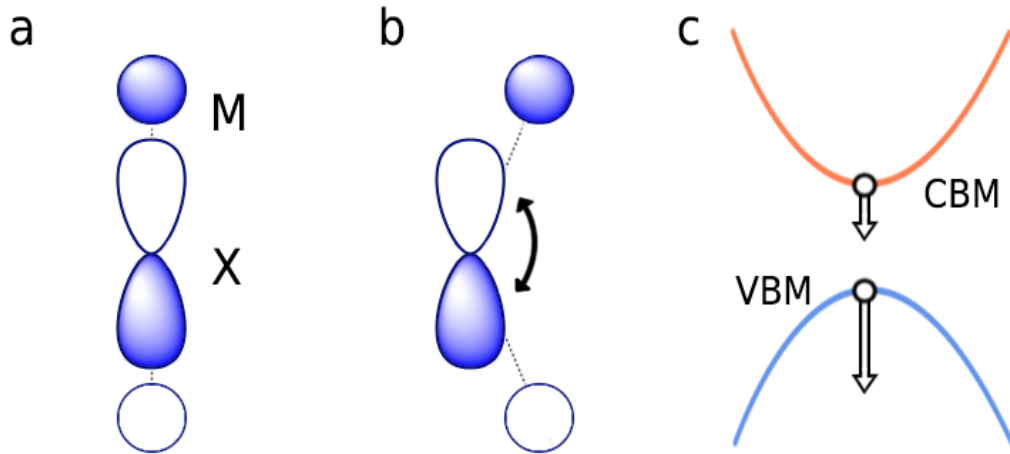
FIGURE 3.5 – (a) M$_s$-X$_p$ antibonding interaction as found in the top of the valence band. (b) M$_s$-X$_p$ interaction after the MX array is misaligned, lowering orbital overlap. (c) consequent change in band energy.

interaction, in this case the X ions localized in the transverse plane to the M$_p$ orbital direction form π interactions and thus must be taken into consideration. Represented in the blue color are the orbitals of the M cation and three X anions inside a single primitive cell of an initially undisturbed cubic lattice. The orbitals of the adjoined cells are represented in red. Since the conduction band is originated from an antibonding overlap, every interaction inside a single unit cell is antibonding, totalizing one σ^* and two π^* interactions. In order to correctly represent the Bloch's crystal state at R $(\frac{1}{2},\frac{1}{2},\frac{1}{2})$, every orbital in the neighboring cells must be out-of-phase with relation to its analogous in the central cell. Therefore, if all M$_p$-X$_p$ overlaps are considered, there is one bonding interaction for every antibonding interaction, adding up to a nonbonding equilibrium. Consider then the distortion as shown in Figure 3.6b, where the long/short bond ratio is risen above the ideal unitary value. This distortion causes the orbital overlap of σ^* and π^* antibonding interactions to increase, while separating σ and π bonds. Consequently, the crystal state is destabilized, increasing the energy level of the CBM and consequently increasing the band gap.

In the case of partial segregation of MX$_3$ units, where one or two of the halogen ions remain halfway between two metal ions, the gap opening is not as significant as in complete segregation. This is so because the π^* interactions observed in the CBM in type III compositions are weaker than σ^* orbital interactions. Ultimately, it is not possible to assert with certainty with static DFT calculations which compositions present a type III or type IV bandstructure, for the MX connections are dynamical. However, it is reasonable to suppose that for a fixed A cation, smaller M and X ions will tend to present a type IV character due to shorter bond lengths.
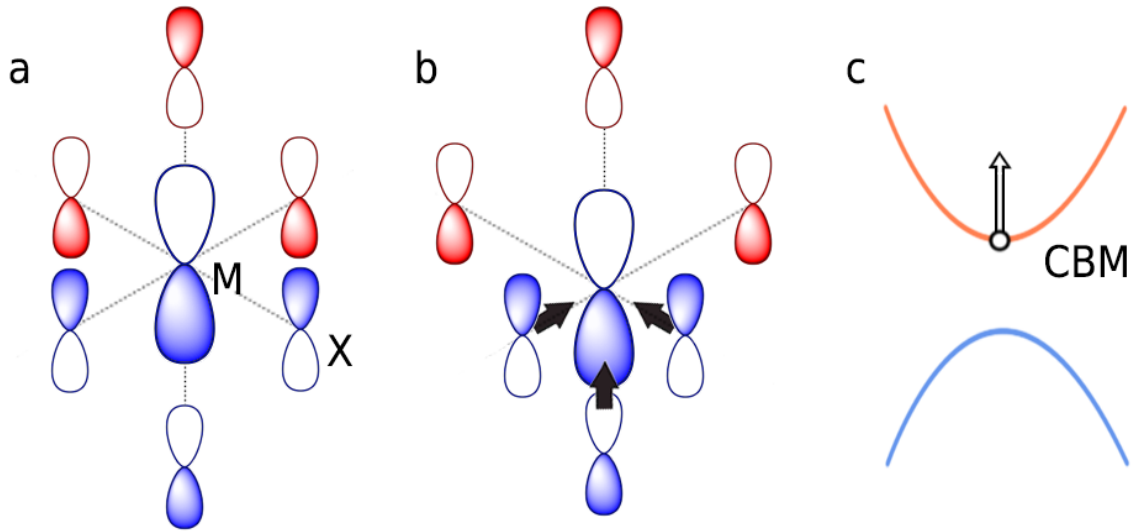
FIGURE 3.6 – (a) M$_p$-X$_p$ nonbonding interaction as found in the bottom of the conduction band. (b) M$_p$-X$_p$ arrangement for long/short bond ratios higher than 1, enhancing antibonding and lowering bonding overlap. (c) consequent destabilization of the CBM energy level.

In light of the orbital considerations, the succeeding sections are committed to analyze and explain the band gap values and trends of different perovskites.

3.4   Band Gap

The bandstructures of all 48 compositions were determined using DFT and DFT-1/2 correction. The approximate DFT-1/2 correction was employed, where only the removal of half electron from the halogen p orbital is considered. This approximation was previously reported to generate good results for perovskite systems, and is seen to account for most of the self-energy terms in Eq. 2.35 (GUEDES-SOBRINHO *et al.*, 2019a).

As an example, Fig. 3.7 shows the archetype bandstructure of CsPbI$_3$ with and without spin-orbit coupling, as obtained by the DFT-1/2 method. The conduction band minimum is in principle threefold degenerate, with each band related to a M$_p$-X$_s$ antibonding interaction between the group-IV cation and one of the three halogens comprised in the unit cell. However, the SOC lifts this degeneracy, splitting the conduction band into two degenerate p$_{\frac{3}{2}}$ bands with higher energy and a third and more stable p$_{\frac{1}{2}}$ band, similarly to the valence band of III-V semiconductors (COMBESCOT *et al.*, 2019). This splitting caused by relativistic effect leads to the reduction of band gap. The magnitude of such closing is expected to be stronger for heavier elements such as Pb and Sn, weak for Ge and negligible for Si, due to the atomic number of each element. The CBM of the

lighter elements Ge and Si thus remains nearly degenerate.
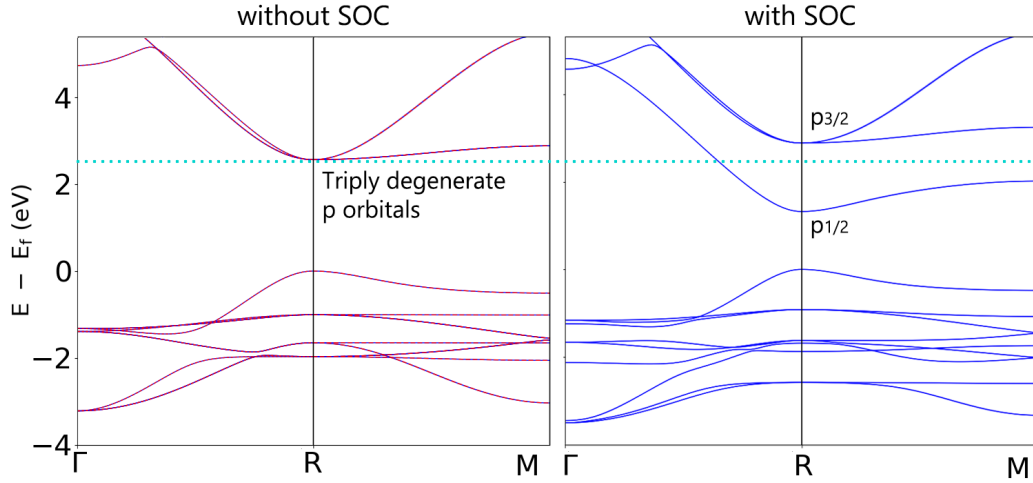
FIGURE 3.7 – DFT-1/2 band structure of cubic CsPbI$_3$ without (left) and with (right) spin-orbit coupling.

The DFT and DFT-1/2 gap values obtained computationally for each cubic perovskite are shown in Tables 3.3 and 3.4, as well as results from HSE06 and variations of GW found in the literature: GW$_0$ (BOKDAM *et al.*, 2016; SUTTON *et al.*, 2018), and QSGW (HUANG; LAMBRECHT, 2016). These are compared to experimental values when available. In many cases the values retrieved in literature are obtained for perovskite phases other than cubic, and so the lattice system of each material is indicated for proper comparison. The DFT-1/2 method systematically corrects the well-known underestimation of DFT band gap, showing gaps close to experiment. For the commonly studied FAPbI$_3$, MAPbI$_3$ and CsPbI$_3$, the correction broadens the DFT gap by over 1 eV, reaching values with absolute errors smaller than 0.16 eV.

11 perovskites have both experimental and GW data available for the cubic phase. In these cases, the DFT-1/2 method reaches an average absolute error of 0.193 eV compared to 0.197 eV for GW. Considering the perovskites MAPbBr$_3$, MAPbCl$_3$, CsPbI$_3$, MASnI$_3$ and MASnBr$_3$, for which there is also HSE06 data, both GW and DFT-1/2 present an average absolute error of 0.164 eV with relation to experimental gaps, whereas the hybrid functional method have a much larger mean error of 0.447 eV. Therefore, the DFT-1/2 method comes out as an accurate alternative to the more costly GW and HSE06 calculations. In general, GW have broader band gaps than both DFT-1/2 and hybrid functional methods, often overestimating the experimental result. GW and DFT-1/2 present a similar accuracy, whereas the HSE06 method presents less accurate results in comparison to the other methods.

As a general rule, DFT-1/2 renders band gap values slightly smaller than experiment. This tendency can be primarily explained by the cubic phase adopted in our calculations.

TABLE 3.3 – Calculated DFT and DFT-1/2 band gaps in eV for APbX$_3$ and ASnX$_3$ perovskites compared to experimental, GW and hybrid functional values found in literature. The lattice system of collected values are indicated for proper comparison: (c), (t), and (o) the cubic, tetragonal, and orthorhombic lattice systems. The orbital character classification as defined in Fig. 3.3 is also shown.

Perovskite	orbital char.	DFT	DFT$-\frac{1}{2}$	Exp.	GW	HSE06
FAPbI3	II	0.32	1.39	1.48 (c)[a]	1.48[b] (c)	
FAPbBr3	II	0.74	2.04	2.18 (c)[c]	2.26 (c)[b]	
FAPbCl3	II	1.20	2.61		3.07 (c)[b]	
MAPbI3	II	0.54	1.55	1.57 (t)[d]	1.675 (c)[e]	1.82 (c)[f]
MAPbBr3	II	0.92	2.16	2.2 (c)[d]	2.34 (c)[b]	2.44 (c)[f]
MAPbCl3	II	1.36	2.70	3.11 (c)[g]	3.07 (c)[b]	2.91 (c)[f]
CsPbI3	I	0.25	1.32	1.48 (c)[h]	1.14 (c)[h]	0.755 (c)[i]
				1.73 (o)[d]	1.57 (o)[h]	
CsPbBr3	I	0.60	1.88	2.25 (o)[j]	1.868 (c)[e]	
CsPbCl3	I	1.02	2.39	2.86 (t)[j]	2.678 (c)[e]	
RbPbI3	I	0.23	1.29			
RbPbBr3	I	0.57	1.84			
RbPbCl3	I	0.99	2.34			
FASnI3	II	0.33	1.27	1.41 (c)[k]	1.27 (c)[b]	
FASnBr3	III	1.10	2.15	2.37 (c)[c]	2.67 (c)[b]	
FASnCl3	III	1.70	2.74		3.90 (c)[b]	
MASnI3	II	0.42	1.34	1.20 (c)[k]	1.03 (c)[b]	0.94 (c)[f]
MASnBr3	II	0.85	1.93	2.00 (c)[l]	1.87 (c)[b]	1.19 (c)[f]
MASnCl3	II	1.43	2.51		4.02 (c)[b]	1.70 (c)[f]
CsSnI3	I	0.07	1.02	1.27 (o)[m]	1.008 (c)[e]	0.344 (c)[i]
					1.3 (o)[e]	0.804 (o)[i]
CsSnBr3	I	0.28	1.43	1.75 (c)[m]	1.382 (c)[e]	
CsSnCl3	I	0.64	1.84	2.23 (c)[n]	2.693 (c)[e]	
RbSnI3	I	0.02	0.97			
RbSnBr3	I	0.23	1.37			
RbSnCl3	I	0.58	1.77			

[a](PRASANNA et al., 2017); [b](BOKDAM et al., 2016); [c](PISANU et al., 2018); [d](EPERON et al., 2014); [e](HUANG; LAMBRECHT, 2016); [f](KOLIOGIORGOS et al., 2017); [g](KITAZAWA et al., 2002); [h](SUTTON et al., 2018); [i](RAY et al., 2018); [j](LIU et al., 2013); [k](STOUMPOS et al., 2013); [l](FERRARA et al., 2017); [m](SABBA et al., 2015); [n](VOLOSHINOVSKII et al., 1994).

A comprehensive first-principles study published by Jacobsen's group support that the band gap is larger for structures with lower symmetry (CASTELLI et al., 2014). The octahedral tilting present in tetragonal and orthogonal phases diminishes the orbital overlap and stabilizes the valence band maximum. A similar reasoning should be extended to the less studied rhombohedral phase adopted by germanium perovskites. Also, molecular dynamics studies show that the MX bonds in hybrid perovskites are dynamically distorted due to the constant motion of the organic cation in higher-temperature phases

TABLE 3.4 – Calculated DFT and DFT-1/2 band gaps in eV for AGeX$_3$ and ASiX$_3$ perovskites compared to experimental, GW and hybrid functional values found in literature. The lattice system of collected values are indicated for proper comparison: (c) and (r) the cubic and rhombohedral lattice systems. The orbital character classification as defined in Fig. 3.3 is also shown.

Perovskite	orbital char.	DFT	DFT$-\frac{1}{2}$	Exp.	GW	HSE06
FAGeI3	III	1.23	2.08	2.35 (r)[a]		
FAGeBr3	III	1.63	2.65	-		
FAGeCl3	III	2.12	3.16	-		
MAGeI3	III	1.14	2.03	2.00 (r)[a]		1.21 (c)[b]
MAGeBr3	III	1.49	2.55	-		1.51 (c)[b]
MAGeCl3	III	2.01	3.10	-		1.96 (c)[b]
CsGeI3	I	0.39	1.29	1.63 (r)[a]	1.199 (c)[c]	
					1.619 (r)[c]	1.41 (r)[d]
CsGeBr3	I	0.59	1.71	2.38 (r)[e]	1.800 (c)[c]	1.66 (r)[d]
CsGeCl3	I	0.92	2.12	3.43 (r)[e]	2.654 (c)[c]	2.22 (r)[d]
RbGeI3	I	0.33	1.22	-		
RbGeBr3	I	0.49	1.60	-		
RbGeCl3	I	0.80	1.98	-		
FASiI3	III	0.66	1.39	-		
FASiBr3	III	1.11	1.92	-		
FASiCl3	III	1.79	2.51	-		
MASiI3	IV	0.83	1.54	-		
MASiBr3	III	0.92	1.78	-		
MASiCl3	IV	2.51	3.15	-		
CsSiI3	I	-	0.49	-	0.313 (c)[c]	
CsSiBr3	I	-	0.72	-	0.381 (c)[c]	
CsSiCl3	I	-	1.02	-	1.427 (c)[c]	
RbSiI3	I	-	0.37	-		
RbSiBr3	I	-	0.55	-		
RbSiCl3	I	-	0.80	-		

[a](KRISHNAMOORTHY et al., 2015); [b](KOLIOGIORGOS et al., 2017); [c](HUANG; LAMBRECHT, 2016); [d](WALTERS; SARGENT, 2018); [e](LIN et al., 2008).

(QUARTI et al., 2015; PISANU et al., 2018). Quarti et al. (2015) have found that the gap experiences variations of up to 0.22 eV for cubic-phase FAPbI$_3$ and 0.13 eV for tetragonal MAPbI$_3$. This effect is not contemplated in our calculations since the methods here presented consider a static frame.

A previous publication assessing the application of DFT-1/2 to two-dimensional systems indicates that the success of the approximation is compound-dependent (GUILHON et al., 2018). Since this method is designed for correcting localized electronic states, a lower orbital mixing between M$_s$ and X$_p$ orbitals at the VBM results in better gap values. Considering that the M$_s$ energies lie well below those of X$_p$ orbitals, the increased

electronegativity of the halogen ion brings both energy levels closer together, enhancing the orbital mixing at the VBM. This enlightens the higher accuracy of the method for iodide perovskites in comparison to bromide perovskites, and of the latter in comparison to chloride materials. Such considerations can partially explain the discrepancy found for CsGeCl$_3$.
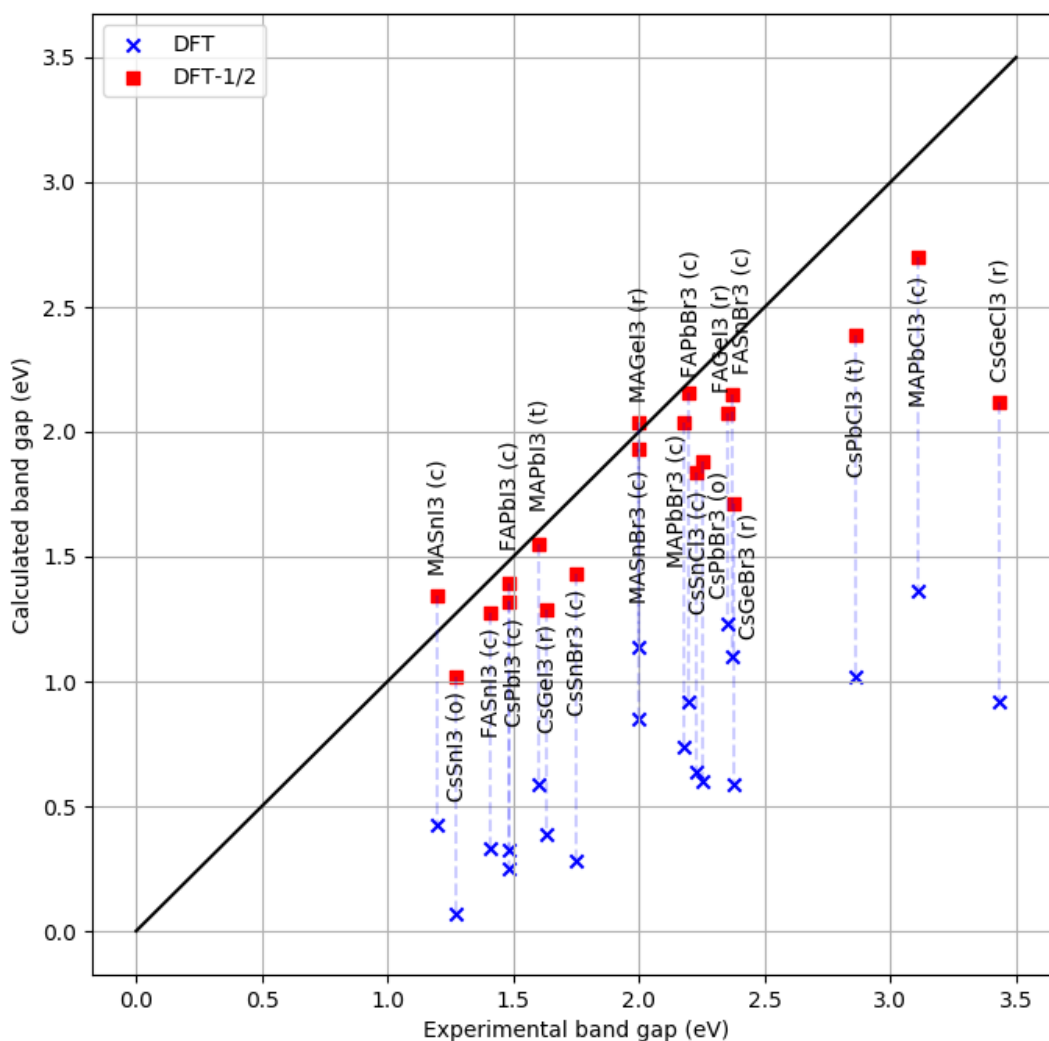
FIGURE 3.8 – DFT-$\frac{1}{2}$ and default DFT band gap results in comparison to experimental band gaps for perovskites for which there are data available. Each labels indicates the corresponding perovskite and the phase in which the experimental results were obtained, being (c), (t), (o) and (r) the cubic, tetragonal, orthorhombic and rhombohedral lattice systems, respectively.

The corrected values show an outstanding agreement with experimental data, as is evidenced in Figure 3.8. This correspondence validates the use of the method for pre-

dicting hypothetical materials such as some Ge-, Si- and Rb-containing perovskites. The results also point out promising candidates for further investigation. Calculations on the theoretical limit of single junction solar cell efficiency conclude that materials with band gap between 0.93 eV and 1.61 eV can reach PCE above 30% (RüHLE, 2016). 16 of the 48 investigated perovskites fall within this range, 12 of which contain iodine, 3 are Si-based materials (FASiI$_3$, MASiI$_3$ and CsSiCl$_3$) and 4 contain rubidium (RbSnI$_3$, RbSnBr$_3$, RbGeI$_3$, RbGeBr$_3$). Among the materials containing Ge and Sn, RbSnBr$_3$ and RbGeBr$_3$ are of special interest due to the reduced lattice size and higher electronegativity of Br in comparison to I, two factors that may reduce vulnerability to oxidation.

3.5   General trends

Figure 3.9 shows the corrected band gap results for all perovskites as a function of composition. The metal ions are separated into different graphs, and each color represents an A cation. This section focus on justifying the band gap trends and eventual anomalies found.

The most prominent feature is the broadening of the band gap with the halogen electronegativity, a well-known effect in the literature (SUTTON *et al.*, 2016; ZARICK *et al.*, 2018; CRESPO, 2019; YUAN *et al.*, 2015). The I $\rightarrow$ Br $\rightarrow$ Cl substitution involves two conflicting mechanisms: the reduction in unit cell dimensions, which increases the VBM energy, and the reduction of X$_p$ energy level. Since the valence band is primarily composed of X$_p$ orbitals, the VBM energy level ϵ_{VBM} lowers significantly. The CBM is also affected by destabilization of the antibonding interaction and the stabilization of the X$_s$ energy, although less significantly in both cases. The result is a non-trivial trend in the VBM level of CsSnX$_3$ and MASnX$_3$ perovskites as reported by Yuan *et al.* (2015), with $\epsilon_{\text{VBM}}(\text{Br}) > \epsilon_{\text{VBM}}(\text{Cl}) > \epsilon_{\text{VBM}}(\text{I})$. They also found a regular decrease in the CBM energy with higher electronegativity. Crespo (2019) found a regular trend $\epsilon_{\text{VBM}}(\text{I}) > \epsilon_{\text{VBM}}(\text{Br}) > \epsilon_{\text{VBM}}(\text{Cl})$ for MAPbX$_3$ perovskites, with little influence over the CBM. In summary, although the precise movement of both bands should be verified in each case, all literature results show a net broadening in gap with halogen electronegativity, no matter the identity of A and M cations. Figure 3.9 has the same behaviour, with average increases of 0.48 eV for I $\rightarrow$ Br substitution and 0.47 eV for Br $\rightarrow$ Cl substitution (excluding the outlier MASiCl$_3$).

Halide ion exchange does not allow one to achieve narrower band gaps, so it is necessary to explore other forms of electronic manipulation, such as A cation replacement. As previously mentioned, the A cation does not participate directly in the formation of conduction or valence bands, although it can indirectly affect the electronic structure by

reshaping MX bonds. When the cation is a molecule, it breaks the cubic symmetry. If it is too large to fit the cuboctahedron cage of the inorganic network, it induces the bonding angle distortion and increases the gap. These effects can be attested in Fig. 3.9. Especially for Sn, Ge and Si perovskites, the FA and MA compositions have considerably larger gaps than their inorganic counterparts due to this symmetry breaking. Also, the magnitude of this effect increases with smaller M cations due to the higher susceptibility to distortion. The A cation also affects the overall bond length. For the undistorted inorganic perovskites, the lattice contraction caused by Cs → Rb substitution causes a consistent decrease in band gap, as expected.
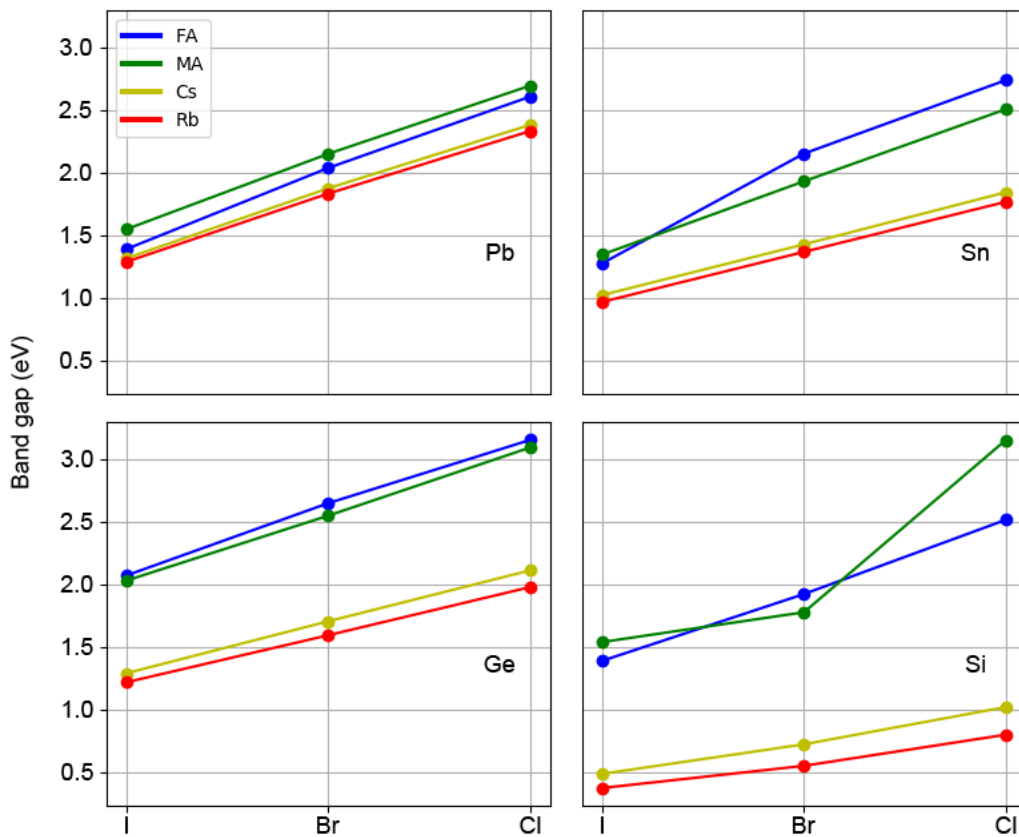
FIGURE 3.9 – DFT-$\frac{1}{2}$ band gap as a function of chemical composition. Formamidinium (FA), methylammonium (MA), cesium (Cs) and rubidium (Rb) perovskites are respectively ploted in blue, green, yellow and red colors.

The last option of composition exchange is by selecting the metal ion. This case is less well-behaved as it involves various chemical and structural effects. The substitution of Pb for lighter group-IV cations (1) decreases the SOC magnitude, consequently increasing the band gap; (2) contracts the MX bond lengths, closing the gap; (3) increases the electronegativity of the M$_p$ orbitals at the CBM, narrowing the gap; and (4) leaves the MX network vulnerable to the A molecule distortion. Factor (4) is less predictable and confuses the search for meaningful chemical trends. Considering only the inorganic perovskites,

which are affected only by factors (1-3), the results for Cs and Rb perovskites reveal a consistent gap narrowing occurring with Pb $\rightarrow$ Ge $\rightarrow$ Sn $\rightarrow$ Si substitution. There is not a direct correlation between gap and the atomic number. Whereas Pb $\rightarrow$ Sn causes a gap closing due to factors (2) and (3), Sn $\rightarrow$ Ge causes an abrupt loss of magnitude in spin-orbit coupling, broadening the gap. The same non-trivial gap trend was observed by Huang *et al.* (2016) in a first-principles study using GW approximation. Inorganic silicon perovskites have the lowest gap values, whereas some of their hybrid versions present band gaps broader than Sn perovskites. This confirms that factor (4) can disturb the observed trend.

There are two intriguing cases in Figure 3.9 that must be assessed individually. Firstly, both FASnBr$_3$ (2.15 eV) and FASnCl$_3$ (2.70 eV) have higher gap values than their lead counterparts FAPbBr$_3$ (2.04 eV) and FAPbCl$_3$ (2.61 eV), as opposed to what is observed in every other APbX$_3$/ASnX$_3$ pair. They have also unexpectedly broader gaps than their methylammonium versions MASnBr$_3$ (1.93 eV) and MASnCl$_3$ (2.51 eV), respectively. These two compositions were already mentioned in Section 3.2, where they also showed a large unit cell volume. This, however, is not the only factor influencing the gap. In Section 3.3, they were identified as the only perovskites amongst Pb and Sn compositions that presented partial MX$_3$ formation (type III orbital profile). Every other composition were classified either as type I or type II (See Table 3.3). As was previously explained, the distortion caused by the partial segregation broadens the band gap.

Secondly, there is an anomalous evolution with halide ion exchange in MASiX$_3$ perovskites. MASiBr$_3$ has narrower gap than both MASiI$_3$ and MASiCl$_3$, the Br $\rightarrow$ Cl substitution leading to a remarkable broadening of 1.37 eV. This is no surprise, since MASiI$_3$ and MASiCl$_3$ were the only perovskites to present a complete formation of pyramidal MX$_3$ structures, thus having a type IV orbital profile. The impact of the nonbonding equilibrium breaking in the CBM energy level is considerably stronger in type IV compounds than that for type III perovskites, explaining why the MASiBr$_3$ gap is this narrow with relation to the other methylammonium silicon halides.

Once again, it must be mentioned the importance of considering the system's dynamics and its impact on the band gap. There is in principle no reason for MASiBr$_3$ to be of type III while MASiI$_3$ is classified into type IV. A possible path for future studies is to understand how the MA and FA rotations impact the energy level and orbital character of the CBM.

3.6   Conclusion

In this chapter, the quasiparticle correction DFT-1/2 is reaffirmed as a fast and accurate method for the study of electronic properties of metal halide perovskites. The band gaps of a broad number of perovskites were obtained with accuracy similar to that of GW method when compared to the experiment, and the deviations can be partly attributed to the lack of dynamical distortion and eventual difference in phase. This result therefore sustains the competence of the method in predicting the electronic properties of less studied materials such as silicon-, germanium- and rubidium-containing perovksites. 16 materials were identified as falling within the band gap range of 0.93 eV-1.61 eV, coming up as promising candidates for the photoactive layer of solar cells.

The orbital character of both conduction and valence bands were analysed in detail for every material, consistently showing respectively the presence of M_p-X_s and M_s-X_p antibonding character at the CBM and VBM. Even though a significant presence of X_p orbitals is observed in the conduction band, this character vanishes at the CBM due to a net nonbinding interaction. The knowledge of the atomistic origin of the bandstructure sheds light on the relationship between structural parameters and band gap, which was inspected carefully. Cs $\rightarrow$ Rb substitution is observed to cause a consistent band gap reduction due to lattice contraction. Also, the hybrid perovskites show a higher band gap than their inorganic counterparts due to structural distortion, and smaller metal ions show to be more susceptible to this effect due to their more contracted MX lattice. In more extreme cases of lattice distortion, such as in Ge and Si perovskites, the organic molecules force the detachment of metal-halogen bonds, destabilizing the CBM state and broadening the gap. In MASiI$_3$ and MASiCl$_3$ perovskites, this leads to the segregation of MX$_3$ units.

The calculations allow the investigation of purely chemical aspects of electronic structure manipulation. The increased halogen electronegativity has a major influence in the blueshift of absorption onset, leading to materials appropriate for the top layer of tandem solar cells. Moreover, the inorganic Ge-based perovskites are seen to have broader gaps than their Sn-based relatives, a trend attributed to the tuning of spin-orbit coupling with metal substitution.

In conclusion, orbital, structural, and chemical arguments were employed for a reasonable and comprehensive understanding of the electronic properties of a large set of perovskite semiconductors. This study opens up a path for further exploration and manipulation of new materials for the fabrication of cheap, efficient, and stable solar cells.

4 CsPb$_{1-x}$Sn$_x$I$_3$ - Minimizing the band gap

4.1 Motivation

The attention towards CsPbI$_3$-based perovskite solar cells has intensified in the last few years, since Eperon *et al.* (2015) reported a device with 2.9% efficiency. The enthusiasm for the replacement of the organic cation in MAPbI$_3$ or FAPbI$_3$ for Cs and Rb was justified by the enhanced thermal stability of the inorganic materials (KRISHNAMOORTHY *et al.*, 2015), overcoming one of the major obstacles for the fabrication of commercial perovskite devices. Despite presenting an initially low performance, not long after Swarnkar *et al.* (2016) reported a quantum-dot photovoltaic cell with efficiency of 10.77%. Many subsequent studies reported PCE above 13% using varied techniques (NAM *et al.*, 2018). In special, Wang *et al.* produced stable 17% efficient solar cells using Br-doped CsPbI$_3$ (WANG *et al.*, 2018).

This fast development encourages the research on CsPbI$_3$ and related perovskites for surpassing the known problems. Orthorhombic CsPbI$_3$ has a band gap of 1.73 eV, which theoretical calculations show to be somewhat larger than the optimal value for single-junction solar cells (RüHLE, 2016). This limits the solar radiation absorption and, therefore, reduces the maximum PCE achievable. Also, its black perovskite phase is unstable at room temperature, rapidly degrading to an optically inactive yellow (δ) phase in the presence of humidity. The performance of the cell thus depends on preventing this phase transition.

One interesting perspective of enhancing the light absorption spectrum is to fabricate CsPbI$_3$ in its cubic (α) phase. *Ab initio* calculations indicates this band gap to be, in fact, lower than that of the orthorhombic phase due to the lowering of bond angle distortions (SUTTON *et al.*, 2018). However, the black perovskite phase observed at room temperature is in truth the orthorhombic (γ) phase, the α phase only becoming stable at high temperatures (SUTTON *et al.*, 2018). Extrapolation of the band gap dependency with temperature estimates that the cubic phase has a gap of 1.48 eV at T = 0 K, a value

closer to the DFT-1/2 and GW predictions.

Many studies suggest that the cubic phase can be stabilized over both γ and δ phases at room temperature with surface engineering (LI *et al.*, 2018; DING *et al.*, 2019; YANG; TAN, 2020). This involves either the inclusion of surface ligands or the fabrication of nanocrystals, although in the latter case the quantum confinement effect might broaden the band gap back to non-ideal values (PROTESESCU *et al.*, 2015).

Another possibility for the band gap optimization is metal alloying. CsSnI$_3$ has a considerably smaller gap of 1.27 eV (SABBA *et al.*, 2015), allowing CsPb$_{1-x}$Sn$_x$I$_3$ to reach adequate values for single-junction cells. More than that, the previous literature reports that tin-lead mixed perovskites present a strong gap bowing, so much so that some intermediate compositions have narrower gaps than those of tin and lead pristine materials (RAJAGOPAL *et al.*, 2019). Tin-lead alloying can also contribute to the device stabilization: Swarnkar *et al.* (2018) suggest that the tuning of bond lengths can stabilize the black phase at room temperature, and Leijtens *et al.* (2017) show that the mixing of both metals can reduce Sn oxidation. A recent showed γ-CsPb$_{0.7}$Sn$_{0.3}$I$_3$ solar cells with significantly larger stability when exposed to air than those of MAPb$_{0.7}$Sn$_{0.3}$I$_3$ and CsPbI$_2$Br (YANG *et al.*, 2020).

Given this context, the cubic CsPb$_{1-x}$Sn$_x$I$_3$ alloy has a good perspective for photovoltaic applications. The objective of this chapter is to report the calculation of this perovskite. Its electronic structure will be determined with the DFT-1/2 correction and studied in correlation to structural and thermodynamical effects. The detailed methods applied are expected to provide an in-depth understanding of the underlying mechanisms of the band gap bowing, which will be assessed in view of previous literature. The results shown should serve as a guide for the fabrication of respective solar cells, and also for shedding light on the study of other tin-lead mixed perovskite systems.

4.2 Symmetry and structural relaxation

As discussed in the previous chapter, the atomic arrangement in a semiconductor is determinant of its electronic structure. Obtaining the equilibrium crystalline structure is then a crucial step for accurate first principle calculations. In alloys, this relationship becomes more sophisticated since the compositional disorder brings up a correlated structural disorder. Hence, we start with the careful analysis of the geometry, bonding and symmetry in CsPb$_{1-x}$Sn$_x$I$_3$ alloys.

Even though CsPbI$_3$ and CsSnI$_3$ both adopt the orthorhombic perovskite phase at ambient conditions, they transform to the cubic phase at temperatures above 425 K and 375 K, respectively, and so their cubic lattice parameters can be measured (MARRONNIER
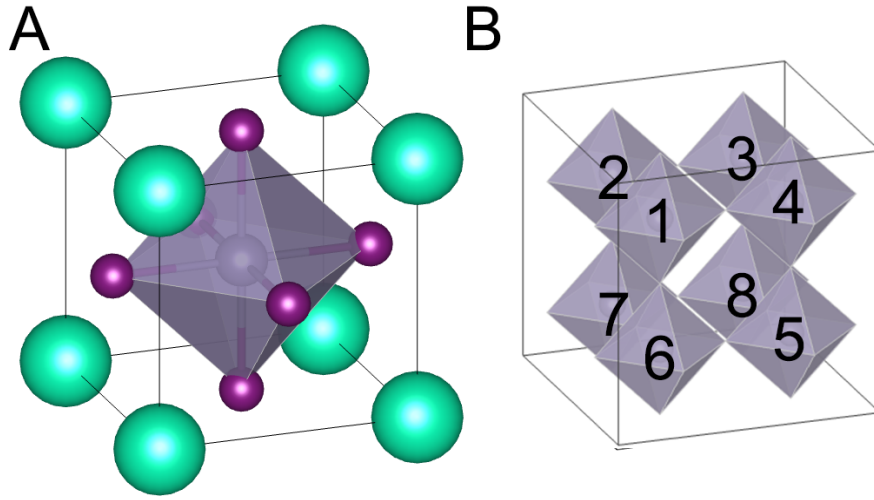
FIGURE 4.1 – Schematic diagram for the cubic perovskite phase of (a) primitive cell, highlighting the MX$_6$ octahedron and its (b) 2x2x2 supercell, with a number from 1 to 8 assigned to each metal cation. Green, gray and purple spheres represent the A, M and X ions, respectively.

TABLE 4.1 – Symmetry information on the 22 groups of degenerate 8-fold supercells of cubic CsPb$_{1-x}$Sn$_x$I$_3$. The supercells are numbered from j = 0 to j = 21. The degeneracy g$_j$ and the number of Sn ions is displayed. The internal atomic arrangement of a representative supercell is represented by a list of letters, where the i-th letter is A or B when the i-th metal position is occupied by a Pb or Sn cation, respectively.

j	g$_j$	# Sn	Configuration 12345678	j	g$_j$	# Sn	Configuration 12345678
0	1	0	AAAAAAAA	11	24	4	BBBABAAA
1	8	1	BAAAAAAA	12	24	5	BBBBABAA
2	12	2	BBAAAAAA	13	6	4	BABAABAB
3	12	2	BABAAAAA	14	24	5	BBBABAAB
4	24	3	BBABAAAA	15	12	6	BBBBABBA
5	6	4	BBBBAAAA	16	2	4	BABABABA
6	8	3	BABABAAA	17	8	5	BBBABABA
7	8	4	BBABABAA	18	12	6	BBBBBABA
8	4	2	BAAAAAAB	19	4	6	BBBABBAB
9	24	3	BABAABAA	20	8	7	BBBBBBBA
10	24	4	BBBAABAA	21	1	8	BBBBBBBB

et al., 2018; YAMADA *et al.*, 1991). From Table 3.1, the calculations for CsPbI$_3$ resulted in cubic edges of 6.39 Å in comparison to 6.289 Å as found by x-ray diffraction (TROTS; MYAGKOTA, 2008). For CsSnI$_3$, the calculated lattice constant was 6.28 Å, also slightly larger than the experimental value of 6.219 Å (YAMADA *et al.*, 1991). Both results show to be good approximations, with error below 1.6%.

The alloy calculations were done with a 40-atom 2x2x2 supercell, with the eight octahedra being centered either on a lead or tin cation. Figure 4.1b shows this structure where the M positions are numbered from 1 to 8. There are, in principle, $2^8 = 256$ possible configurations. With the use of crystalline symmetries, these configurations are reduced to 22 representative supercells. Table 4.1 lists the group's degeneracy, atomic composition, and the metal configuration of each representative; the configuration is encoded as an array with 8 elements, where the i-th element, corresponding to the i-th position in Fig. 4.1, is written as A or B when occupied by Pb or Sn, respectively.

Each supercell of CsPb$_{1-x}$Sn$_x$I$_3$ was relaxed with the same criteria used for unit cells (described in detail in Section 3.1) in exception for the number of divisions in the k-mesh, reduced from eight to four. The lattice parameter value a was retrieved for all the clusters and averaged using GQCA statistics as described in Section 2.3. The result is the lattice parameter as a function of composition at T = 300 K, plotted in Figure 4.2 as a solid line. The representative lattice constants are displayed as a scatter plot. Both the GQCA average and the cluster values closely follow Vegard's rule of linearity. Moreover, the cell dimensions for each configuration are seen to essentially depend of their overall composition, with neglectable changes between different metal configurations.
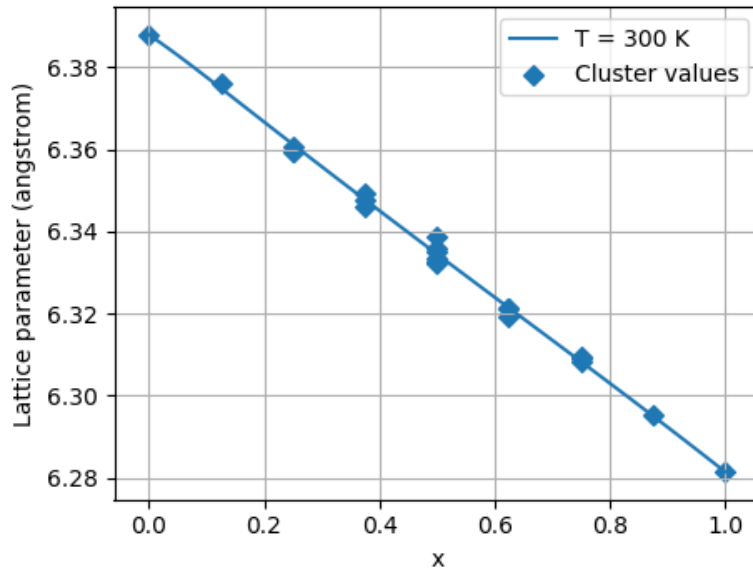
FIGURE 4.2 – Lattice parameter a for each cluster (scatter plot) and its GQCA average (solid line) at T = 300 K as a function of composition.

Besides the natural volume contraction expected with increasing tin content in lead perovskites, the octahedra also suffer from reshaping after relaxation. The two most relevant parameters to be studied in this case are ∠MIM' bonding angle and d$_{MI}$ bond length. For the α-CsPb$_{1-x}$Sn$_x$I$_3$ supercells, the lead-tin alloying distorts ∠MIM' only down to 179.91°, which is believed to be within the calculation error and does not convey much

physical information on the system. For comparison, unit cell calculations on $MASnI_3$ and $MAPb_3$ lead to bond angles as low as 170° and 168°, respectively (see Table 3.1). The Pb and Sn ions do not displace significantly from their ideal positions, while the iodine anions remain on the common line between adjacent metal cations. It is thus possible to neglect the bonding angle influence in the stability and electronic structure of the alloy.

The iodine anions still have one degree of freedom, which is their position along the $\overline{MM}'$ segment. The d_{MI} bonding length is strongly related to the identity of the two metal cations M and M' neighbors to I. Since tin ions have a somewhat shorter radius of 1.10 Å compared to lead's 1.19 Å (SHANNON, 1976; CHEN *et al.*, 2015), iodine shared between different elements will displace towards Sn. When, however, the iodine is split between two isotopes, it stays approximately halfway between M and M'. It this last case, $d_{MI} \approx a/2$ regardless of the nature of M. Therefore, the agglomeration of isotopes have the effect of limiting bond length relaxation. Let us define $d_{MI}(M')$ as the bond length between M and I, with M' being the second adjacent metal. Figure 4.3 shows, as a function of the number of tin ions, the bond length values found in all relaxed supercells. The bonds of different clusters were plotted together since their internal arrangements do not influence the bond length significantly. $d_{PbI}(Pb)$ and $d_{SnI}(Sn)$ are seen to follow a diagonal line between the values of d_{PbI} and d_{SnI} in the end components, echoing the lattice constant trend in Figure 4.2. $d_{PbI}(Sn)$ and $d_{SnI}(Pb)$, however, deviate strongly from the other bond values, since the broken symmetry allows the proper relaxation of the iodine ion position. $d_{SnI}(Pb)$ is ≈ 0.04 Å lower than $d_{SnI}(Sn)$, while $d_{PbI}(Sn)$ is larger than $d_{PbI}(Pb)$ by roughly the same amount. Notably, these two bond lengths are still modulated by the volumetric contraction with x, thus following a linear evolution.

The structural disorder in α-$CsPb_{1-x}Sn_xI_3$ is somewhat simple. Neither Cs, Pb or Sn ions significantly deviate from their ideal positions. The relaxation process is thus essentially contained in the iodine movement, which is limited to the line segment between metal ions.

4.3 Stability and cluster population

A more evenly mixed supercell increases the number of iodine anions shared between different metal cations. As discussed in the previous section, this allows the halogen to reduce the strain by approaching the Sn ion, contributing to the energy minimization of the cell. In this case, it is expected that these evenly mixed cells will have lower formation energies, increasing its probability of formation during the alloy fabrication. The objective of this section is to explore the relation between structure, excess energies, miscibility and cluster statistics. These factors will be correlated with the alloy susceptibility to oxidation,
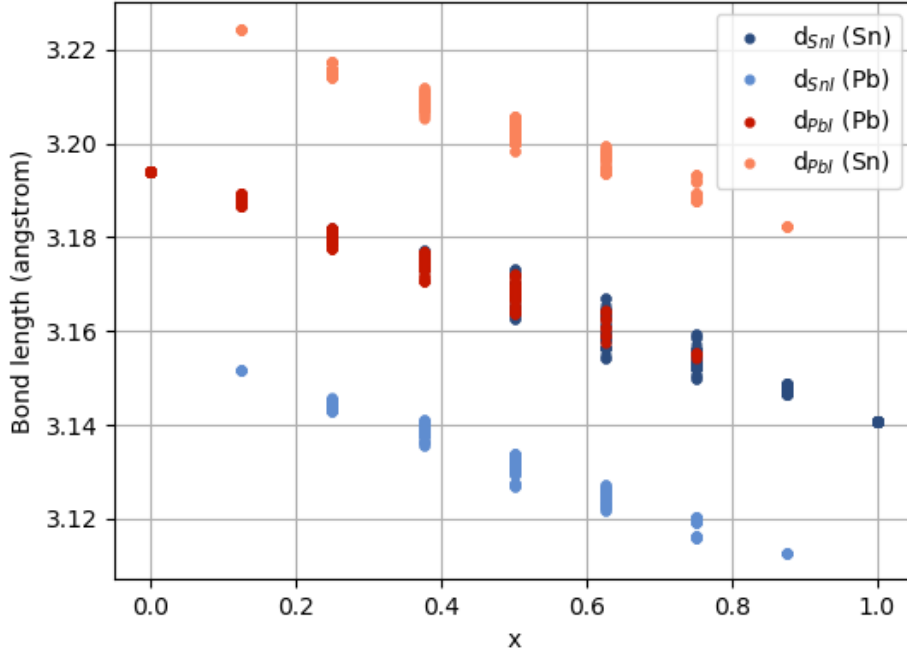
FIGURE 4.3 – Bond length values d$_{MI}$(M') as a function of composition, for M, M' $\in$ {Sn, Pb}.

a major research topic in tin-containing perovskite solar cells.

The excess energies as defined in 2.57 are obtained for each representative supercell and displayed in Figure 4.4. Interestingly, many supercell configurations have negative excess energies, indicating a propensity for ordering. Similar stable configurations were previously observed in the literature for APb$_{1-x}$Sn$_x$I$_3$, A = Cs, MA (FANG *et al.*, 2019; GUEDES-SOBRINHO *et al.*, 2019b). It is also noteworthy that the mixing enthalpies for CsPb$_{1-x}$Sn$_x$I$_3$ have very low absolute values, smaller that 3 meV per metal ion in comparison to values over 60 meV/metal observed by Guedes *et al.* for MAPb$_{1-x}$Si$_x$I$_3$. The colors of the plot in Figure 4.4 are specified according to the percentage of iodine ions present in the cluster that bond with similar metal cations. That is, values close to 100% indicate the formation of tin or lead-rich regions, whereas more evenly-mixed supercell configurations show values closer to 0%. The graph shows a consistent positive correlation between isotope agglomeration and excess energy when comparing supercells of same composition, as expected by the bond relaxation reasoning. This result indicates the stabilization of CsPbI$_3$ perovskites with Sn inclusion, agreeing with previous experimental observations which showed for a large number of cases that partial substitution of Pb by smaller ions can lead to more durable devices (SWARNKAR *et al.*, 2018).

Resistence of oxidation in Pb-Sn mixed perovskites has been first reported by Ogomi *et al.* (2014), and the detailed mechanism was later studied in depth by Leitjens *et al.*
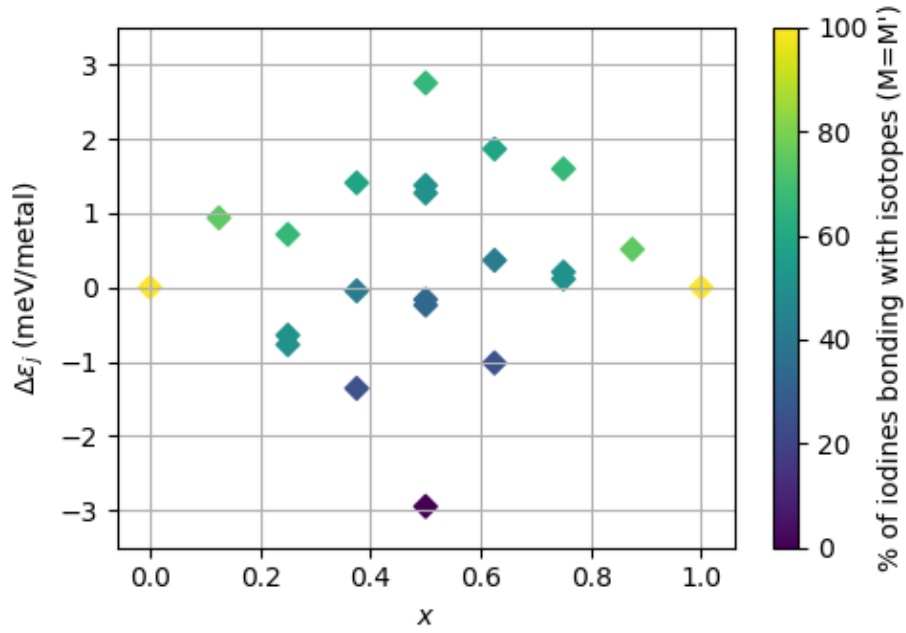
FIGURE 4.4 – Excess energies $\Delta\epsilon$ for each cluster as a function of composition. The colors are specified according to the percentage of iodines of the supercell shared between isotopes (M = M').

(2017). This last study found that the main oxidation path requires the presence of two adjacent Sn ions and is much less likely to occur in the presence of lead. At the same time, the calculated mixed enthalpies reveal that the alloy statistics inhibits the formation of Sn-rich regions. The hindering of tin oxidation is thus also influenced by the thermodynamics during the alloy fabrication. The thermal cluster distribution is expected to produce more stable perovskites than what would be expected from an ideal solution model.

With the objective of measuring the oxidation stability enhancement obtained from thermal distribution, a simple model is developed to calculate the probability of a random M', neighbor to any M = Sn, of also being a tin ion. Assume the spatial stacking of statistically-independent clusters, whose formation probability is defined by GQCA. Then, for each metal ion present in the cluster as defined in Fig. 4.1, there are three iodine anions shared with other metal cations within the cluster and three other iodines connected to the local environment. For a given metal ion M$_i$ (i = 1, 2, ..., 8) within cluster j, the vulnerability to oxidation V_i^j is defined as the normalized sum of probabilities

$$V_i^j = \frac{1}{6}\left(3x + \sum_{M'} \delta_{M',M_i}\right),\tag{4.1}$$

where x is the probability of a random metal ion in neighboring cells being Sn. The summation is executed over the three internal neighboors M' and δ_{M',M_i} equals 1 when M' = M$_i$ and is 0 otherwise. The summation in 4.1 accounts for the thermodynamical

effect in V$_i^j$. V$_i^j$ is then averaged over the Sn ions present in the cluster, and then the GQCA average is obtained as in Eq. 2.48:

$$V^j = \frac{1}{n_j} \sum_{M_i=Sn} V_i^j, \tag{4.2}$$

$$V(x,T) = \sum_j V^j x_j(x,T). \tag{4.3}$$

The value n$_j$ indicates the number of Sn ions within the j-th cluster. The complementary value $R(x,T) = 1 - V(x,T)$, related to the resistance to oxidation, is plotted in Figure 4.5 for T = 10 K, 300 K and T $\rightarrow \infty$.
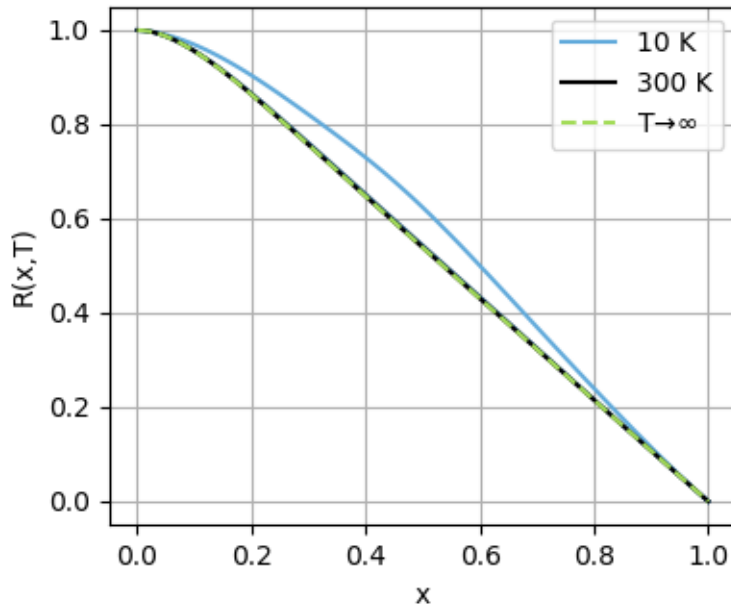
FIGURE 4.5 – Resistence to oxidation R(x, T) = 1 - V(x, T) for α-CsPb$_{1-x}$Sn$_x$I$_3$ at multiple temperatures. The dashed green line is obtained at the limit T $\rightarrow \infty$.

The curve for T $\rightarrow \infty$ represents the oxidation resistance values for the *a priori* cluster distribution (Eq. 2.52). For lower formation temperatures, R gets consistently higher due to the lower mixing enthalpy of more resistant clusters. The alloy gets considerably more resistant for extremely low temperatures of T = 10 K. However, the graph indicates that, for perovskite fabrication above room temperature (T > 300 K), the oxidation resistance is very close of that for T $\rightarrow \infty$ and, therefore, suffers little influence of thermodynamical effects. These results suggest that the enhanced stability observed in experiment is primarily attributed to ideal solution distribution, but that this effect can be significantly improved if the ordering tendency is leveraged.

Proceeding to the thermodynamical analysis, the mixed perovskite's miscibility can be evaluated in GQCA's framework by analyzing the Helmholt's free energy (2.53) as a

function of temperature. Figure 4.6 (left side) shows the alloy's mixing energy ΔE as a function of composition for temperatures ranging from 30 K to 240 K. The curve has a very distinct profile when compared to the values found for α-MAPb$_{1-x}$Sn$_x$I$_3$ using the same method (GUEDES-SOBRINHO *et al.*, 2019b). The methylammonium perovskite shows two minima near the end components, and a higher ΔE at intermediate compositions. On a completely opposite fashion, CsPb$_{1-x}$Sn$_x$I$_3$ has a single depression at x $\approx$ 0.5 and two local maxima near the end compositions. This distinct feature of the inorganic perovskite is due to the presence of many intermediate cluster configurations with negative excess energy, as depicted in Figure 4.4. The graph at the right side charts the mixing entropy ΔS curve for the same temperatures, presenting the usual shape and a rapid convergence to high-temperature behavior.
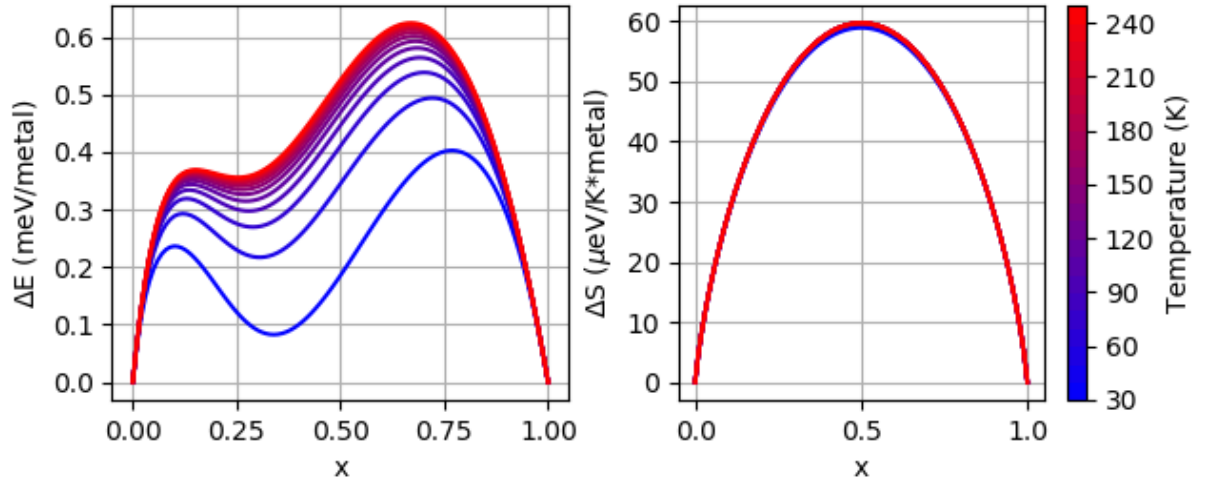
FIGURE 4.6 – Alloy's mixing energy ΔE and mixing entropy ΔS as a function of temperature and composition.

Once ΔE and ΔS are outlined the mixing free energy ΔF = ΔE $-$ TΔS curves are plotted in Figure 4.7. ΔF is convex even at low temperatures due to the single minima of ΔE centralized at intermediate compositions. It is, therefore, absent of binodal and spinodal decomposition regions above 30 K, meaning a remarkable miscibility between CsPbI$_3$ and CsSnI$_3$ perovskites. This is in contrast with other mixed perovskite materials as calculated by Guedes *et al.* (2019b). For comparison, MAPb$_{1-x}$Sn$_x$I$_3$ presents a miscibility gap for temperatures below 204 K.

4.4 Eletronic Structure

Now that the structural and thermodynamical features of CsPb$_{1-x}$Sn$_x$I$_3$ are known in detail, this section studies the electronic properties of its supercells.
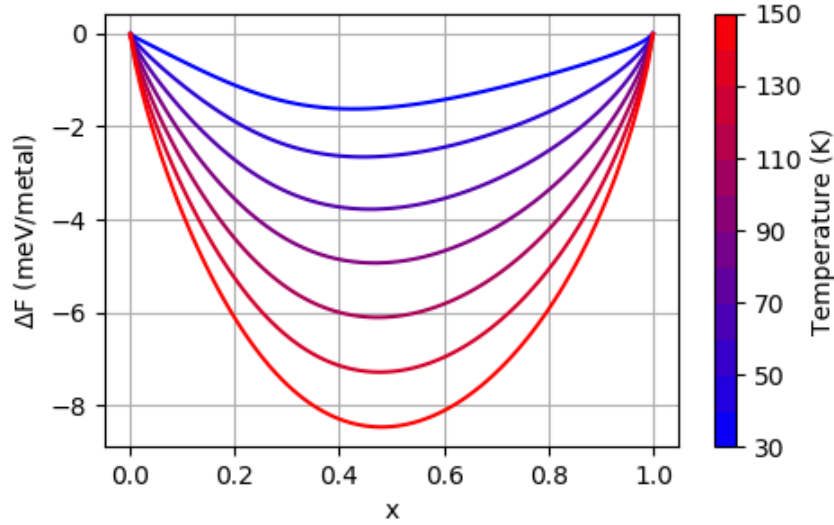
FIGURE 4.7 – Alloy's mixing free energy ΔF as a function of temperature and composition. The convexity of the curve implies the total miscibility between the mixed perovskite's components.

The band gap evolution with x in an alloy A$_{1-x}$B$_x$ is commonly modeled as a parabolic function in the form

$$E_g(x) = (1 - x) * E_g(0) + x * E_g(1) + bx(1 - x), \qquad (4.4)$$

where E$_g$(x) is the band gap as a function of composition x, and b is denominated the bowing parameter. Early experimental studies on methylammonium mixed tin-lead iodide perovskites (STOUMPOS *et al.*, 2013; OGOMI *et al.*, 2014; HAO *et al.*, 2014) showed the presence of a strong bowing, leading to gaps in intermediate compositions lower than those of the end components. Stoumpos *et al.* (2013) produced MAPb$_{0.25}$Sn$_{0.75}$I$_3$ perovskite showing a red-shift of 70 nm in comparison to MASnI$_3$ by measuring the photoluminescence emission peak, whereas the same samples showed optical absorption edges of 1.17 eV and 1.21 eV respectively. A subsequent publication by Ogomi *et al.* (2014) reported the first solar cells made of mixed tin-lead perovskites, which presented the same low optical absorption edge of 1.17 eV for MAPb$_{0.30}$Sn$_{0.70}$I$_3$. This anomalous behavior in MAPb$_{1-x}$Sn$_x$I$_3$ is a promising path for the electronic structure manipulation for high-efficiency solar cells, encouraging further research.

Stoumpos and coworkers published a density functional theory study in which they analyze the possible causes for the strong band gap bowing (IM *et al.*, 2015). They conclude that both the spin-orbit coupling effect and the structural distortion due to transition from cubic to tetragonal phases make up the non-linear trend. Eperon *et al.* (2016) reported similar calculations on MAPb$_{1-x}$Sn$_x$I$_3$. Their results pointed out that, under the ideal solution assumption, the gap obeys a linear trend, but the bowing would again reap-

pear if only the low-bandgap supercell configurations were selected for each composition. This would indicate the presence of short-range ordering in the alloy, even though they remark that the selected configurations are less stable. With the objective of resolving the conflicting premises found in literature, Goyal *et al.* (2018) publishes another *ab initio* study in which they argue that SOC, structural distortion and ordering should all be ruled out as possible explanations for the gap trend with composition. Instead, they show that in intermediate compositions the valence band maximum is primarily determined by Sn orbitals, whereas the conduction band minimum is composed of Pb orbitals. Thus, a small addition of tin in lead perovskites produces a sudden elevation of the VBM energy, consequently narrowing the band gap. Similar narrowing occurs as a result of the estabilization of the CBM with Pb-doping in MASnI$_3$, which causes the gap bowing.

The same atypically strong bowing was later observed in other tin-lead mixed perovskites APb$_{1-x}$Sn$_x$X$_3$ with a multitude of A-cation and halogen combinations (PRASANNA *et al.*, 2017; PISANU *et al.*, 2018; RAJAGOPAL *et al.*, 2019). A recent experimental research by Rajagopal and others quantified the bowing parameter b for iodine alloys with FA, MA, Cs, FA$_{0.8}$Cs$_{0.2}$, MA$_{0.8}$Cs$_{0.2}$, MA$_{0.5}$FA$_{0.5}$ and MA$_{0.8}$GA$_{0.2}$ occupying the cuboctahedral cage. In every case, the lowest band gap values were found for tin-rich intermediate compositions. The microstrain, composed of a conjunction of octahedral distortion and octahedral tilting, is found to be correlated to the magnitude of b. Nevertheless, the same research concludes that the non-linearity in gap evolution should occur even in the absence of lattice distortion, possibly due to chemical effects as postulated by Goyal's group. The purpose of this section is the study of band gap of cubic CsPb$_{1-x}$Sn$_x$I$_3$, which is then expected to give insights on the nature of bowing in tin-lead perovskite alloys. Given the absence of octahedral tilting and ∠MXM' distortion, the microstrain in this material is primarily related to the d$_{MX}$ distortion caused by iodine displacement, simplifying the problem. The developed calculations will contribute to the aforementioned discussion by presenting gap values with a good correction method and by including orbital, structural and thermodynamic considerations.

The DFT and DFT-1/2 corrected band gaps for the unit cell calculation of end components, as obtained in Chapter 3, are displayed in Table 4.2. The CUT parameters used were 3.20 a.u. for the I$_p$ orbital in CsPbI$_3$ and 3.05 a.u. for the same orbital in CsSnI$_3$. Experimental and *ab initio* GW values found in literature are also shown for comparison. To evaluate accurately the precision of DFT-1/2 method, the table includes the band gap for both cubic and orthorhombic phases when available. The gap of α-CsPbI$_3$ indicated (1.48 eV) was measured by Sutton *et al.* (2018) using linear extrapolation to 0 K of the evolution of its absorption onset with temperature. DFT-1/2 results in the close value of 1.32 eV, a more accurate result than the GW gap of 1.14 eV. Both the GW and experimental values for the γ phase corroborates with the observation that high-symmetry phases

lead to smaller band gaps. As for CsSnI$_3$, DFT-1/2 (1.02 eV) results are comparable to GW (1.008 eV). Huang *et al.* (2016) realized a second GW calculation for the γ phase using the same method, obtaining a value of 1.3 eV in comparison to the experimental gap of 1.27 eV. The success of the GW method in predicting the gap of γ-CsSnI$_3$ endorses the DFT-1/2 results for the cubic phase. Finally, the DFT-1/2 method provides a significant correction compared to the underestimated GGA gap and an accuracy comparable to the GW method, validating its use for the subsequent supercell calculations.

TABLE 4.2 – Band gap values for unit cell DFT, DFT-1/2 and GW calculations and experimental measurements for CsPbI$_3$ and CsSnI$_3$ in cubic (α) and orthorhombic (γ) phases.

Perovskite	DFT	DFT-1/2.	GW	exp.
α-CsPbI3	0.25	1.32	1.14 [a]	1.48 [a]
γ-CsPbI3			1.57 [a]	1.73 [b]
α-CsSnI3	0.07	1.02	1.008 [c]	
γ-CsSnI3			1.3 [c]	1.27 [d]

[a](SUTTON *et al.*, 2018); [b](EPERON *et al.*, 2014); [c](HUANG; LAMBRECHT, 2016); [d](SABBA *et al.*, 2015).

For the supercell calculations, the CUT parameter was fixed as the average of the CUT values for the end components (3.125 a.u.). Figure 4.8 shows the resultant thermodynamically averaged band gap as a function of composition at the temperatures of 300 K (solid line) and 10 K (dashed line). The expected strong bowing is evidenced by these results. A value of $b = 0.582$ eV for T = 300 K is found by numerical fit to the function defined in 4.4. This value is remarkably close to the bowing parameter of $b = 0.57 \pm 0.06$ eV determined experimentally for γ-CsPbSnI$_3$ (RAJAGOPAL *et al.*, 2019). At this temperature, the calculated gap curve reaches a minimum of 0.984 eV at the composition of x$_{min} = 0.80$, 0.033 eV lower than the gap of CsSnI$_3$. This difference is comparable to a narrowing of 0.04 eV between the band gaps of MASnI$_3$ and MAPb$_{0.25}$Sn$_{0.75}$I$_3$ (STOUMPOS *et al.*, 2013).

Besides the GQCA average, Figure 4.8 shows the individual gap values of the 22 cluster configurations of the alloy as a function of its fractional tin composition. The color of each cluster value is related to its excess energy. It is evident from the graph that, for each fixed composition, the supercell configurations with the narrower gaps are less stable. Configurations 5 and 16, both with 4 tin ions within the supercell, have band gaps of 0.952 eV and 1.103 eV and excess energies of 22.0 meV and -23.6 meV (per supercell), respectively. This rule is valid for all clusters, and it casts doubt on the hypothesis that short range ordering can cause the bowing. On the contrary, the graph shows that, at lower manufacturing temperatures - a condition that is more prone to ordering -, the bowing is less intense.

With the objective of understanding the mechanisms determining the band gap, a
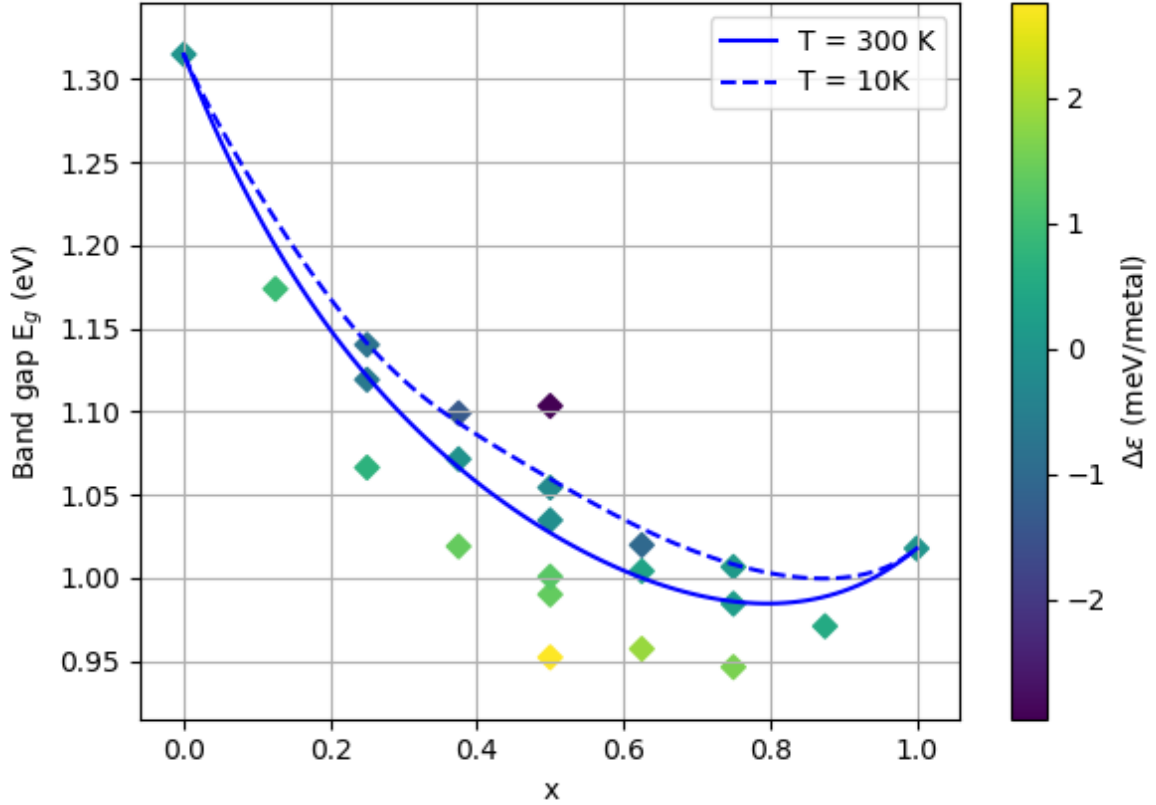
FIGURE 4.8 – Band gap E$_g$ for each cluster (scatter plot) and its GQCA average for T = 10 K (dashed line) and 300 K (solid line) as a function of composition x. The colors are specified according to the cluster's excess energy $\Delta\epsilon$.

closer look into the electronic structure is necessary. The average M$_s$ orbital character at the VBM for each cluster, as well as the M$_p$ orbital at the CBM, is shown in Figure 4.9. Regardless of the composition or cluster configuration, the Pb$_s$ character is consistently more prevalent at the conduction band, since the Pb$_p$ atomic orbital is more stable than Sn$_p$. The opposite is found at the valence band, in which Sn$_s$ character is stronger than Pb$_s$. This indicates that the VBM and the CBM energy levels are determined respectively by the CsSnI$_3$ and CsPbI$_3$ bands, which is a possible cause for the gap bowing as proposed by Goyal *et al.* (2018). A small incorporation of Pb in CsSnI$_3$ would lead to a sudden stabilization of the CBM energy, narrowing the gap. Also, the orbital character shows a tendency for charge separation: the thermally excited electrons will likely concentrate in Pb-rich regions, while the vacancies will accumulate around Sn ions, hindering carrier recombination. This property is valuable for solar cells, enhancing its quantum efficiency.

The chemical aspect of the gap bowing is also closely related to the atomic arrangement. Given the relation between $\Delta\epsilon$ and metal arrangement as previously discussed, Figure 4.9 shows that, between isocompositional clusters, higher isotope agglomeration is associated with a more accentuated Sn and Pb character at their respective bands. This

effect is a possible explanation for the gap narrowing in supercells with higher $\Delta\epsilon$ as seen in Figure 4.8, and is responsible for enhancing the band gap bowing. For illustration, consider the valence band maximum character of the two supercell configurations depicted in Figure 4.10. The grey and black circles represent tin and lead ions, respectively, and their radii are scaled to denote the ion-projected M$_s$ orbital character at the VBM. In the supercell at the left, the two Sn ions are adjacent and the tin character is much more substantial than the Pb character. In the second configuration, there are no two adjacent isotopes, and the orbital character is more evenly distributed between Pb and Sn ions. A similar rule occurs at the CBM, in which the Pb character is more present in the first supercell and better distributed in the latter. The first supercell configuration then presents both a lower E$_g$ and a higher $\Delta\epsilon$ than the second configuration. This rule is observed between the isocompositional supercells of any x.
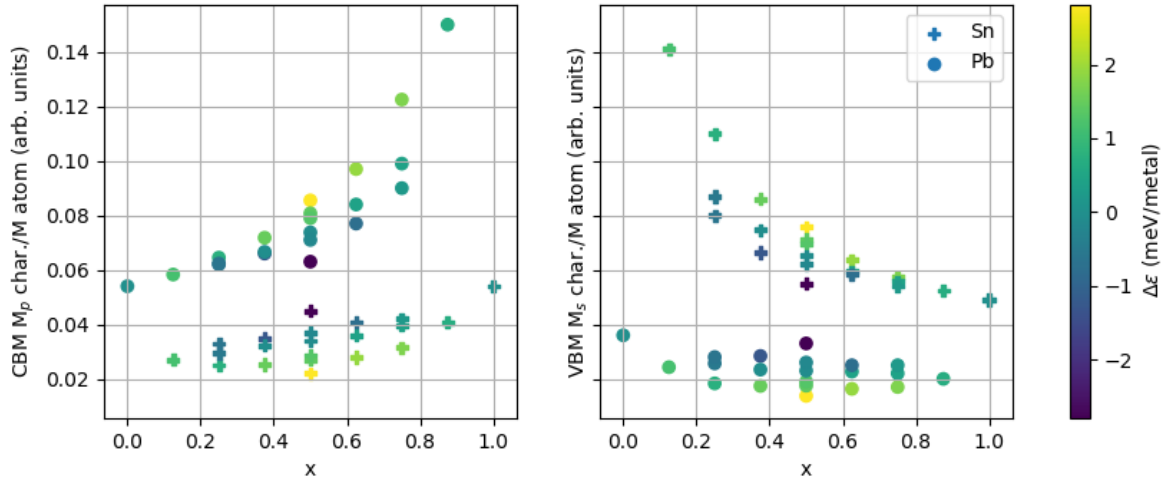
FIGURE 4.9 – Average M$_p$ and M$_s$ orbital character at the CBM (left) and the VBM (right), respectively, as a function of cluster composition. The colors indicate the cluster's excess energies $\Delta\epsilon$.

Finally, it is necessary to determine the influence of spin-orbit coupling in the band gap. The SOC affects in special the conduction band of metal halide perovskites due to the prevalence of M$_p$ character. Without SOC (no-SOC for short), the CBM is triply degenerate, each band associated to one of p$_x$, p$_y$ or p$_z$ orbitals. When relativistic effects are taken into consideration, the CBM splits into two p$_{\frac{3}{2}}$ bands and a p$_{\frac{1}{2}}$ lower-energy split-off band. The stabilization of the p$_{\frac{1}{2}}$ band is responsible for a strong band narrowing in Pb-based perovskites. The same effect is found for tin perovskites, but in lower magnitude since it is a lighter atom. On the other hand, the valence band, primarily composed of halogen orbitals, is less affected. Figure 3.7 illustrates these effects by comparing the band structures of CsPbI$_3$ with and without considering spin-orbit coupling.

Figure 4.11 shows for comparison the DFT-1/2 band gap curve at T = 300 K with and
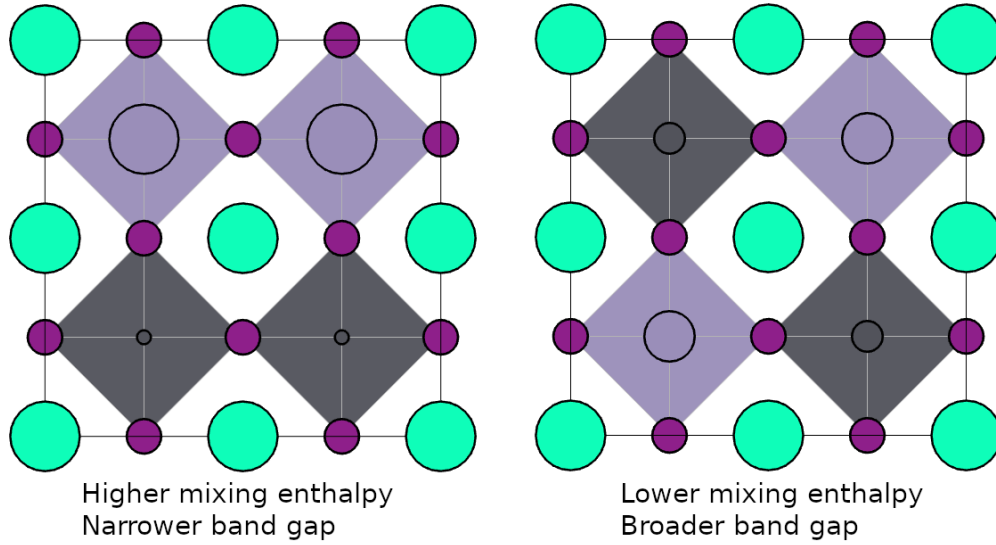
FIGURE 4.10 – Comparison of mixing enthalpy, bandgap and VBM M$_s$ orbital character between two isocompositional supercell configurations. The amplitude of the projected M$_s$ character is proportional to the circle's radius drawn over each octahedron. Green, purple, light gray, and black circles represent Cs, I, Sn, and Pb ions, respectively.

without SOC. In no-SOC calculations, the band gaps broaden by 1.25 eV and 0.40 eV with relation to SOC for CsPbI$_3$ and CsSnI$_3$ respectively. The accentuated band gap bowing vanishes. Instead, the band gap evolution of the clusters from j = 1 to 21 follow a linear behavior, with cluster j = 0 (corresponding to CsPbI$_3$), deviating from this tendency. This result is compatible with that reported by Im *et al.* (2015), with the exception that, in this case, structural deformation and phase transition are not determinant factors.

To further investigate the influence of SOC on the gap bowing, the orbital character of the CBM and VBM were analyzed as well for no-SOC calculations. The metal M$_s$ character at the VBM is very similar to the one depicted in Figure 4.9b, with a prevalence of Sn character throughout all compositions. The CBM, however, showed a very different profile, as can be seen in Figure 4.12. The CBM character in no-SOC band structure has a higher presence of tin orbitals, in contrast to the SOC results shown in Figure 4.9. Therefore, without SOC both the VBM and CBM are strongly defined by Sn orbitals, which explains the stronger band gap narrowing with the addition of a single tin ion to the CsPbI$_3$ 8-fold supercell (j = 0 → j = 1), and also explains the absence of narrowing with the inclusion of one Pb ion to the CsSnI$_3$ supercell, an effect observed in SOC calculations. This exchange in metallic character can be explained in terms of the atomic energy levels of the outermost p orbitals of tin and lead atoms which compose the conduction band. Toggling on SOC stabilizes the Sn$_p$ level from -4.0 eV to -4.2 eV for p$_{\frac{1}{2}}$, and takes Pb$_p$ from -3.8 eV (higher than Sn$_p$) to -4.9 for p$_{\frac{1}{2}}$ (lower than tin p$_{\frac{1}{2}}$) (GOYAL *et al.*, 2018). It is thus reasonable to conclude that the spin orbit coupling is an essential feature for the
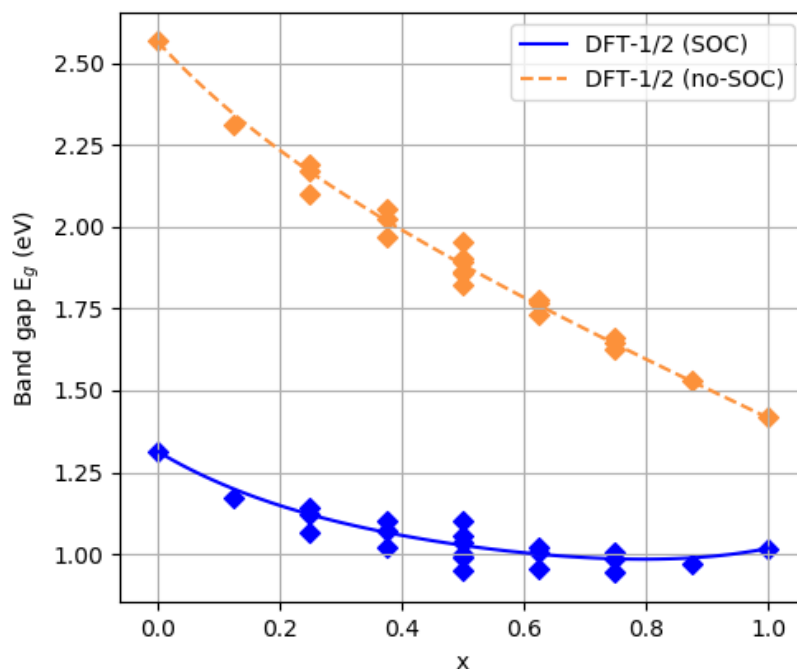
FIGURE 4.11 – Band gap E$_g$ as a function of composition considering SOC (blue) and without considering SOC (yellow). The individual cluster values are depicted as a scatter plot, and the GQCA averages at T = 300 K are shown as a line plot.

presence of band gap bowing.

4.5 Conclusion

The analysis accomplished in this chapter allowed for a comprehensive understanding of the properties of CsPb$_{1-x}$Sn$_x$I$_3$. The study of the crystal's lattice, cluster configuration, bonding, mixing enthalpy, band gap, charge separation and orbital character were integrated, and the physical relationships between these variables were investigated.

The structural deformation due to alloying was primarily attributed to the stretching of Pb-I bonds and the contraction of Sn-I bonds when compared to Vegard's law, while still maintaining linearity in the MIM' chain. This deformation is responsible for the stabilization of cluster configurations with evenly distributed metal ions, configurations which are known to improve oxidation resistance. A measure of oxidation resistance based on the fraction of iodine ions shared between metals of different identities was proposed, and the measurement of this quantity indicated that low-temperature fabrication methods can lead to solar cells less susceptible to deterioration. A detailed look into the thermodynamics of the solid solutions showed an unusual profile of the mixing enthalpies of different supercells configurations. The mixed perovskite then demonstrated a perfect miscibility, a feature that was not found for other perovskite alloys.
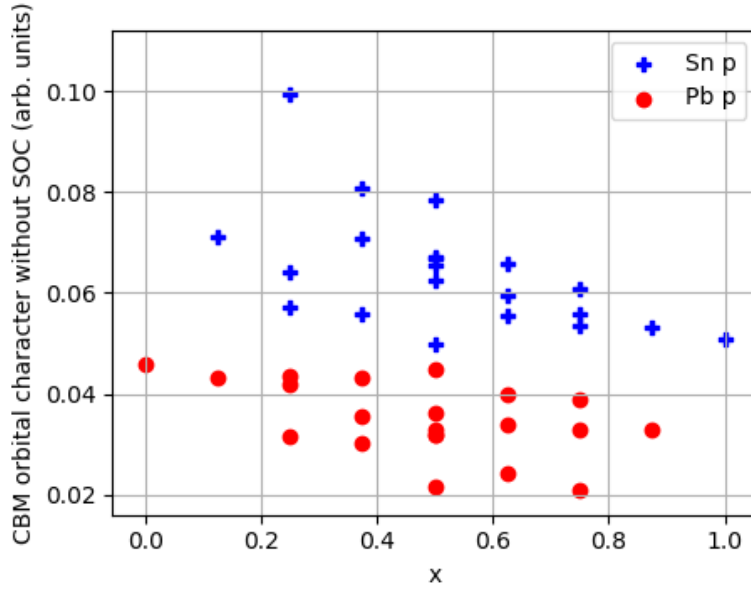
FIGURE 4.12 – Average Pb$_p$ and Sn$_p$ orbital character at the CBM as a function of composition for no-SOC calculations.

Thereafter, the electronic structure of CsPb$_{1-x}$Sn$_x$I$_3$ was explored in detail. The quantitative results obtained are in great accordance with experiment, thus validating the methods employed. The band gap evolution with composition demonstrated a strong bowing, with intermediate tin-rich compositions having narrower band gaps than the end components. For x = 0.80, the alloy is predicted to have a band gap of 0.984 eV, 0.033 eV lower than the gap of CsSnI$_3$. Such behavior is a common effect between tin-lead perovskites. The bowing parameter was calculated with a parabolic fit, giving a value of $b = 0.582$ eV, comparable to the value of $b = 0.57 \pm 0.06$ eV obtained experimentally for the orthorhombic phase. The many proposals for the origin of such bowing found in previous literature were carefully investigated. Short-range ordering claims were ruled out, since the more stable configurations would, in fact, show a weaker bowing. The inspection of metal orbital character revealed that the valence and conduction bands were originated from different metals, which explains the band gap narrowing with small Pb inclusion in CsSnI$_3$. The strong spin-orbit coupling in Pb with relation to Sn has a determinant role in this chemical arrangement. Thus, it is inferred that the band gap bowing is originated from an unusual arrangement of atomic levels, which is only possible due to SOC effects.

The aforementioned analysis and results are expected to play an important role in understanding the underlying physics of tin-lead mixed perovskites in general. Also, the calculations show to be accurate when compared to experiment and make relevant predictions on the properties of α-CsPb$_{1-x}$Sn$_x$I$_3$.

5 CsSn$_{1-x}$Ge$_x$I$_3$ - Towards efficient lead-free devices

5.1 Motivation

The replacement of toxic lead in metal halide perovskite solar cells is a theme of great research interest. The operation conditions to which solar panels are commonly exposed can cause device deterioration and consequently contaminate the environment, posing a high risk to human health (BABAYIGIT *et al.*, 2016). With the objective of tackling this issue, alternate compositions based on Sn^{2+}, Ge^{2+}, Sb^{3+}, Bi^{3+} and a myriad of other cations have been proposed (SHALAN *et al.*, 2019), even though they commonly present much lower power conversion efficiency (PCE) when compared to lead-based materials. Any potential substitute of MAPbI$_3$ must rival its optoelectronic properties, such as its relatively low band gap of 1.57 eV and small carrier effective masses (EPERON *et al.*, 2014; GALKOWSKI *et al.*, 2016).

Numerous publications focus on the first-principle study of perovskites in search for adequate photoactive materials (MAO *et al.*, 2018; KRISHNAMOORTHY *et al.*, 2015; QIAN *et al.*, 2016). Qian *et al.* (2016) assessed 48 different compositions, between which CsGeI$_3$ stood out as the best candidate. Using the Spectroscopic Limited Maximum Efficiency method (YU; ZUNGER, 2012), they obtained the theoretical limit of 27.9% for its PCE, compared to 26.7% for MAPbI$_3$. This result was a consequence of a suitable optical absorption function, which, alongside the balanced and reduced carrier masses, acknowledges CsGeI$_3$ as a promising candidate for solar cell research. Krishnamoorthy *et al.* (2015) also identified the high potential of Ge-based perovskites and devised the earliest reported CsGeI$_3$ solar cell, obtaining a PCE of 0.11% with a 1.63 eV band gap. Despite its competent intrinsic characteristics, germanium, as well as tin, is known for suffering rapid oxidation from Ge^{2+} to Ge^{4+}, leading to low efficiencies.

Effort in enhancing CsGeI$_3$-based solar cells are justified by the several advantages this material presents besides its absorption properties. The absence of a volatile molecule in its composition leads to a much higher thermal stability when compared to MAGeI$_3$ and

FAGeI$_3$ (KRISHNAMOORTHY *et al.*, 2015). Moreover, it is stable in the rhombohedral phase at ambient temperature (THIELE *et al.*, 1987; STOUMPOS *et al.*, 2015), whereas CsPbI$_3$ and CsSnI$_3$ tend to degrade to an optically inactive yellow phase (KONTOS *et al.*, 2016; SUTTON *et al.*, 2018). The susceptibility to oxidation is thus the major stability challenge of Ge-based solar cells.

This scenario has suddenly changed with the recent report by Chen *et al.*, in which a CsSn$_{0.5}$Ge$_{0.5}$I$_3$ device delivered a PCE of 7.1%, a high conversion efficiency value amongst the lead-free perovskite solar cells reported so far (CHEN *et al.*, 2019). The device showed a higher resistance to oxidation compared to the pristine CsSnI$_3$ and CsGeI$_3$. Such enhanced stability was attributed to the surface passivation due to the formation of native-oxide layer when in contact with air.

The objective of this chapter is to present an in-depth study of CsSn$_{1-x}$Ge$_x$I$_3$ mixed perovskite. To the best of the author's knowledge, this is the most detailed account of this alloy reported so far. Using the same methods previously addressed, the microscopical geometry, solid solution thermodynamics, and electronic structure are calculated and discussed. The intrinsic characteristics of this material are obtained over the entire composition range, offering opportunities and insights for the improvement of related photovoltaic devices.

5.2   Symmetry and geometrical parametrization

CsSnI$_3$ and CsGeI$_3$ crystallize at room temperature into orthorhombic and rhombohedral structures respectively, so phase transition should occur when adjusting the composition of the mixed system CsSn$_{1-x}$Ge$_x$I$_3$. In this chapter, the rhombohedral system is assumed in all supercell calculations, which is believed to be the symmetry of most interest due to a series of factors. Firstly, at higher temperatures CsSnI$_3$ crystals can assume the aristotype cubic structure (YAMADA *et al.*, 1991), closely related to the rhombohedral structure, whereas CsGeI$_3$ does not assume the orthorhombic phase. Also, the fabricated perovskite with x = 0.5 was identified as rhombohedral by XRD measurements (CHEN *et al.*, 2019). Lastly, the germanium perovskites are more promising for solar cell application than tin-based materials, so, in principle, the Ge-rich compositions are of greater research interest.

The adopted rhombohedral primitive cell is depicted in Figure 5.1a. In simple terms, it can be described as a cubic cell stretched along the [1,1,1] direction - the so-called triad axis. The square angles between the cell edges are narrowed down to a value β, and the MX$_3$ octahedron is distorted. Moreover, the M cation slides along the triad axis from the centre of the octahedron, which is responsible for the breaking of inversion symmetry. The

parameter δ will be defined as the dislocation of M from the equidistant point between two Cs cations. The M cation then comes closer to three of the surrounding halogen anions, forming a trigonal pyramidal MX$_3$ unit with MX bonding distance d$_S$ and d$_L$ to the closest and farthest halogens, respectively. Considering X and X' opposite vertices of the octahedron, the $\angle$XMX' angle consequently deviates from the value of 180° found in the regular cubic structure. These parameters are highlighted in Fig. 5.1b and will be of interest in the next section when analyzing the cell relaxation.

The described primitive cell is classified within the Space Group 160 (R3m). Supercells for alloy calculations are defined as shown in Figure 5.1c, with 8 unit cells each and 40 atoms in total. There are consequently 8 octahedron centered either by a tin or germanium cation, and each octahedron is numbered from 1 to 8. In principle, there are $2^8 = 256$ supercell configurations. Using the Space Group symmetry operations, the set of possible configurations was parsed into 22 groups of degenerate supercells. As can be seen in Table 5.1, the results are identical to those obtained for the cubic structure in Chapter 4. One representative configuration for each group is selected, and its metal arrangement is encoded as a list of letters. If the i-th element of the list is the letter A (B), the i-th octahedron is centered by a Sn (Ge) ion.

TABLE 5.1 – Symmetry information on the 22 groups of degenerate 8-fold supercells of rhombohedral CsSn$_{1-x}$Ge$_x$I$_3$. The supercells are numbered from j = 0 to j = 21. The degeneracy g$_j$ and the number of Ge ions is displayed. The internal atomic arrangement of a representative supercell is represented by a list of letters, where the i-th letter is A or B when the i-th metal position is occupied by a Sn or Ge ion, respectively.

j	g$_j$	# Ge	Configuration 12345678	j	g$_j$	# Ge	Configuration 12345678
0	1	0	AAAAAAAA	11	24	4	BBBABAAA
1	8	1	BAAAAAAA	12	24	5	BBBBABAA
2	12	2	BBAAAAAA	13	6	4	BABAABAB
3	12	2	BABAAAAA	14	24	5	BBBABAAB
4	24	3	BBABAAAA	15	12	6	BBBBABBA
5	6	4	BBBBAAAA	16	2	4	BABABABA
6	8	3	BABABAAA	17	8	5	BBBABABA
7	8	4	BBABABAA	18	12	6	BBBBBABA
8	4	2	BAAAAAAB	19	4	6	BBBABBAB
9	24	3	BABAABAA	20	8	7	BBBBBBBA
10	24	4	BBBAABAA	21	1	8	BBBBBBBB

FIGURE 5.1 – Depiction of (a) the R3m unit cell, showing the MX$_6$ octahedron faces; (b) the d$_L$, d$_S$ and ∠XMX' parameters, with the shorter bonds forming a MX$_3$ trigonal pyramidal form; and (c) the 2x2x2 rhombohedral supercell used for alloy calculations.

5.3   Structural relaxation

The microscopic arrangement of perovskite materials plays a crucial role in determining their electronic properties. Obtaining the lattice and equilibrium atomic positions is the first step in understanding any key factor that determines the quality of an active layer of solar cells, such as stability, band gap, orbital signature of bandstructure, and carrier effective mass. Not as simple as their cubic counterparts, rhombohedral perovskites have a much richer complexity in its internal structure, and the relations between its diverse geometrical parameters must be studied with care. The objective of this section is to provide a rational basis for the structural analysis of mixed rhombohedral perovskites, as well as to offer some insights on the particular characteristics of CsSn$_{1-x}$Ge$_x$I$_3$.

First, the primitive cell of pure compounds CsSnI$_3$ and CsGeI$_3$ are investigated in both cubic (α-) and rhombohedral (r-) structures, with the objective of understanding the differences and similarities between both forms. r-CsSnI$_3$ and r-CsGeI$_3$ structures were initialized with parameter values a = 6.10 Å, β = 88.46°, δ = 0.342 Å, d$_S$ = 2.80 Å, d$_L$ = 3.34 Å and ∠XMX' = 168.2°. These values were chosen to match the relaxed

structure of r-CsGeI$_3$ as found in the Materials Project Database (JAIN *et al.*, 2013). The atomic positions of each cell were then relaxed with the same VASP parameters as used in the previous chapter for CsPb$_{1-x}$Sn$_x$I$_3$. The results are displayed in Table 5.2.

TABLE 5.2 – Geometrical parameters of relaxed structures of rhombohedral and cubic CsGeI$_3$ and CsSnI$_3$ perovskites compared with experimental data. The output VASP energy E is given in units of eV/atom.

Perovskite	Structure	a	β	δ	d$_S$	d$_L$	$\angle$XMX'	E
	r	6.12	88.32	0.353	2.79	3.36	167.8	-2.96755
CsGeI3	r (Exp.)[a]	5.983	88.62	0.31	2.7526	3.2561	169.31	
	α	6.00	90.0	0	3.0	3.0	180.0	-2.42183
	α (Exp.)[b]	6.05						
	r	6.28	89.9	0.03	3.11	3.17	178.5	-2.95212
CsSnI3	α	6.28	90.0	0	3.14	3.14	180.0	-2.95217
	α (Exp.)[c]	6.219						

[a](STOUMPOS *et al.*, 2015); [b](THIELE *et al.*, 1987); [c](YAMADA *et al.*, 1991).

The calculated lattice parameters for r-CsGeI$_3$ and α-CsSnI$_3$ were overestimated with relative errors of 2.2% and 0.9%, respectively, showing good agreement to experimental data. In the former case, the additional calculated geometrical parameters also show a remarkable agreement to X-ray diffraction data, although presenting a somewhat larger rhombohedral distortion. On the other hand, the r-CsSnI$_3$ perovskite spontaneously relaxes towards the cubic symmetry. This is expected due to the higher stability of the cubic system in tin perovskites and the proximity between both polymorphs. The output total energy per atom E is also shown for each material. As expected, r-CsGeI$_3$ has a lower formation energy than α-CsGeI$_3$, evidencing a higher stability of the former. The α-CsSnI$_3$ is slightly more stable than r-CsSnI$_3$.

Next, the alloy's representative supercells were relaxed from the same initial conditions until reaching equilibrium. The same DFT parameters for primitive cell calculations were used, in exception for the sampling of the first Brillouin zone that is changed to 4 divisions along the reciprocal vector directions. The composition-dependence of the geometrical parameters were obtained and will now be analyzed. Fig. 5.2 shows both the values of lattice parameter a and lattice angles β as a function of composition. Each cluster has three values of a and β as a consequence of the tridimensional geometry, so the data points shown correspond to the average value within each cluster. The GQCA average of the lattice parameter presents a slight downward curvature with increasing Ge content, specially in the region x > 0.875. The lattice angles also depart from linearity in this region, whereas following a linear evolution for x<0.875. This suggests a connection between both parameters. Moreover, the lattice angles are seen to continuously increase towards the ideal cubic value of $\beta = 90°$ for tin-rich compositions, indicating a continuous
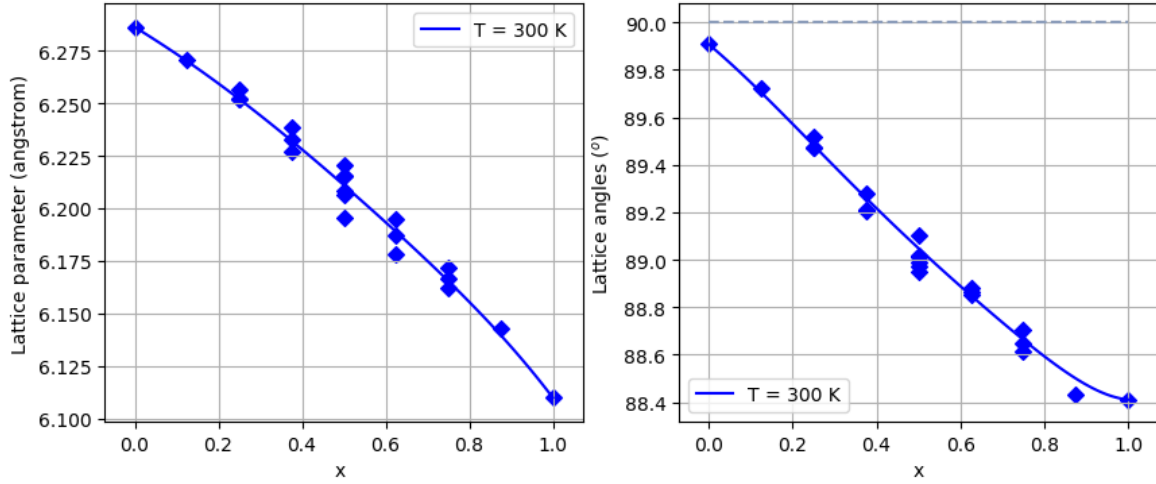
transformation between lattice systems with x.

FIGURE 5.2 – Graphs showing (left) lattice parameter a as a function of composition x, with the individual cluster values shown as a scatter plot and the average GQCA values for T = 300 K represented as a solid line; and (right) the three lattice angles β of each cluster as a function of x.

Due to the potentially chaotic behavior of the microstructure of alloys, some preliminary simplifications are necessary. The rhombohedral perovskites present linear CsM chains along the triad axis, as can be seen in Fig. 5.1a. The calculations reveal that the Cs-Cs distance along those chains remains within 0.2% of its ideal value. Also, the $\angle Cs_1Cs_2Cs_3$ angle remains essentially straight, having a maximum distortion of 0.4° for three consecutive Cs cations. It is thus reasonable to neglect deviations of the Cs cations from their ideal positions, and so the relaxation effects are assumed to take place within the MX framework primarily.

Similarly to CsPb$_{1-x}$Sn$_x$I$_3$, the iodine anions in CsSn$_{1-x}$Ge$_x$I$_3$ are disputed between Sn and Ge and naturally lie closer to the latter due to its shorter radius. This competition moves both metal and halogen ions from their ideal positions. The resulting M off-centering δ also holds an important relation with the perovskite's electronic properties. It is responsible for breaking the nonbonding equilibrium of M$_p$-X$_p$ orbital interaction at the conduction band minimum and subsequently enlarging the bandgap, as will be explored in Section 5.5, and for removing the inversion symmetry, which is commonly associated with a lower bimolecular recombination due to Rashba splitting (AZARHOOSH et $al.$, 2016). Since δ is directly influenced by halogen competition, it is necessary to take into account the immediate vicinity of the octahedron. Suppose that N$_M$ is the number of octahedra centered by M ions that surround a given ion of same chemical element M. If, for example, N$_{Ge}$ = 6 (= 0), it means the respective GeI$_6$ octahedron is completely surrounded by 6 Ge- (Sn-) centered octahedra. In Figure 5.3, δ is plotted for each of the 8 octahedra of each cluster as a function of cluster composition x. Data points of Sn and Ge ions are

represented by crosses and circles, respectively, and their color correspond to the value of
N_M. Several conclusions can be taken from this plot. As expected, the germanium ions
present consistently higher δ than tin ions. Also, its value its strongly influenced by the
neighboring elements. The higher the number of surrounding Sn ions (lower N_M for Ge
and higher N_M for Sn), the lower is δ. For Sn-centered octahedron surrounded by 6 other
tin ions δ is cut down to less than 0.1 Å, which indicates that even a relatively small
agglomeration of Sn ions could induce a local transition to the cubic symmetry. Also, δ is
not significantly influenced by the supercell composition x for fixed values of N_M, which
shows some insensibility to change in lattice constant.

Even though the M displacement is ideally aligned with the triad axis as seen in
Fig. 5.1a, the complicated equilibrium of forces can cause M to leave the axis and slightly
break the rhombohedral symmetry of the primitive cell. However, similarly to pseudocubic
perovskites, this local symmetry breaking should be null when averaged over the range of
a sufficiently large sample of unit cells.
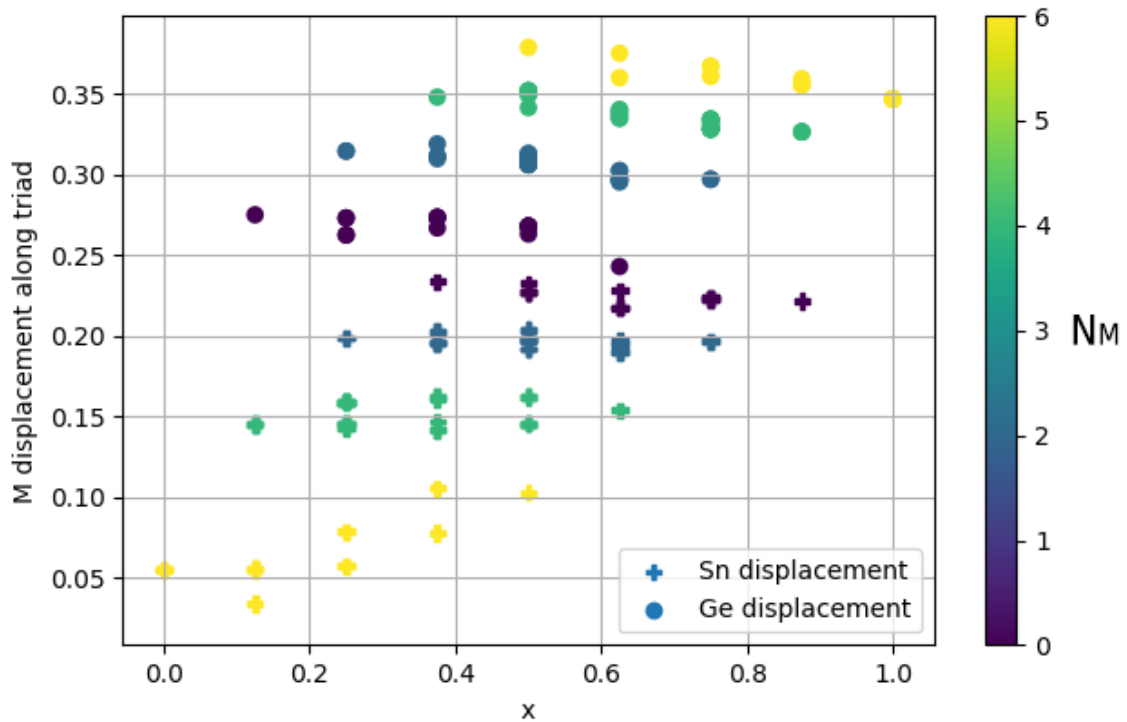
FIGURE 5.3 – M ion displacement δ of each octahedron for every cluster as a function
of its composition x. The colors of data points are assigned accordingly to the number of
neighboring isotopes.

Both metal and halogen displacements are the cause of the asymmetry between short
and long bonds in the MX arrays. With the objective of classifying and effectively un-
derstanding the bonds, the iodine ions can be divided into four types regarding their first
neighbors: those (i) placed between Ge ions, (ii) placed between Sn ions, (iii) forming a

long bond with a Ge ion and a short bond with a Sn ion, and (iv) forming short (long) bond with a Ge (Sn) ion. Each type of iodine naturally forms one short bond d$_S$ and one long bond d$_L$, resulting in a total of 8 categories of bonds. Next, each category is analyzed and quantified with respect to the alloy's composition.

Consider a linear infinite array M$_1$XM$_2$XM$_3$X... along a given primitive lattice vector direction. Since the supercells are limited to two primitive cells stacked in each direction, the presented calculations are limited to the study of pure-tin (SnISnI...), pure-germanium (GeIGeI...) and alternating arrays (SnIGeISnIGeI...). Figure 5.4 shows a representative alternating array, that contains iodines of types (iii) and (iv). There are in total four distinct types of bond: d$_S$(GeI), d$_S$(SnI), d$_L$(GeI), d$_L$(SnI), identified in the structure. The graph in Figure 5.4 plots the bond values of each type as a function of cluster composition. As expected, both short and long SnI bonds are more stretched than the respective GeI bonds, although d$_L$(GeI) > d$_S$(SnI). Also, both GeI and SnI short bonds are nearly constant with x and have a small value dispersion for any fixed composition, demonstrating that the alloy environment does not affect these bonds significantly. On the other hand, the long bonds d$_L$ are linearly distorted with x and show a slightly larger dispersion. The weaker metal-halogen interaction of the long bonds should make them more sensible to perturbation. A similar conclusion was given by Stoumpos *et al.* (2015), who observed experimentally that the Cs → MA → FA substitution in AGeI$_3$ perovskites would extend the long bonds as 3.256 → 3.446 → 3.577 [Å], whereas the short bonds remained virtually the same (2.753 → 2.772 → 2.733 [Å]).

Figure 5.5 does the same analysis for the pure-tin and pure-germanium arrays. For the latter, both d$_S$ and d$_L$ show a similar profile to those present in the alternating array. The Sn bonds have a different behavior, with the d$_L$ bonds remaining almost constant, and d$_S$ values slightly decreasing with increased x. The underlying reason for this distinct behavior is that the Sn-centered octahedron is forced to raise its rhombohedral distortion due to a local environment rich in germanium, but at the same time it is constrained to progressively smaller volumes. This causes the d$_L$/d$_S$ ratio to increase. Figure 5.6 (left) shows the evolution of the d$_L$/d$_S$ ratios r$^A_{GeI}$ and r$^A_{SnI}$ for the Ge and Sn octahedra in the alternating array, and r$^P_{GeI}$ and r$^P_{SnI}$ values for the pure arrays. The values of r$^P_{GeI}$, r$^A_{GeI}$ and r$^A_{SnI}$ suffer a linear decrease due to the sensibility of the long bond to the shortening of the lattice constant.

Besides the bond length, a second parameter of interest is the ∠XMX' bond angle, where X and X' are located in opposite vertices of the octahedron centered by M. its value in the ideal cubic structure is 180°, and decreases in the rhombohedral symmetry. For the calculated supercells, the individual angle values show a considerable dispersion. ∠ISnI' values span the range 178°-171°, while ∠IGeI' lie in the lower range of 172°-166°. On the other hand, the average cluster values for all ∠IMI' angles show a much clearer trend.
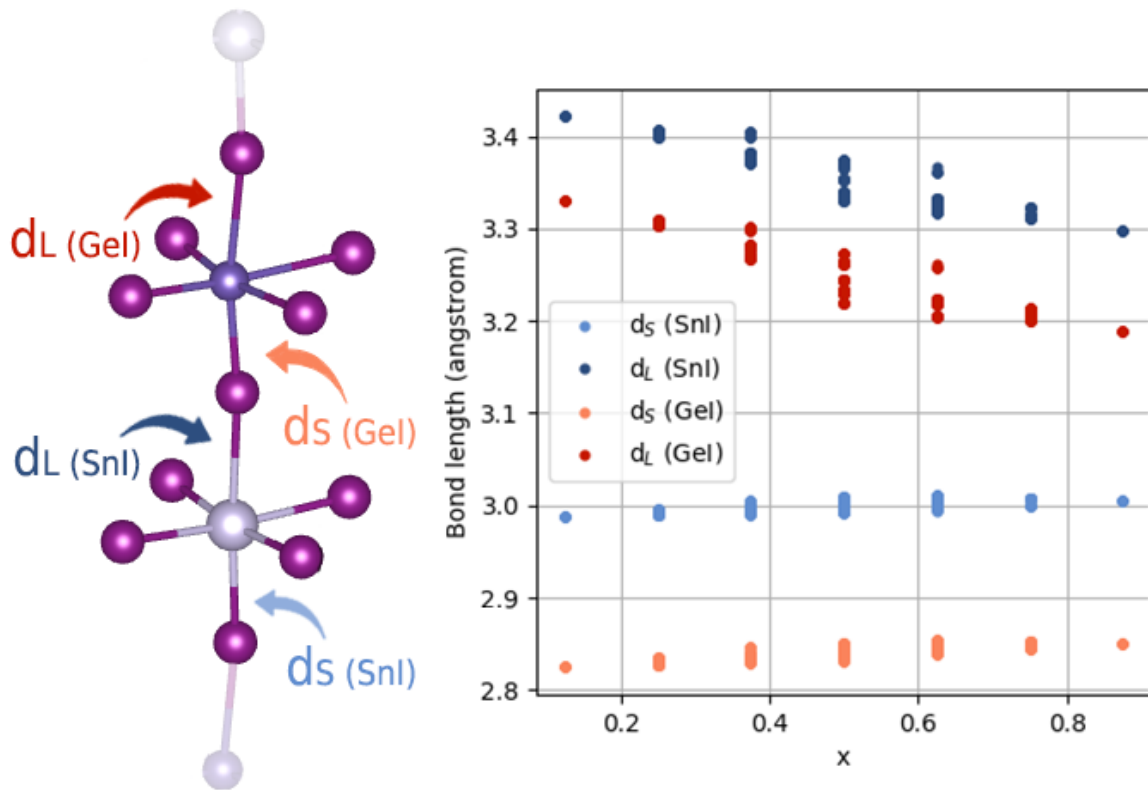
FIGURE 5.4 – The alternating (GeISnI...) array is depicted in the left, highlighting four different types of bonds: $d_{L(GeI)}$, $d_{S(GeI)}$, $d_{L(SnI)}$, and $d_{S(SnI)}$. The graph at the right plots the bond values found in each cluster as a function of composition x.

Figure 5.6 displays the average values as a scatter plot as a function of composition, as well as their GQCA average for T = 300 K.

In this section, the principal geometrical parameters of the rhombohedral CsSn$_{1-x}$Ge$_x$I$_3$ alloy were examined in detail. The Cs cations are seen to be virtually unaffected by the alloying, so the ionic relaxation occurs mainly in the MX lattice. It is shown that the average lattice of the alloy undergoes a continuous transition from cubic to rhombohedral symmetry with increasing x, and that even small tin-rich regions may rapidly transit to the α phase. The MX bonds were found to lie within 8 distinct categories including up to second-neighbor effects, and the evolution and behavior of each type of bond were quantified. At last, the average bonding angle of MX arrays - another parameter of interest for the bandstructure analysis - was described.

5.4   Phase diagram

The insertion of alien metal elements to a pristine perovskite alloy causes a structural perturbation to the immediate surroundings. This is specially true when mixing perovskites which adopt different lattice arrangements at the given temperature. Figure
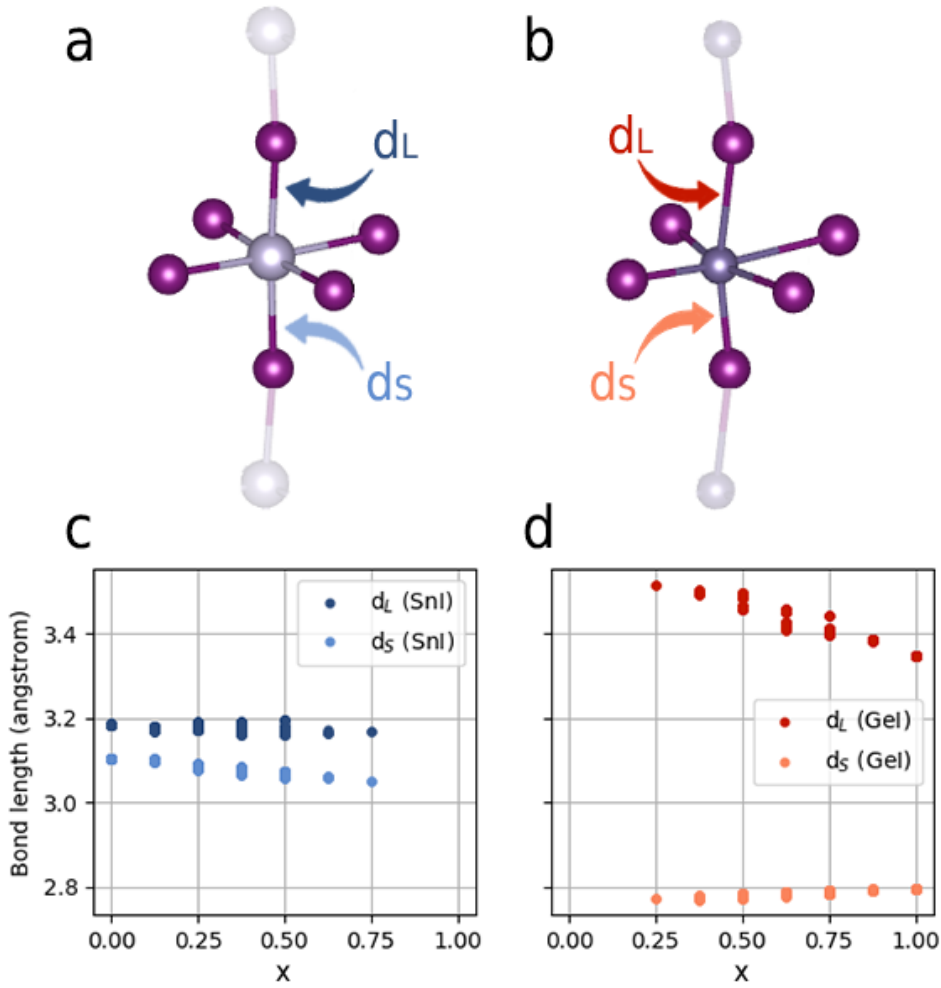
FIGURE 5.5 – (a) SnI and (b) GeI arrays, with corresponding long d$_L$ and short d$_S$ metal-halogen bond distances highlighted in each structure. The graphs in (c) and (d) plots the bond values found in each cluster as a function of composition x.

5.6, for example, shows that, with the insertion of one Ge ion to CsSnI$_3$ (x = 0.125), the bond angle is severely changed. This local strain causes the energy of the mixed supercell to increase in comparison to the linear interpolation between those energies of the pure compounds. It is important to evaluate these excess energies, as defined in Eq. 2.57, for they dictate the alloy mixing thermodynamics.

Figure 5.7 plots the excess energies per metal ion $\Delta\epsilon$ as a function of composition. The profile of the graph is remarkably different from that obtained for the CsPb$_{1-x}$Sn$_x$I$_3$ alloy (Fig. 4.4). In the present case, the excess energies have much higher values, and no cluster shows negative $\Delta\epsilon$, indicating that CsSn$_{1-x}$Ge$_x$I$_3$ is much more susceptible to phase separation. $\Delta\epsilon_j$ peaks at 13.00 meV/metal for j = 7, compared to 2.75 meV/metal of CsPb$_{1-x}$Sn$_x$I$_3$. Guedes *et al.* did similar calculations for methylamonium metal iodide mixed perovskites (GUEDES-SOBRINHO *et al.*, 2019b). Compared to the results of the present study, MAPb$_{1-x}$Sn$_x$I$_3$ has lower $max(\Delta\epsilon)$ than CsSn$_{1-x}$Ge$_x$I$_3$, whereas the

FIGURE 5.6 – (left) Long/short bond ratios found for the octahedrons of every cluster as a function of composition. r^A and r^P correspond to ratios retrieved from the alternating and pure arrays, respectively. (right) Cluster average of ∠IMI' bonding angles as a function of composition, with individual values shown as a scatter plot and the GQCA average at T = 300 K shown as a solid line.
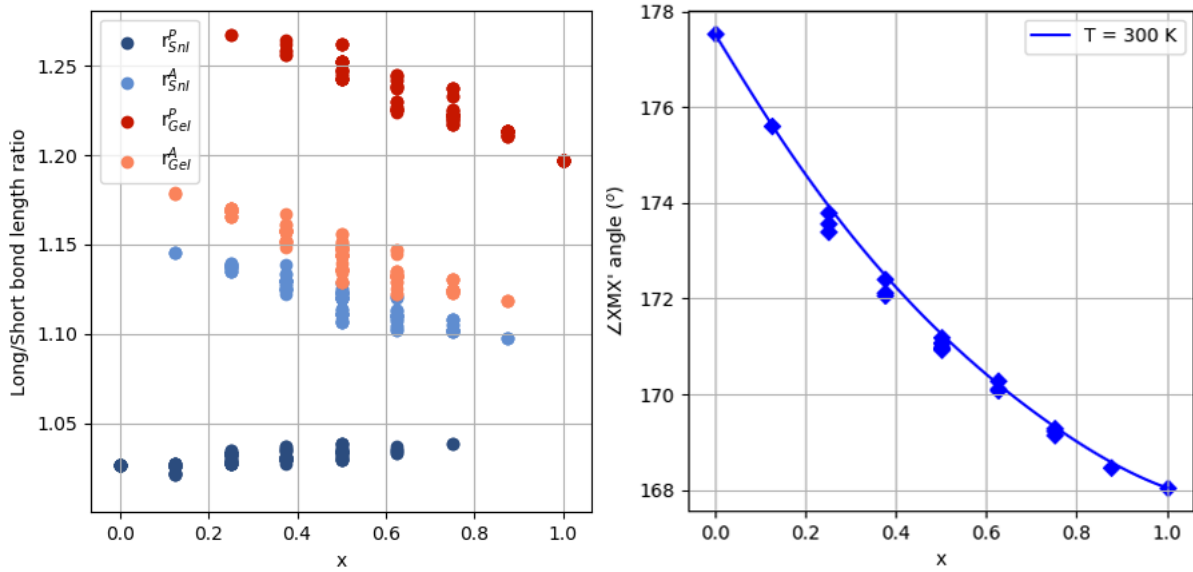
MAPb$_{1-x}$Ge$_x$I$_3$ and MAPb$_{1-x}$Si$_x$I$_3$ alloys have much higher $max(\Delta\epsilon)$ ($\approx$ 30 meV/atom and 60 meV/atom, respectively). These trends can be partially attributed to the unbalance of ionic radius between distinct metal elements. Moreover, the graph in Fig. 5.7 is skewed towards lower values of x, indicating that the tin-rich compositions are more unstable than the Ge-rich regions. The presence of loose long bonds in CsGeI$_3$ possibly allows the lattice to more easily accommodate to the inclusion of ionic species of different sizes.

The mixing free energy ΔF of the alloy is calculated as in Eq. 2.53 for a range of temperatures and is plotted in Figure 5.8. The mixing energy values are entirely positive at temperatures lower than 60 K, indicating complete immiscibility. With increasing temperatures, two local minima appear close to x = 0 and x = 1 as a consequence of the entropy contribution to ΔF, indicating the existence of a well-defined miscibility gap. For the curves at 270 K and 300 K, the two minima are merged together and the second derivative $\partial^2 \Delta F / \partial x^2$ is positive for all x, showing no binodal or spinodal decomposition regions.

The spinodal and binodal points of the mixing free energy were calculated as a function of fabrication temperature. The respective phase diagram is shown in Figure 5.9. A miscibility gap is present for lower temperatures, disappearing above the critical temperature T$_c$ = 258.78 K. As inferred from Fig. 5.7, the Sn-rich compositions are indeed more prone to phase separation than the Ge-rich mixed systems, and the critical temperature is
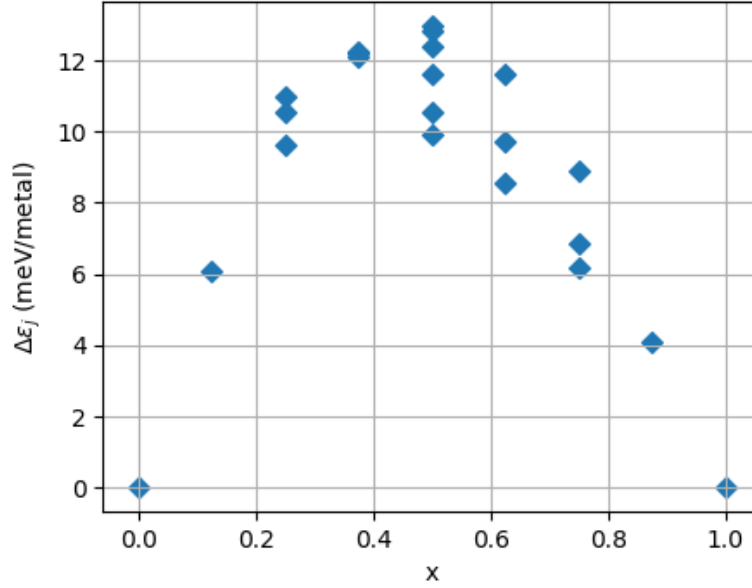
FIGURE 5.7 – Cluster excess energies $\Delta\epsilon_j$ as a function of cluster composition.

observed at the composition x = 0.385. In conclusion, the mixing of CsSnI$_3$ with CsGeI$_3$ is less stable than mixing with CsPbI$_3$, although no phase separation should be observed for CsSn$_{1-x}$Ge$_x$I$_3$ since typically perovskite fabrication methods take place at temperatures higher than T$_c$ (WATTHAGE *et al.*, 2018).

5.5 Electronic Structure

Firstly, the bandstructure calculations were executed for both pure compounds CsSnI$_3$ and CsGeI$_3$ in the two lattice systems. In the case of the rhombohedral lattice, the reciprocal lattice was sampled in the high-symmetry kpoints Γ (0,0,0), L ($\frac{1}{2}$, 0, 0), F ($\frac{1}{2}$, $\frac{1}{2}$, 0) and Z ($\frac{1}{2}$, $\frac{1}{2}$, $\frac{1}{2}$), analogous respectively to the points Γ, X, M and R in the first Brillouin zone of the cubic lattice. The labelling follows the notation of Setyawan and Curtarolo (2010). The CUT parameters of 3.05 a.u. (CsSnI$_3$) and 3.10 a.u. (CsGeI$_3$) for the DFT-1/2 correction were found variationally, resulting in the band gap values displayed in Table 5.3. All materials were identified as having a direct band gap at the ($\frac{1}{2}$, $\frac{1}{2}$, $\frac{1}{2}$) kpoint of the reciprocal space. The experimental and GW band gap values as found in the literature are also shown for comparison.

The DFT-1/2 band gaps are seen to have a good correspondence to GW calculations, especially in the α phase. As seen in Chapter 3, both methods often render comparable results, although in this case there are no experimental data available for evaluating their accuracy. The rhombohedral system shows a gap broadening with relation to the
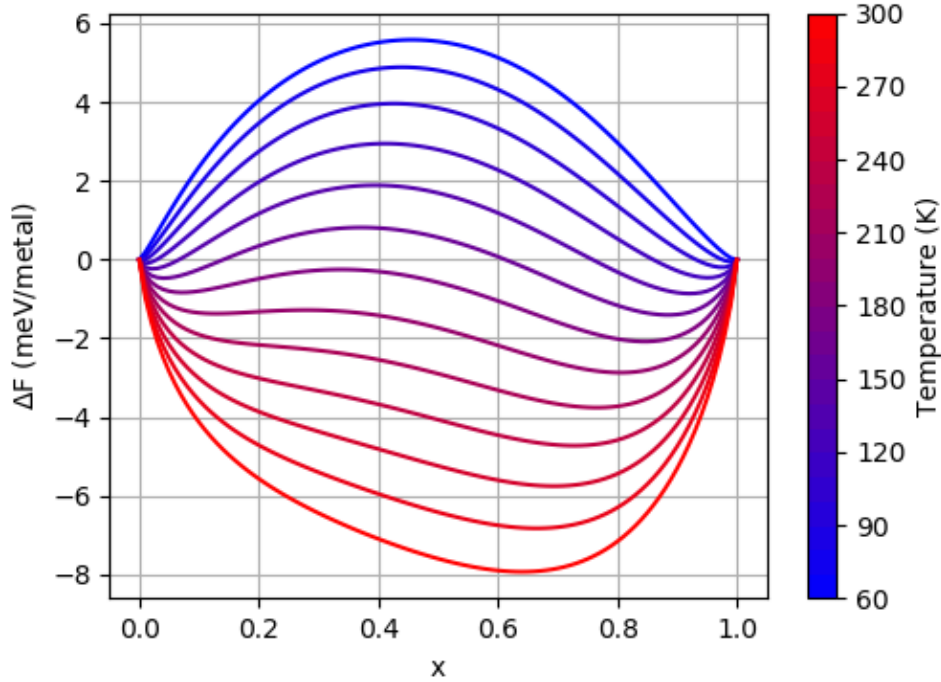
FIGURE 5.8 – Mixing helmholtz free energy ΔF(x) of the alloy for temperature values ranging from 60 K to 300 K. The spinodal region (positive second derivative of ΔF(x)) vanishes around 240 K.

cubic structure. For CsSnI$_3$, the band gap broadening is negligible, consistent with both structures being very similar (see Table 5.2). In the case of rhombohedral CsGeI$_3$, for which optical absorption measurements show a band gap of 1.63 eV, the DFT-1/2 method results in the slightly overestimated value of 1.80 eV, much larger than the cubic value of 1.29 eV. Figure 5.10 shows the DFT-1/2 band diagram of both r- and α-CsGeI$_3$ for comparison. Although the change in lattice system has a considerable impact on the band gap, the general profile of the bandstructure remains almost unaltered.

TABLE 5.3 – *Ab initio* band gap values (DFT, DFT-1/2 and GW) and experimental measurements for CsSnI$_3$ and CsGeI$_3$ in cubic (α) and rhombohedral (r) lattice systems.

Perovskite	DFT	DFT-1/2.	GW	exp.
r-CsGeI3	0.93	1.80	1.619 [a]	1.63 [b]
α-CsGeI3	0.39	1.29	1.199 [a]	
r-CsSnI3	0.08	1.05		
α-CsSnI3	0.07	1.02	1.008 [a]	

[a](HUANG; LAMBRECHT, 2016); [b](KRISHNAMOORTHY *et al.*, 2015)

The broader gap values of r-CsGeI$_3$ compared to the experiment are a consequence of the more severe rhombohedral distortion of the calculated structure when compared to XRD measurements, as shown in Table 5.2. To measure this influence, a r-CsGeI$_3$

FIGURE 5.9 – Phase diagram of CsSn$_{1-x}$Ge$_x$I$_3$ alloy, showing the spinodal and binodal regions in red and blue, respectively. The critical temperature is T$_c$ = 258.78 K and the critical composition is x = 0.385.

primitive cell was artificially designed to meet the experimental parameters, with values of δ = 0.305 Å, $\angle$GeIGe' = 169°, β = 88.62°, a = 5.983 Å, d$_S$ =2.752 Å,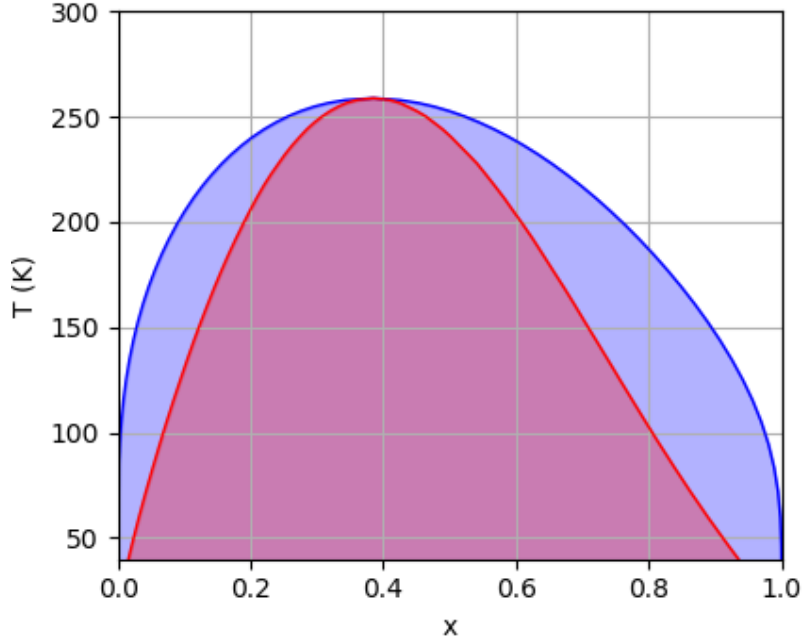 and d$_L$ = 3.258 Å. This configuration resulted in a DFT-1/2 band gap of 1.51 eV (CUT parameter of 3.10 a.u.), smaller and closer to the experimental gap. Comparing the two rhombohedral calculations (gaps of 1.80 eV and 1.51 eV) and the cubic CsGeI$_3$ (gap of 1.29 eV), it is evident a direct relation between gap and distortion.

This relation between structure and band gap can be understood based on the discussions of Chapter 3. Two important structural factors come into play: the bending of $\angle$XMX angles and the increase in the d$_L$/d$_S$ bond ratio. As seen in Table 5.2, the transition from cubic to the rhombohedral system affects the lattice both ways due to the formation of MX$_3$ units. The increase in bond ratio is responsible for destabilizing the CBM energy, while the angle distortion lowers the VBM energy. This conjunction of effects results in a strong band gap opening, as evidenced by the DFT-1/2 data. This is expected to account for a significant part in the band gap evolution in the CsSn$_{1-x}$Ge$_x$I$_3$ alloy, since both effects increase with the inclusion of Ge in the mix (See Figure 5.6).

The rhombohedral deformation is related to that observed for MASiI$_3$ and MASiCl$_3$ perovskites. The increase in long/short bond ratio breaks the nonbonding equilibrium at the CBM, so much so that the X$_p$ orbital character is non-null at the $(\frac{1}{2}, \frac{1}{2}, \frac{1}{2})$ point of the conduction band. Figure 5.11 confirms this comparison: while the cubic lattice character
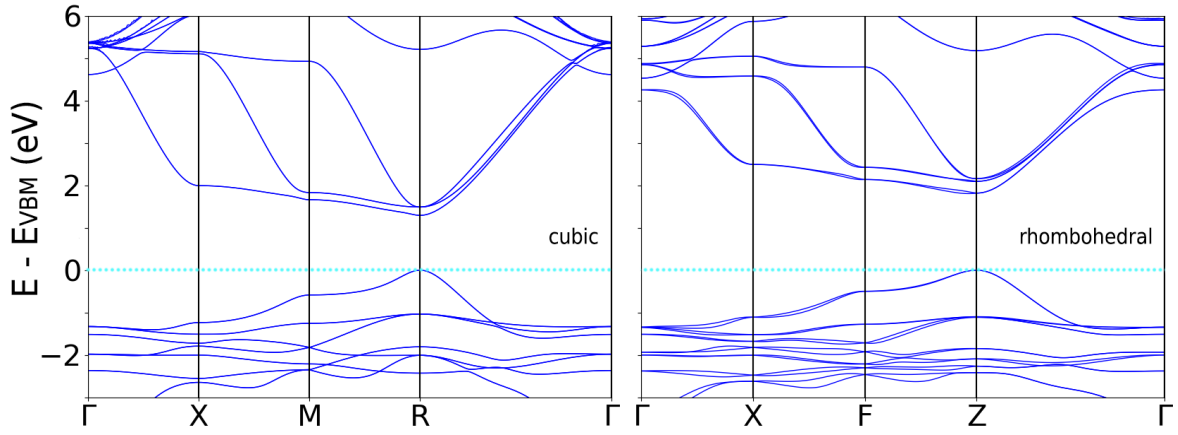
FIGURE 5.10 – Bandstructures of both cubic and rhombohedral CsGeI$_3$, showing the gap broadening suffered from lowering the symmetry.

is similar to the type I profile (defined in Fig. 3.3), the rhombohedral lattice character can be classified into type IV, similarly to MASiI$_3$ and MASiCl$_3$.
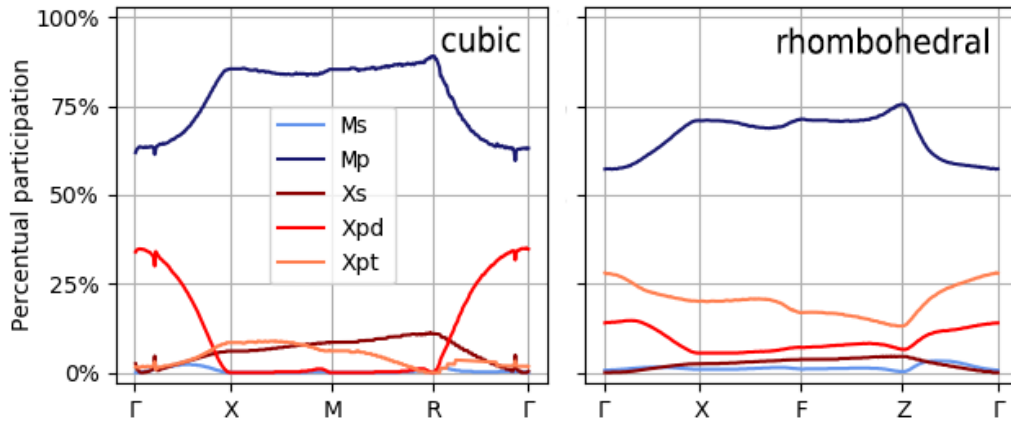
FIGURE 5.11 – Percentual orbital character participation at the conduction band of CsGeI$_3$ in both lattice systems, obtained with DFT-1/2 and SOC corrections. X$_{pd}$ and X$_{pt}$ corresponds to the halogen p orbitals aligned and transversal to the MX segment, respectively. The profile of the rhombohedral structure is similar to that of MASiI$_3$ as shown in Figure 3.3

The band gaps for each CsSn$_{1-x}$Ge$_x$I$_3$ supercell were calculated with SOC and DFT-1/2 corrections. The CUT parameter of 3.07 a.u. was used, an intermediate value between those obtained variationally for the end components. The GQCA average of the cluster values was calculated for T = 300 K, and the results are shown in Figure 5.12. The band gap presents a very well-behaved linear evolution, closely obeying Vegard's law. The dashed line represents an interpolation between the gap values of cubic CsSnI$_3$ and CsGeI$_3$, so the difference between both lines can be attributed to the lattice deformation. Optical absorption measurements in rhombohedral CsSn$_{0.5}$Ge$_{0.5}$I$_3$ found a band gap of 1.5 eV, which is close to the calculated value of 1.41 eV for the same composition (CHEN et

al., 2019). Due to the lack of comprehensive composition-dependent experimental studies, the proper analysis of band gap evolution is limited. Nevertheless, a recent study showed by XRD measurements that CsSn$_{0.7}$Ge$_{0.3}$I$_3$*c* is stable in the orthorhombic phase, and consequently the linearity is expected to break at some point $0.3 \leq x \leq 0.5$ due to the phase transition (QIAN *et al.*, 2020). The band gap curve should then present an upward concavity in the tin-rich region, since γ-CsSnI$_3$ has a band gap of 1.27 eV (HUANG; LAMBRECHT, 2016). Such phase-related nonlinearity was experimentally observed for the MASn$_{1-x}$Ge$_x$I$_3$ perovskite (NAGANE *et al.*, 2018).
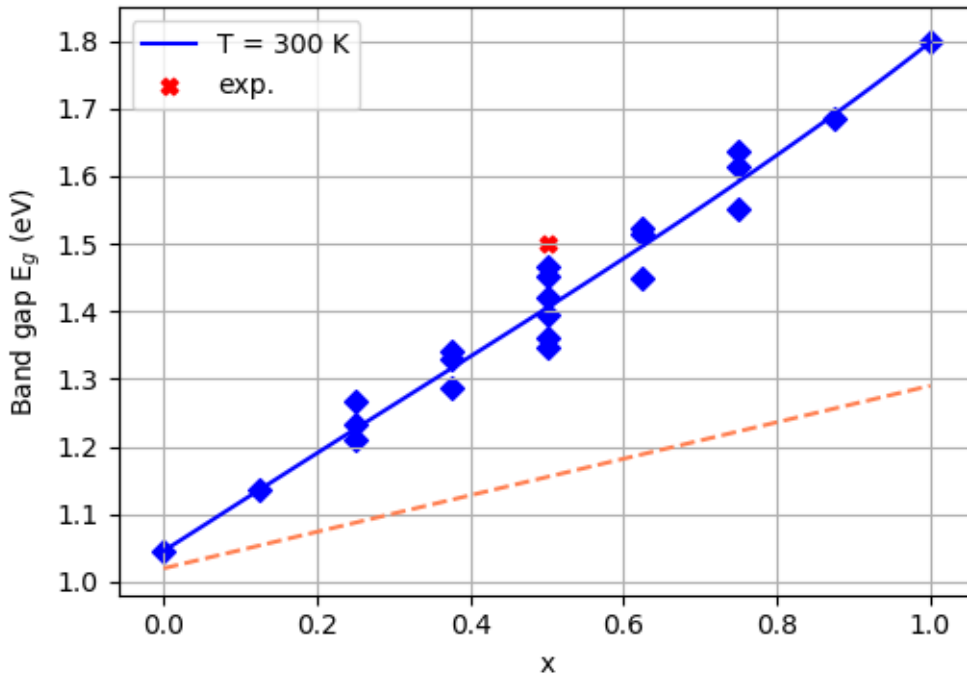
FIGURE 5.12 – Band gap E_g of CsSn$_{1-x}$Ge$_x$I$_3$ as a function of x. The blue data points represent the individual cluster values and the solid curve is their GQCA average at T = 300 K. The red data point is the experimental data for rhombohedral CsSn$_{0.5}$Ge$_{0.5}$I$_3$ (CHEN *et al.*, 2019). The dashed line is a linear interpolation between cubic CsSnI$_3$ and CsGeI$_3$ band gap values, showing the expected behavior in the absence of rhombohedral distortion.

The shape of the band gap evolution of r-CsSn$_{1-x}$Ge$_x$I$_3$ is interestingly in contrast to the gap of the α-CsPb$_{1-x}$Sn$_x$I$_3$ alloy obtained in Chapter 4. While the latter presents a strong bowing with the band gap minimum appearing at intermediate compositions, the former shows the complete absence of this effect. Since the origin of the band gap bowing in the lead-tin mixed perovskites was attributed to the metal signature of the valence and conduction bands, it is fruitful to analyze the M character for CsSn$_{1-x}$Ge$_x$I$_3$ clusters as well.

The average metal character for Sn and Ge ions in both CBM and VBM is shown in Figure 5.13 as a function of x. In both bands, the Sn character is noticeably more present

than Ge, although the difference is much lower in the CBM, possibly due to the proximity of Sn$_p$ and Ge$_p$ atomic energy levels. This prominent Sn character in both bands is a signature consistent with the linear evolution of band energy levels (GOYAL *et al.*, 2018). Neither band is significantly perturbed by the addition of one Ge ion to CsSnI$_3$, and thus its band gaps evolves as expected towards the gap of pristine CsGeI$_3$. This is different of the behavior observed with the addition of one Pb ion, which, in fact, causes the gap to close as a consequence of the strong Pb$_p$ presence in the conduction band (See Fig. 4.9).
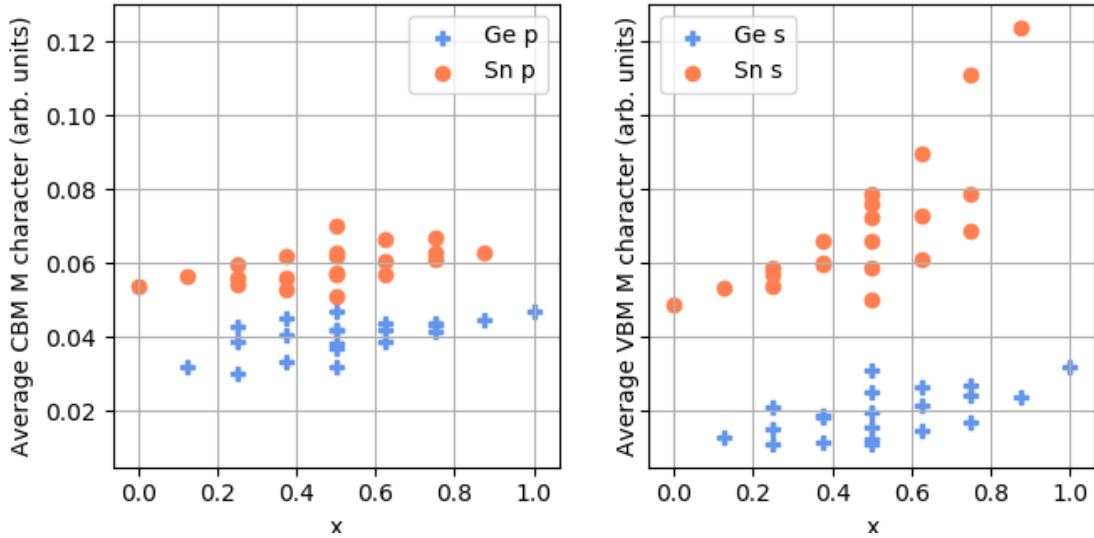
FIGURE 5.13 – M$_p$ (left) and M$_s$ (right) average orbital character per metal at the CBM and VBM, respectively, as a function of x.

On the other extremity of composition, the CsGeI$_3$ bandstructure is more significantly perturbed by addition of tin content, in special its valence band. The inclusion of Sn to CsGeI$_3$ causes a sudden elevation of the VBM energy and a consequent stronger gap narrowing than is expected from a simple linear interpolation. This effect is not too evident in Figure 5.12, which shows a slight upward curvature in the $0.875 \leq x \leq 1.0$ region. But it becomes clear in the second derivative of band gap E$_g$ with respect to composition x. Defining the local bowing b(x) as half the second derivative of E$_g$, the graph of Figure 5.14a shows a sudden increase of this value when the last tin ion is substituted by germanium. The diagram in 5.14b shows the expected band alignment between germanium and tin perovskites that would generate this behavior in the energy levels of the mixed system.

Interestingly, the band gap behavior of CsSn$_{1-x}$Ge$_x$I$_3$ is qualitatively the same of the no-SOC gap of CsPb$_{1-x}$Sn$_x$I$_3$ shown in Fig. 4.11. Both present a similar orbital character in both CBM and VBM, as shown in Fig. 4.12. This correspondence validates the explanation for the band gap trend of both mixed perovskites.
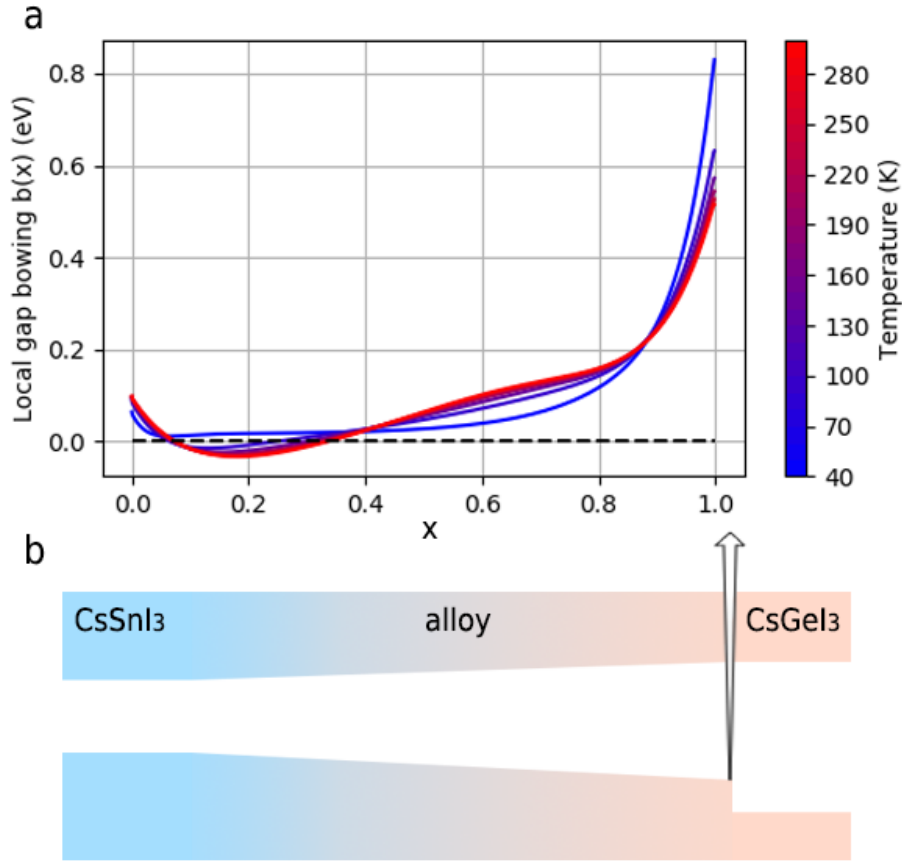
FIGURE 5.14 – (a) Local bowing b(x) for temperature values ranging from 50 K to 300 K. (b) expected band alignment as a function of composition. The abrupt VBM energy shift at x = 0.875 is a possible cause for the appearance of gap bowing for germanium-rich compositions.

5.6   Conclusion

CsSn$_{0.5}$Ge$_{0.5}$I$_3$ has recently been used as the active layer of lead-free solar cells, presenting the relatively high PCE efficiency of 7.1% and an remarkable stability to oxidation. However, no detailed experimental or theoretical study of the optoelectronic characteristics of CsSn$_{1-x}$Ge$_x$I$_3$ were published so far. In this chapter, much of its properties and general behavior were obtained for the first time, generating useful insights to guide future research and the design of photovoltaic devices.

The rhombohedral lattice system was assumed for all calculations, since it is known that CsSn$_{1-x}$Ge$_x$I$_3$ adopts this symmetry in the region of interest x > 0.5. However, it is observed that the system suffers a continuous distortion to the cubic symmetry with decreasing x, due to the higher stability of CsSnI$_3$ in this form with respect to its rhombohedral counterpart. The geometrical parameters a, β, δ, d$_L$, d$_S$ and ∠XMX' were defined and quantified, showing that even small tin-rich regions could rapidly relax

towards the cubic phase. The lattice constant shows a subtle bowing, correlated to the evolution in lattice angle β. The MX bonding distances d$_L$ and d$_S$ were classified into 8 distinct categories regarding their immediate vicinity, each presenting its own length and comportment with x. The Cs cations remain virtually in their ideal positions, not participating in the ionic relaxation process.

The phase stability of the alloy is also studied. The tin-germanium perovskite presents considerably higher values of excess energy than those of the CsPb$_{1-x}$Sn$_x$I$_3$ system. The phase diagram is calculated, showing that the critical temperature of T$_c$ = 258.78 K is lower than ambient and annealing temperatures during perovskite fabrication. The miscibility gap reported is skewed to tin-rich compositions, indicating that the alloy is less susceptible to phase separation for higher values of x. This preference is attributed to the presence of long bonds in the rhombohedral lattice, allowing structural perturbation with low additional cost to energy.

The lattice system adopted was found to be a factor of great importance to the electronic structure of the alloy. The rhombohedral system leads to broader band gaps with relation to the arystotype cubic structure, specially due to d$_L$/d$_S$ bond length ratio and the ∠XMX' angle bending. The effect of these geometrical parameters on the bandstructure was elucidated in terms of orbital interactions at the conduction and valence bands. The band gap of the CsSn$_{1-x}$Ge$_x$I$_3$ alloy was found to follow a linear trend with x, contrasting with the strong bowing of CsPb$_{1-x}$Sn$_x$I$_3$. The differences between both alloys were explored and explained in terms of band alignment.

6 Conclusion

In summary, this dissertation outlines how it is possible to engineer the intrinsic properties of perovskite systems to meet the desired device requirements. It encompasses a myriad of halide perovskite compositions of interest for photovoltaic applications, providing a bird's-eye view on the underlying physics. More than characterizing the proposed systems with *ab initio* calculations, this study explored the uniqueness of each composition and how they relate to each other.

The lattice geometry and band gap of 48 cubic AMX_3 perovskites were reported. This collection included the more common hybrid Pb and Sn halide perovskites and those less studied containing Rb and Si. With the use of the DFT-1/2 correction, the results were close to the experiment and comparable to the state-of-art GW method, thus providing a good description of the bandstructure. Sixteen cases have suitable band gaps for single-junction solar cells, whereas other compositions can be useful to integrate varied layers of tandem cells. The systems share common orbital characteristics in both the valence and conduction bands. It was then shown how their energy levels could be tuned by either enhancing or reducing orbital overlap in the MX_3 network. It was further demonstrated how the choices on composing elements influence the band gap in terms of their spin-orbit coupling magnitude, electronegativity, ionic radius, and orbital overlap. Ultimately, the partial or complete formation of pyramidal MX_3 units was identified as the cause of unexpectedly high band gaps in some perovskites.

With the knowledge acquired and in the light of previous literature, some compositions were selected for constituting promising mixed perovskites. With the objective of efficiently studying these materials, three programs were developed in Python to (1) reduce the number of supercell calculations using symmetry considerations, (2) coordinate the VASP executions, and (3) post-process the output information to retrieve the alloy's properties. The high-throughput solutions were designed to be user-friendly and applicable to multinary alloys of arbitrary composition and lattice geometry. These will be useful in future works of the group on diverse semiconducting systems.

The first studied alloy was α-$CsPb_{1-x}Sn_xI_3$. It has been reported in previous literature as a remarkably stable perovskite in terms of phase and thermal degradation, as well as

oxidation. The structural disorder was identified as a simple relaxation of MX bond lengths, without significant bond angle deformation. No tendency for phase separation was found in any mixed composition. Also, there is a slight energetic preference for configurations with evenly distributed Pb and Sn cations, which are also more resistant to oxidation. The band gap was obtained for all values of x and compared to other tin-lead alloys found in the literature. This class of mixed perovskites is known for presenting a strong gap bowing, and some hypotheses for its origin were ranked and analyzed. The bowing was found to be caused by a peculiar band alignment between the end components, consequence of the strong SOC in $CsPbI_3$.

Then, the rhombohedral $CsSn_{1-x}Ge_xI_3$ perovskite was analyzed. This perovskite was recently discovered to be stable to oxidation due to the formation of an oxide layer on its surface and was used for building lead-free solar cells with 7.1% efficiency. The DFT calculations showed a very sophisticated relaxation process, with a spontaneous transition from the rhombohedral to the cubic lattice with decreasing x. The phase diagram shows single-phase mixing for fabrication temperatures higher than 259 K. The orbital character and band gap evolution as a function of x were calculated and discussed. The linearity in the band gap of $CsSn_{1-x}Ge_xI_3$ was also explained in terms of band alignment and compared to the case of $CsPb_{1-x}Sn_xI_3$. Such a detailed description of this tin-germanium alloy is reported for the first time.

The field of perovskite photovoltaics is vast and, although not exhaustive, this dissertation provides a significant outlook on the topic of compositional tuning. The systems were carefully studied with reliable and efficient computational tools, and the physics was discussed in detail. The results reported are expected to nurture future works and guide the development and engineering of perovskite solar cells.

Bibliography

ANSARI, M. I. H.; QURASHI, A.; NAZEERUDDIN, M. K. Frontiers, opportunities, and challenges in perovskite solar cells: A critical review. **Journal of Photochemistry and Photobiology C: Photochemistry Reviews**, Elsevier BV, v. 35, p. 1–24, jun. 2018. Disponível em: <https://doi.org/10.1016/j.jphotochemrev.2017.11.002>.

ATAÍDE, C. A. **Combinação de método estatístico e aproximação de quase partícula no estudo do óxido de Zinco e materiais relacionados.** Ph.D. Thesis — Instituto Tecnológico de Aeronáutica, 2016.

AZARHOOSH, P.; MCKECHNIE, S.; FROST, J. M.; WALSH, A.; SCHILFGAARDE, M. van. Research update: Relativistic origin of slow electron-hole recombination in hybrid halide perovskite solar cells. **APL Materials**, AIP Publishing, v. 4, n. 9, p. 091501, set. 2016. Disponível em: <https://doi.org/10.1063/1.4955028>.

BABAYIGIT, A.; ETHIRAJAN, A.; MULLER, M.; CONINGS, B. Toxicity of organometal halide perovskite solar cells. **Nature Materials**, Springer Science and Business Media LLC, v. 15, n. 3, p. 247–251, fev. 2016. Disponível em: <https://doi.org/10.1038/nmat4572>.

BARRETT, J.; BIRD, S. R. A.; DONALDSON, J. D.; SILVER, J. The Mössbauer effect in tin(II) compounds. Part XI. The spectra of cubic trihalogenostannates(II). **J. Chem. Soc. A**, Royal Society of Chemistry (RSC), v. 0, n. 0, p. 3105–3108, 1971. Disponível em: <https://doi.org/10.1039/j19710003105>.

BLOCH, F. Über die quantenmechanik der elektronen in kristallgittern. **Zeitschrift für Physik**, Springer Science and Business Media LLC, v. 52, n. 7-8, p. 555–600, jul. 1929. Disponível em: <https://doi.org/10.1007/bf01339455>.

BLöCHL, P. E. Projector augmented-wave method. **Physical Review B**, American Physical Society (APS), v. 50, n. 24, p. 17953–17979, dez. 1994. Disponível em: <https://doi.org/10.1103/physrevb.50.17953>.

BOKDAM, M.; SANDER, T.; STROPPA, A.; PICOZZI, S.; SARMA, D. D.; FRANCHINI, C.; KRESSE, G. Role of Polar Phonons in the Photo Excited State of Metal Halide Perovskites. **Scientific Reports**, Springer Science and Business Media LLC, v. 6, n. 1, jun. 2016. Disponível em: <https://doi.org/10.1038/srep28618>.

CARMONA-ESPÍNDOLA, J.; GÁZQUEZ, J. L.; VELA, A.; TRICKEY, S. B. Generalized gradient approximation exchange energy functional with correct asymptotic

behavior of the corresponding potential. **The Journal of Chemical Physics**, AIP Publishing, v. 142, n. 5, p. 054105, fev. 2015. Disponível em: <https://doi.org/10.1063/1.4906606>.

CASTELLI, I. E.; GARCÍA-LASTRA, J. M.; THYGESEN, K. S.; JACOBSEN, K. W. Bandgap calculations and trends of organometal halide perovskites. **APL Materials**, AIP Publishing, v. 2, n. 8, p. 081514, ago. 2014. Disponível em: <https://doi.org/10.1063/1.4893495>.

CHEN, A.-B.; SHER, A. (Ed.). **Semiconductor Alloys**. Springer US, 1996. Disponível em: <https://doi.org/10.1007/978-1-4613-0317-6>.

CHEN, M.; JU, M.-G.; GARCES, H. F.; CARL, A. D.; ONO, L. K.; HAWASH, Z.; ZHANG, Y.; SHEN, T.; QI, Y.; GRIMM, R. L.; PACIFICI, D.; ZENG, X. C.; ZHOU, Y.; PADTURE, N. P. Highly stable and efficient all-inorganic lead-free perovskite solar cells with native-oxide passivation. **Nature Communications**, Springer Science and Business Media LLC, v. 10, n. 1, jan. 2019. Disponível em: <https://doi.org/10.1038/s41467-018-07951-y>.

CHEN, Q.; MARCO, N. D.; YANG, Y. M.; SONG, T.-B.; CHEN, C.-C.; ZHAO, H.; HONG, Z.; ZHOU, H.; YANG, Y. Under the spotlight: The organic–inorganic hybrid halide perovskite for optoelectronic applications. **Nano Today**, Elsevier BV, v. 10, n. 3, p. 355–396, jun. 2015. Disponível em: <https://doi.org/10.1016/j.nantod.2015.04.009>.

COMBESCOT, M.; SHIAU, S.-Y.; VOLIOTIS, V. Spin-orbit coupling: Atom versus semiconductor crystal. **Physical Review B**, American Physical Society (APS), v. 99, n. 24, jun. 2019. Disponível em: <https://doi.org/10.1103/physrevb.99.245202>.

CRESPO, C. T. The effect of the halide anion on the optical properties of lead halide perovskites. **Solar Energy Materials and Solar Cells**, Elsevier BV, v. 195, p. 269–273, jun. 2019. Disponível em: <https://doi.org/10.1016/j.solmat.2019.03.023>.

DING, X.; CAI, M.; LIU, X.; DING, Y.; LIU, X.; WU, Y.; HAYAT, T.; ALSAEDI, A.; DAI, S. Enhancing the phase stability of inorganic α-CsPbI$_3$ by the bication-conjugated organic molecule for efficient perovskite solar cells. **ACS Applied Materials & Interfaces**, American Chemical Society (ACS), v. 11, n. 41, p. 37720–37725, out. 2019. Disponível em: <https://doi.org/10.1021/acsami.9b12579>.

EPERON, G. E.; LEIJTENS, T.; BUSH, K. A.; PRASANNA, R.; GREEN, T.; WANG, J. T.-W.; MCMEEKIN, D. P.; VOLONAKIS, G.; MILOT, R. L.; MAY, R.; PALMSTROM, A.; SLOTCAVAGE, D. J.; BELISLE, R. A.; PATEL, J. B.; PARROTT, E. S.; SUTTON, R. J.; MA, W.; MOGHADAM, F.; CONINGS, B.; BABAYIGIT, A.; BOYEN, H.-G.; BENT, S.; GIUSTINO, F.; HERZ, L. M.; JOHNSTON, M. B.; MCGEHEE, M. D.; SNAITH, H. J. Perovskite-perovskite tandem photovoltaics with optimized band gaps. **Science**, American Association for the Advancement of Science (AAAS), v. 354, n. 6314, p. 861–865, out. 2016. Disponível em: <https://doi.org/10.1126/science.aaf9717>.

EPERON, G. E.; PATERNÒ, G. M.; SUTTON, R. J.; ZAMPETTI, A.; HAGHIGHIRAD, A. A.; CACIALLI, F.; SNAITH, H. J. Inorganic caesium lead iodide perovskite solar cells. **Journal of Materials Chemistry A**, Royal Society of

Chemistry (RSC), v. 3, n. 39, p. 19688–19695, 2015. Disponível em:
<https://doi.org/10.1039/c5ta06398a>.

EPERON, G. E.; STRANKS, S. D.; MENELAOU, C.; JOHNSTON, M. B.; HERZ,
L. M.; SNAITH, H. J. Formamidinium lead trihalide: a broadly tunable perovskite for
efficient planar heterojunction solar cells. **Energy & Environmental Science**, Royal
Society of Chemistry (RSC), v. 7, n. 3, p. 982, 2014. Disponível em:
<https://doi.org/10.1039/c3ee43822h>.

FANG, Z.; SHANG, M.; HOU, X.; ZHENG, Y.; DU, Z.; YANG, Z.; CHOU, K.-C.;
YANG, W.; WANG, Z. L.; YANG, Y. Bandgap alignment of α-CsPbI3 perovskites with
synergistically enhanced stability and optical performance via b-site minor doping.
Nano Energy, Elsevier BV, v. 61, p. 389–396, jul. 2019. Disponível em:
<https://doi.org/10.1016/j.nanoen.2019.04.084>.

FERRARA, C.; PATRINI, M.; PISANU, A.; QUADRELLI, P.; MILANESE, C.;
TEALDI, C.; MALAVASI, L. Wide band-gap tuning in Sn-based hybrid perovskites
through cation replacement: the $FA_{1-x}MA_xSnBr_3$ mixed system. **Journal of
Materials Chemistry A**, Royal Society of Chemistry (RSC), v. 5, n. 19, p. 9391–9395,
2017. Disponível em: <https://doi.org/10.1039/c7ta01668a>.

FERREIRA, L. G.; MARQUES, M.; TELES, L. K. Approximation to density functional
theory for the calculation of band gaps of semiconductors. **Physical Review B**,
American Physical Society (APS), v. 78, n. 12, set. 2008. Disponível em:
<https://doi.org/10.1103/physrevb.78.125116>.

FERREIRA, L. G.; MARQUES, M.; TELES, L. K. Slater half-occupation technique
revisited: the LDA-1/2 and GGA-1/2 approaches for atomic ionization energies and
band gaps in semiconductors. **AIP Advances**, AIP Publishing, v. 1, n. 3, p. 032119,
set. 2011. Disponível em: <https://doi.org/10.1063/1.3624562>.

FEYNMAN, R. P. Forces in molecules. **Physical Review**, American Physical Society
(APS), v. 56, n. 4, p. 340–343, ago. 1939. Disponível em:
<https://doi.org/10.1103/physrev.56.340>.

FILIPPI, C.; UMRIGAR, C. J.; TAUT, M. Comparison of exact and approximate
density functionals for an exactly soluble model. **The Journal of Chemical Physics**,
AIP Publishing, v. 100, n. 2, p. 1290–1296, jan. 1994. Disponível em:
<https://doi.org/10.1063/1.466658>.

GALKOWSKI, K.; MITIOGLU, A.; MIYATA, A.; PLOCHOCKA, P.; PORTUGALL,
O.; EPERON, G. E.; WANG, J. T.-W.; STERGIOPOULOS, T.; STRANKS, S. D.;
SNAITH, H. J.; NICHOLAS, R. J. Determination of the exciton binding energy and
effective masses for methylammonium and formamidinium lead tri-halide perovskite
semiconductors. **Energy & Environmental Science**, Royal Society of Chemistry
(RSC), v. 9, n. 3, p. 962–970, 2016. Disponível em:
<https://doi.org/10.1039/c5ee03435c>.

GOESTEN, M. G.; HOFFMANN, R. Mirrors of bonding in metal halide perovskites.
Journal of the American Chemical Society, American Chemical Society (ACS),
v. 140, n. 40, p. 12996–13010, set. 2018. Disponível em:
<https://doi.org/10.1021/jacs.8b08038>.

GOYAL, A.; MCKECHNIE, S.; PASHOV, D.; TUMAS, W.; SCHILFGAARDE, M. van; STEVANOVIĆ, V. Origin of pronounced nonlinear band gap behavior in lead–tin hybrid perovskite alloys. **Chemistry of Materials**, American Chemical Society (ACS), v. 30, n. 11, p. 3920–3928, maio 2018. Disponível em: <https://doi.org/10.1021/acs.chemmater.8b01695>.

GUEDES-SOBRINHO, D.; GUILHON, I.; MARQUES, M.; TELES, L. K. Relativistic DFT-1/2 calculations combined with a statistical approach for electronic and optical properties of mixed metal hybrid perovskites. **The Journal of Physical Chemistry Letters**, American Chemical Society (ACS), v. 10, n. 15, p. 4245–4251, jul. 2019. Disponível em: <https://doi.org/10.1021/acs.jpclett.9b01499>.

GUEDES-SOBRINHO, D.; GUILHON, I.; MARQUES, M.; TELES, L. K. Thermodynamic Stability and Structural Insights for $CH_3NH_3Pb_{1-x}Si_xI_3$, $CH_3NH_3Pb_{1-x}Ge_xI_3$, and $CH_3NH_3Pb_{1-x}Sn_xI_3$ Hybrid Perovskite Alloys: A Statistical Approach from First Principles Calculations. **Scientific Reports**, Springer Science and Business Media LLC, v. 9, n. 1, jul. 2019. Disponível em: <https://doi.org/10.1038/s41598-019-47192-7>.

GUILHON, I.; KODA, D. S.; FERREIRA, L. G.; MARQUES, M.; TELES, L. K. Approximate quasiparticle correction for calculations of the energy gap in two-dimensional materials. **Physical Review B**, American Physical Society (APS), v. 97, n. 4, jan. 2018. Disponível em: <https://doi.org/10.1103/physrevb.97.045426>.

HAO, F.; STOUMPOS, C. C.; CHANG, R. P. H.; KANATZIDIS, M. G. Anomalous Band Gap Behavior in Mixed Sn and Pb Perovskites Enables Broadening of Absorption Spectrum in Solar Cells. **Journal of the American Chemical Society**, American Chemical Society (ACS), v. 136, n. 22, p. 8094–8099, maio 2014. Disponível em: <https://doi.org/10.1021/ja5033259>.

HEDIN, L. On correlation effects in electron spectroscopies and the GW approximation. **Journal of Physics: Condensed Matter**, IOP Publishing, v. 11, n. 42, p. R489–R528, out. 1999. Disponível em: <https://doi.org/10.1088/0953-8984/11/42/201>.

HELLMANN, V. H. Einführung in die quantenchemie. **Angewandte Chemie**, Wiley, v. 54, n. 11-12, p. 156–156, mar. 1941. Disponível em: <https://doi.org/10.1002/ange.19410541109>.

HOFFMANN, R. How Chemistry and Physics Meet in the Solid State. **Angewandte Chemie International Edition in English**, Wiley, v. 26, n. 9, p. 846–878, set. 1987. Disponível em: <https://doi.org/10.1002/anie.198708461>.

HOHENBERG, P.; KOHN, W. Inhomogeneous electron gas. **Physical Review**, American Physical Society (APS), v. 136, n. 3B, p. B864–B871, nov. 1964. Disponível em: <https://doi.org/10.1103/physrev.136.b864>.

HUANG, L. yi; LAMBRECHT, W. R. L. Electronic band structure trends of perovskite halides: Beyond Pb and Sn to Ge and Si. **Physical Review B**, American Physical Society (APS), v. 93, n. 19, maio 2016. Disponível em: <https://doi.org/10.1103/physrevb.93.195211>.

IM, J.; STOUMPOS, C. C.; JIN, H.; FREEMAN, A. J.; KANATZIDIS, M. G. Antagonism between Spin–Orbit Coupling and Steric Effects Causes Anomalous Band Gap Evolution in the Perovskite Photovoltaic Materials $CH_3NH_3Sn_{1-x}Pb_xI_3$. **The Journal of Physical Chemistry Letters**, American Chemical Society (ACS), v. 6, n. 17, p. 3503–3509, ago. 2015. Disponível em: <https://doi.org/10.1021/acs.jpclett.5b01738>.

JAIN, A.; ONG, S. P.; HAUTIER, G.; CHEN, W.; RICHARDS, W. D.; DACEK, S.; CHOLIA, S.; GUNTER, D.; SKINNER, D.; CEDER, G.; PERSSON, K. A. Commentary: The materials project: A materials genome approach to accelerating materials innovation. **APL Materials**, AIP Publishing, v. 1, n. 1, p. 011002, jul. 2013. Disponível em: <https://doi.org/10.1063/1.4812323>.

JANAK, J. F. Proof that $\partial E/\partial n_i=\epsilon$ in density-functional theory. **Physical Review B**, American Physical Society (APS), v. 18, n. 12, p. 7165–7168, dez. 1978. Disponível em: <https://doi.org/10.1103/physrevb.18.7165>.

KIM, J.; LEE, S.-C.; LEE, S.-H.; HONG, K.-H. Importance of Orbital Interactions in Determining Electronic Band Structures of Organo-Lead Iodide. **The Journal of Physical Chemistry C**, American Chemical Society (ACS), v. 119, n. 9, p. 4627–4634, fev. 2015. Disponível em: <https://doi.org/10.1021/jp5126365>.

KITAZAWA, N.; WATANABE, Y.; NAKAMURA, Y. Optical properties of $CH_3NH_3PbX_3$ (X = halogen) and their mixed-halide crystals. **Journal of Materials Science**, Springer Science and Business Media LLC, v. 37, n. 17, p. 3585–3587, 2002. Disponível em: <https://doi.org/10.1023/a:1016584519829>.

KOHN, W.; SHAM, L. J. Self-consistent equations including exchange and correlation effects. **Physical Review**, American Physical Society (APS), v. 140, n. 4A, p. A1133–A1138, nov. 1965. Disponível em: <https://doi.org/10.1103/physrev.140.a1133>.

KOJIMA, A.; TESHIMA, K.; SHIRAI, Y.; MIYASAKA, T. Organometal Halide Perovskites as Visible-Light Sensitizers for Photovoltaic Cells. **Journal of the American Chemical Society**, American Chemical Society (ACS), v. 131, n. 17, p. 6050–6051, maio 2009. Disponível em: <https://doi.org/10.1021/ja809598r>.

KOLIOGIORGOS, A.; BASKOUTAS, S.; GALANAKIS, I. Electronic and gap properties of lead-free perfect and mixed hybrid halide perovskites: An ab-initio study. **Computational Materials Science**, Elsevier BV, v. 138, p. 92–98, out. 2017. Disponível em: <https://doi.org/10.1016/j.commatsci.2017.06.026>.

KONTOS, A. G.; KALTZOGLOU, A.; SIRANIDI, E.; PALLES, D.; ANGELI, G. K.; ARFANIS, M. K.; PSYCHARIS, V.; RAPTIS, Y. S.; KAMITSOS, E. I.; TRIKALITIS, P. N.; STOUMPOS, C. C.; KANATZIDIS, M. G.; FALARAS, P. Structural stability, vibrational properties, and photoluminescence in CsSnI3 perovskite upon the addition of SnF2. **Inorganic Chemistry**, American Chemical Society (ACS), v. 56, n. 1, p. 84–91, dez. 2016. Disponível em: <https://doi.org/10.1021/acs.inorgchem.6b02318>.

KRESSE, G.; FURTHMüLLER, J. Efficient iterative schemes for ab initio total-energy calculations using a plane-wave basis set. **Physical Review B**, American Physical

Society (APS), v. 54, n. 16, p. 11169–11186, out. 1996. Disponível em:
<https://doi.org/10.1103/physrevb.54.11169>.

KRISHNAMOORTHY, T.; DING, H.; YAN, C.; LEONG, W. L.; BAIKIE, T.; ZHANG,
Z.; SHERBURNE, M.; LI, S.; ASTA, M.; MATHEWS, N.; MHAISALKAR, S. G.
Lead-free germanium iodide perovskite materials for photovoltaic applications. **Journal
of Materials Chemistry A**, Royal Society of Chemistry (RSC), v. 3, n. 47, p.
23829–23832, 2015. Disponível em: <https://doi.org/10.1039/c5ta05741h>.

LEIJTENS, T.; PRASANNA, R.; GOLD-PARKER, A.; TONEY, M. F.; MCGEHEE,
M. D. Mechanism of tin oxidation and stabilization by lead substitution in tin halide
perovskites. **ACS Energy Letters**, American Chemical Society (ACS), v. 2, n. 9, p.
2159–2165, ago. 2017. Disponível em:
<https://doi.org/10.1021/acsenergylett.7b00636>.

LEITE, J.; FERREIRA, L.; PEREIRA, J. A correction to the liberman approximation
for the exchange energy. **Physics Letters A**, Elsevier BV, v. 40, n. 4, p. 315–316, jul.
1972. Disponível em: <https://doi.org/10.1016/0375-9601(72)90588-9>.

LI, B.; ZHANG, Y.; FU, L.; YU, T.; ZHOU, S.; ZHANG, L.; YIN, L. Surface
passivation engineering strategy to fully-inorganic cubic CsPbI3 perovskites for
high-performance solar cells. **Nature Communications**, Springer Science and Business
Media LLC, v. 9, n. 1, p. 1076, mar. 2018. Disponível em:
<https://doi.org/10.1038/s41467-018-03169-0>.

LI, Z.; YANG, M.; PARK, J.-S.; WEI, S.-H.; BERRY, J. J.; ZHU, K. Stabilizing
perovskite structures by tuning tolerance factor: Formation of formamidinium and
cesium lead iodide solid-state alloys. **Chemistry of Materials**, American Chemical
Society (ACS), v. 28, n. 1, p. 284–292, dez. 2015. Disponível em:
<https://doi.org/10.1021/acs.chemmater.5b04107>.

LIN, Z.-G.; TANG, L.-C.; CHOU, C.-P. Study on mid-IR NLO crystals
$CsGe(Br_xCl_{1-x})_3$. **Optical Materials**, Elsevier BV, v. 31, n. 1, p. 28–34, set. 2008.
Disponível em: <https://doi.org/10.1016/j.optmat.2008.01.004>.

LIU, J.; CHEN, K.; KHAN, S. A.; SHABBIR, B.; ZHANG, Y.; KHAN, Q.; BAO, Q.
Synthesis and optical applications of low dimensional metal-halide perovskites.
Nanotechnology, IOP Publishing, v. 31, n. 15, p. 152002, jan. 2020. Disponível em:
<https://doi.org/10.1088/1361-6528/ab5a19>.

LIU, Z.; PETERS, J. A.; STOUMPOS, C. C.; SEBASTIAN, M.; WESSELS, B. W.; IM,
J.; FREEMAN, A. J.; KANATZIDIS, M. G. Heavy metal ternary halides for
room-temperature x-ray and gamma-ray detection. In: FIEDERLE, M.; BURGER, A.;
FRANKS, L.; JAMES, R. B. (Ed.). **Hard X-Ray, Gamma-Ray, and Neutron
Detector Physics XV**. SPIE, 2013. Disponível em:
<https://doi.org/10.1117/12.2022877>.

MAO, X.; SUN, L.; WU, T.; CHU, T.; DENG, W.; HAN, K. First-principles screening
of all-inorganic lead-free ABX_3 perovskites. **The Journal of Physical Chemistry C**,
American Chemical Society (ACS), v. 122, n. 14, p. 7670–7675, mar. 2018. Disponível
em: <https://doi.org/10.1021/acs.jpcc.8b02448>.

MARQUES, M.; TELES, L. K.; SCOLFARO, L. M. R.; LEITE, J. R.; FURTHMüLLER, J.; BECHSTEDT, F. Lattice parameter and energy band gap of cubic $Al_xGa_yIn_{1-x-y}N$ quaternary alloys. **Applied Physics Letters**, AIP Publishing, v. 83, n. 5, p. 890–892, ago. 2003. Disponível em: <https://doi.org/10.1063/1.1597986>.

MARRONNIER, A.; ROMA, G.; BOYER-RICHARD, S.; PEDESSEAU, L.; JANCU, J.-M.; BONNASSIEUX, Y.; KATAN, C.; STOUMPOS, C. C.; KANATZIDIS, M. G.; EVEN, J. Anharmonicity and disorder in the black phases of cesium lead iodide used for stable inorganic perovskite solar cells. **ACS Nano**, American Chemical Society (ACS), v. 12, n. 4, p. 3477–3486, mar. 2018. Disponível em: <https://doi.org/10.1021/acsnano.8b00267>.

MIYATA, A.; MITIOGLU, A.; PLOCHOCKA, P.; PORTUGALL, O.; WANG, J. T.-W.; STRANKS, S. D.; SNAITH, H. J.; NICHOLAS, R. J. Direct measurement of the exciton binding energy and effective masses for charge carriers in organic–inorganic tri-halide perovskites. **Nature Physics**, Springer Science and Business Media LLC, v. 11, n. 7, p. 582–587, jun. 2015. Disponível em: <https://doi.org/10.1038/nphys3357>.

MØLLER, C. K. Crystal Structure and Photoconductivity of Cæsium Plumbohalides. **Nature**, Springer Science and Business Media LLC, v. 182, n. 4647, p. 1436–1436, nov. 1958. Disponível em: <https://doi.org/10.1038/1821436a0>.

MUTALIB, M. A.; LUDIN, N. A.; RUZALMAN, N. A. A. N.; BARRIOZ, V.; SEPEAI, S.; TERIDI, M. A. M.; SU'AIT, M. S.; IBRAHIM, M. A.; SOPIAN, K. Progress towards highly stable and lead-free perovskite solar cells. **Materials for Renewable and Sustainable Energy**, Springer Science and Business Media LLC, v. 7, n. 2, mar. 2018. Disponível em: <https://doi.org/10.1007/s40243-018-0113-0>.

NAGANE, S.; GHOSH, D.; HOYE, R. L. Z.; ZHAO, B.; AHMAD, S.; WALKER, A. B.; ISLAM, M. S.; OGALE, S.; SADHANALA, A. Lead-free perovskite semiconductors based on germanium–tin solid solutions: Structural and optoelectronic properties. **The Journal of Physical Chemistry C**, American Chemical Society (ACS), v. 122, n. 11, p. 5940–5947, fev. 2018. Disponível em: <https://doi.org/10.1021/acs.jpcc.8b00480>.

NAM, J. K.; CHUN, D. H.; RHEE, R. J. K.; LEE, J. H.; PARK, J. H. Methodologies toward efficient and stable cesium lead halide perovskite-based solar cells. **Advanced Science**, Wiley, v. 5, n. 8, p. 1800509, jun. 2018. Disponível em: <https://doi.org/10.1002/advs.201800509>.

NOH, J. H.; IM, S. H.; HEO, J. H.; MANDAL, T. N.; SEOK, S. I. Chemical management for colorful, efficient, and stable inorganic–organic hybrid nanostructured solar cells. **Nano Letters**, American Chemical Society (ACS), v. 13, n. 4, p. 1764–1769, mar. 2013. Disponível em: <https://doi.org/10.1021/nl400349b>.

NREL. Best research-cell efficiency chart. Access date: 2020. Disponível em: <https://www.nrel.gov/pv/insights/assets/pdfs/cell-pv-eff-emergingpv.pdf>.

OGOMI, Y.; MORITA, A.; TSUKAMOTO, S.; SAITHO, T.; FUJIKAWA, N.; SHEN, Q.; TOYODA, T.; YOSHINO, K.; PANDEY, S. S.; MA, T.; HAYASE, S. $CH_3NH_3Sn_xPb_{1-x}I_3$ Perovskite Solar Cells Covering up to 1060 nm. **The Journal of Physical Chemistry Letters**, American Chemical Society (ACS), v. 5, n. 6, p. 1004–1011, mar. 2014. Disponível em: <https://doi.org/10.1021/jz5002117>.

OHL, R. S. **Light-sensitive electric device**. U.S. Patent 2443542, 27 May 1941.

ONG, S. P.; RICHARDS, W. D.; JAIN, A.; HAUTIER, G.; KOCHER, M.; CHOLIA, S.; GUNTER, D.; CHEVRIER, V. L.; PERSSON, K. A.; CEDER, G. Python materials genomics (pymatgen): A robust, open-source python library for materials analysis. **Computational Materials Science**, Elsevier BV, v. 68, p. 314–319, fev. 2013. Disponível em: <https://doi.org/10.1016/j.commatsci.2012.10.028>.

PERDEW, J. P.; BURKE, K.; ERNZERHOF, M. Generalized gradient approximation made simple. **Physical Review Letters**, American Physical Society (APS), v. 77, n. 18, p. 3865–3868, out. 1996. Disponível em: <https://doi.org/10.1103/physrevlett.77.3865>.

PISANU, A.; MAHATA, A.; MOSCONI, E.; PATRINI, M.; QUADRELLI, P.; MILANESE, C.; ANGELIS, F. D.; MALAVASI, L. Exploring the Limits of Three-Dimensional Perovskites: The Case of $FAPb_{1-x}Sn_xBr_3$. **ACS Energy Letters**, American Chemical Society (ACS), v. 3, n. 6, p. 1353–1359, maio 2018. Disponível em: <https://doi.org/10.1021/acsenergylett.8b00615>.

PRASANNA, R.; GOLD-PARKER, A.; LEIJTENS, T.; CONINGS, B.; BABAYIGIT, A.; BOYEN, H.-G.; TONEY, M. F.; MCGEHEE, M. D. Band gap tuning via lattice contraction and octahedral tilting in perovskite materials for photovoltaics. **Journal of the American Chemical Society**, American Chemical Society (ACS), v. 139, n. 32, p. 11117–11124, ago. 2017. Disponível em: <https://doi.org/10.1021/jacs.7b04981>.

PROTESESCU, L.; YAKUNIN, S.; BODNARCHUK, M. I.; KRIEG, F.; CAPUTO, R.; HENDON, C. H.; YANG, R. X.; WALSH, A.; KOVALENKO, M. V. Nanocrystals of Cesium Lead Halide Perovskites ($CsPbX_3$, X = Cl, Br, and I): Novel Optoelectronic Materials Showing Bright Emission with Wide Color Gamut. **Nano Letters**, American Chemical Society (ACS), v. 15, n. 6, p. 3692–3696, fev. 2015. Disponível em: <https://doi.org/10.1021/nl5048779>.

QIAN, F.; HU, M.; GONG, J.; GE, C.; ZHOU, Y.; GUO, J.; CHEN, M.; GE, Z.; PADTURE, N. P.; ZHOU, Y.; FENG, J. Enhanced Thermoelectric Performance in Lead-Free Inorganic $CsSn_{1-x}Ge_xI_3$ Perovskite Semiconductors. **The Journal of Physical Chemistry C**, American Chemical Society (ACS), abr. 2020. Disponível em: <https://doi.org/10.1021/acs.jpcc.0c00459>.

QIAN, J.; XU, B.; TIAN, W. A comprehensive theoretical study of halide perovskites ABX3. **Organic Electronics**, Elsevier BV, v. 37, p. 61–73, out. 2016. Disponível em: <https://doi.org/10.1016/j.orgel.2016.05.046>.

QUARTI, C.; MOSCONI, E.; ANGELIS, F. D. Structural and electronic properties of organo-halide hybrid perovskites from ab initio molecular dynamics. **Physical Chemistry Chemical Physics**, Royal Society of Chemistry (RSC), v. 17, n. 14, p. 9394–9409, 2015. Disponível em: <https://doi.org/10.1039/c5cp00599j>.

RAJAGOPAL, A.; STODDARD, R. J.; HILLHOUSE, H. W.; JEN, A. K.-Y. On understanding bandgap bowing and optoelectronic quality in Pb–Sn alloy hybrid perovskites. **Journal of Materials Chemistry A**, Royal Society of Chemistry (RSC), v. 7, n. 27, p. 16285–16293, 2019. Disponível em: <https://doi.org/10.1039/c9ta05308e>.

RAY, D.; CLARK, C.; PHAM, H. Q.; BORYCZ, J.; HOLMES, R. J.; AYDIL, E. S.; GAGLIARDI, L. Computational Study of Structural and Electronic Properties of Lead-Free $CsMI_3$ Perovskites (M = Ge, Sn, Pb, Mg, Ca, Sr, and Ba). **The Journal of Physical Chemistry C**, American Chemical Society (ACS), v. 122, n. 14, p. 7838–7848, mar. 2018. Disponível em: <https://doi.org/10.1021/acs.jpcc.8b00226>.

RITCHIE, H.; ROSER, M. Renewable energy. **Our World in Data**, 2020. Https://ourworldindata.org/renewable-energy.

RüHLE, S. Tabulated values of the Shockley–Queisser limit for single junction solar cells. **Solar Energy**, Elsevier BV, v. 130, p. 139–147, jun. 2016. Disponível em: <https://doi.org/10.1016/j.solener.2016.02.015>.

SABBA, D.; MULMUDI, H. K.; PRABHAKAR, R. R.; KRISHNAMOORTHY, T.; BAIKIE, T.; BOIX, P. P.; MHAISALKAR, S.; MATHEWS, N. Impact of Anionic Br^- Substitution on Open Circuit Voltage in Lead Free Perovskite ($CsSnI_{3-x}Br_x$) solar cells. American Chemical Society (ACS), v. 119, n. 4, p. 1763–1767, jan. 2015. Disponível em: <https://doi.org/10.1021/jp5126624>.

SAHOO, S. K.; MANOHARAN, B.; SIVAKUMAR, N. Introduction: Why perovskite and perovskite solar cells? In: **Perovskite Photovoltaics**. Elsevier, 2018. p. 1–24. Disponível em: <https://doi.org/10.1016/b978-0-12-812915-9.00001-0>.

SALHI, B.; WUDIL, Y.; HOSSAIN, M.; AL-AHMED, A.; AL-SULAIMAN, F. Review of recent developments and persistent challenges in stability of perovskite solar cells. **Renewable and Sustainable Energy Reviews**, Elsevier BV, v. 90, p. 210–222, jul. 2018. Disponível em: <https://doi.org/10.1016/j.rser.2018.03.058>.

SARDASHTI, M. K.; ZENDEHDEL, M.; NIA, N. Y.; KARIMIAN, D.; SHEIKHI, M. High efficiency mapbi₃ perovskite solar cell using a pure thin film of polyoxometalate as scaffold layer. **ChemSusChem**, Wiley, v. 10, n. 19, p. 3773–3779, ago. 2017. Disponível em: <https://doi.org/10.1002/cssc.201701027>.

SETYAWAN, W.; CURTAROLO, S. High-throughput electronic band structure calculations: Challenges and tools. **Computational Materials Science**, Elsevier BV, v. 49, n. 2, p. 299–312, ago. 2010. Disponível em: <https://doi.org/10.1016/j.commatsci.2010.05.010>.

SHALAN, A. E.; KAZIM, S.; AHMAD, S. Lead-free perovskites: Metals substitution towards environmentally benign solar cell fabrication. **ChemSusChem**, Wiley, v. 12, n. 18, p. 4116–4139, ago. 2019. Disponível em: <https://doi.org/10.1002/cssc.201901296>.

SHANNON, R. D. Revised effective ionic radii and systematic studies of interatomic distances in halides and chalcogenides. **Acta Crystallographica Section A**, International Union of Crystallography (IUCr), v. 32, n. 5, p. 751–767, set. 1976. Disponível em: <https://doi.org/10.1107/s0567739476001551>.

SHARMA, S.; WEIDEN, N.; WEISS, A. Phase Diagrams of Quasibinary Systems of the Type: ABX_3-A'BX_3; ABX_3-AB'X_3, and ABX_3-ABX'₃; X = Halogen. **Zeitschrift für Physikalische Chemie**, Walter de Gruyter GmbH, v. 175, n. Part_1, p. 63–80, jan. 1992. Disponível em: <https://doi.org/10.1524/zpch.1992.175.part_1.063>.

SHER, A.; SCHILFGAARDE, M. van; CHEN, A.-B.; CHEN, W. Quasichemical approximation in binary alloys. **Physical Review B**, American Physical Society (APS), v. 36, n. 8, p. 4279–4295, set. 1987. Disponível em: <https://doi.org/10.1103/physrevb.36.4279>.

STOUMPOS, C. C.; FRAZER, L.; CLARK, D. J.; KIM, Y. S.; RHIM, S. H.; FREEMAN, A. J.; KETTERSON, J. B.; JANG, J. I.; KANATZIDIS, M. G. Hybrid germanium iodide perovskite semiconductors: Active lone pairs, structural distortions, direct and indirect energy gaps, and strong nonlinear optical properties. **Journal of the American Chemical Society**, American Chemical Society (ACS), v. 137, n. 21, p. 6804–6819, maio 2015. Disponível em: <https://doi.org/10.1021/jacs.5b01025>.

STOUMPOS, C. C.; MALLIAKAS, C. D.; KANATZIDIS, M. G. Semiconducting tin and lead iodide perovskites with organic cations: Phase transitions, high mobilities, and near-infrared photoluminescent properties. **Inorganic Chemistry**, American Chemical Society (ACS), v. 52, n. 15, p. 9019–9038, jul. 2013. Disponível em: <https://doi.org/10.1021/ic401215x>.

SUTTON, R. J.; EPERON, G. E.; MIRANDA, L.; PARROTT, E. S.; KAMINO, B. A.; PATEL, J. B.; HöRANTNER, M. T.; JOHNSTON, M. B.; HAGHIGHIRAD, A. A.; MOORE, D. T.; SNAITH, H. J. Bandgap-Tunable Cesium Lead Halide Perovskites with High Thermal Stability for Efficient Solar Cells. **Advanced Energy Materials**, Wiley, v. 6, n. 8, p. 1502458, fev. 2016. Disponível em: <https://doi.org/10.1002/aenm.201502458>.

SUTTON, R. J.; FILIP, M. R.; HAGHIGHIRAD, A. A.; SAKAI, N.; WENGER, B.; GIUSTINO, F.; SNAITH, H. J. Cubic or Orthorhombic? Revealing the Crystal Structure of Metastable Black-Phase $CsPbI_3$ by Theory and Experiment. **ACS Energy Letters**, American Chemical Society (ACS), v. 3, n. 8, p. 1787–1794, jun. 2018. Disponível em: <https://doi.org/10.1021/acsenergylett.8b00672>.

SWARNKAR, A.; MARSHALL, A. R.; SANEHIRA, E. M.; CHERNOMORDIK, B. D.; MOORE, D. T.; CHRISTIANS, J. A.; CHAKRABARTI, T.; LUTHER, J. M. Quantum dot-induced phase stabilization of α-$CsPbI_3$ perovskite for high-efficiency photovoltaics. **Science**, American Association for the Advancement of Science (AAAS), v. 354, n. 6308, p. 92–95, out. 2016. Disponível em: <https://doi.org/10.1126/science.aag2700>.

SWARNKAR, A.; MIR, W. J.; NAG, A. Can B-Site Doping or Alloying Improve Thermal- and Phase-Stability of All-Inorganic CsPbX3 (X = Cl, Br, I) Perovskites? **ACS Energy Letters**, American Chemical Society (ACS), v. 3, n. 2, p. 286–289, jan. 2018. Disponível em: <https://doi.org/10.1021/acsenergylett.7b01197>.

SWARTWOUT, R.; HOERANTNER, M. T.; BULOVIĆ, V. Scalable deposition methods for large-area production of perovskite thin films. **ENERGY & ENVIRONMENTAL MATERIALS**, Wiley, v. 2, n. 2, p. 119–145, jun. 2019. Disponível em: <https://doi.org/10.1002/eem2.12043>.

TAO, S. X.; CAO, X.; BOBBERT, P. A. Accurate and efficient band gap predictions of metal halide perovskites using the DFT-1/2 method: GW accuracy with DFT expense. **Scientific Reports**, Springer Science and Business Media LLC, v. 7, n. 1, out. 2017. Disponível em: <https://doi.org/10.1038/s41598-017-14435-4>.

THIELE, G.; ROTTER, H. W.; SCHMIDT, K. D. Kristallstrukturen und Phasentransformationen von Caesiumtrihalogenogermanaten(II) $CsGeX_3$ (X = Cl, Br, I). **Zeitschrift fr anorganische und allgemeine Chemie**, Wiley, v. 545, n. 2, p. 148–156, fev. 1987. Disponível em: <https://doi.org/10.1002/zaac.19875450217>.

TROTS, D.; MYAGKOTA, S. High-temperature structural evolution of caesium and rubidium triiodoplumbates. **Journal of Physics and Chemistry of Solids**, Elsevier BV, v. 69, n. 10, p. 2520–2526, out. 2008. Disponível em: <https://doi.org/10.1016/j.jpcs.2008.05.007>.

VALADARES, F. **Development of tools for the ab initio simulation of semiconductor alloys**. Bachelor's Thesis — Instituto Tecnológico de Aeronáutica, dez. 2019.

VOLOSHINOVSKII, A. S.; MYAGKOTA, S. V.; PIDZYRAILO, N. S.; TOKARIVSKII, M. V. Luminescence and structural transformations of $CsSnCl_3$ crystals. **Journal of Applied Spectroscopy**, Springer Science and Business Media LLC, v. 60, n. 3-4, p. 226–228, mar. 1994. Disponível em: <https://doi.org/10.1007/bf02606360>.

WALTERS, G.; SARGENT, E. H. Electro-optic Response in Germanium Halide Perovskites. **The Journal of Physical Chemistry Letters**, American Chemical Society (ACS), v. 9, n. 5, p. 1018–1027, fev. 2018. Disponível em: <https://doi.org/10.1021/acs.jpclett.7b03353>.

WANG, Y.; ZHANG, T.; KAN, M.; ZHAO, Y. Bifunctional stabilization of all-inorganic α-$CsPbI_3$ perovskite for 17% efficiency photovoltaics. **Journal of the American Chemical Society**, American Chemical Society (ACS), v. 140, n. 39, p. 12345–12348, set. 2018. Disponível em: <https://doi.org/10.1021/jacs.8b07927>.

WATTHAGE, S. C.; SONG, Z.; PHILLIPS, A. B.; HEBEN, M. J. Evolution of perovskite solar cells. In: **Perovskite Photovoltaics**. Elsevier, 2018. p. 43–88. Disponível em: <https://doi.org/10.1016/b978-0-12-812915-9.00003-4>.

YAMADA, K.; FUNABIKI, S.; HORIMOTO, H.; MATSUI, T.; OKUDA, T.; ICHIBA, S. Structural Phase Transitions of the Polymorphs of $CsSnI_3$ by Means of Rietveld Analysis of the X-Ray Diffraction. **Chemistry Letters**, The Chemical Society of Japan, v. 20, n. 5, p. 801–804, maio 1991. Disponível em: <https://doi.org/10.1246/cl.1991.801>.

YAMADA, K.; MIKAWA, K.; OKUDA, T.; KNIGHT, K. S. Static and dynamic structures of $CD_3ND_3GeCl_3$ studied by TOF high resolution neutron powder diffraction and solid state NMR. **Journal of the Chemical Society, Dalton Transactions**, Royal Society of Chemistry (RSC), n. 10, p. 2112–2118, abr. 2002. Disponível em: <https://doi.org/10.1039/b201611g>.

YANG, R. X.; TAN, L. Z. Understanding size dependence of phase stability and band gap in CsPbI3 perovskite nanocrystals. **The Journal of Chemical Physics**, AIP Publishing, v. 152, n. 3, p. 034702, jan. 2020. Disponível em: <https://doi.org/10.1063/1.5128016>.

YANG, Z.; ZHANG, X.; YANG, W.; EPERON, G. E.; GINGER, D. S. Tin–lead alloying for efficient and stable all-inorganic perovskite solar cells. **Chemistry of Materials**, American Chemical Society (ACS), v. 32, n. 7, p. 2782–2794, mar. 2020. Disponível em: <https://doi.org/10.1021/acs.chemmater.9b04265>.

YIN, W.-J.; SHI, T.; YAN, Y. Unique properties of halide perovskites as possible origins of the superior solar cell performance. **Advanced Materials**, Wiley, v. 26, n. 27, p. 4653–4658, maio 2014. Disponível em: <https://doi.org/10.1002/adma.201306281>.

YOO, A. B.; JETTE, M. A.; GRONDONA, M. SLURM: Simple Linux Utility for Resource Management. In: **Job Scheduling Strategies for Parallel Processing**. Springer Berlin Heidelberg, 2003. p. 44–60. Disponível em: <https://doi.org/10.1007/10968987_3>.

YU, L.; ZUNGER, A. Identification of potential photovoltaic absorbers based on first-principles spectroscopic screening of materials. **Physical Review Letters**, American Physical Society (APS), v. 108, n. 6, fev. 2012. Disponível em: <https://doi.org/10.1103/physrevlett.108.068701>.

YUAN, Y.; XU, R.; XU, H.-T.; HONG, F.; XU, F.; WANG, L.-J. Nature of the band gap of halide perovskites ABX_3 (A = CH_3NH_3, Cs; B = Sn, Pb; X = Cl, Br, I): First-principles calculations. **Chinese Physics B**, IOP Publishing, v. 24, n. 11, p. 116302, nov. 2015. Disponível em: <https://doi.org/10.1088/1674-1056/24/11/116302>.

ZARICK, H. F.; SOETAN, N.; ERWIN, W. R.; BARDHAN, R. Mixed halide hybrid perovskites: a paradigm shift in photovoltaics. **Journal of Materials Chemistry A**, Royal Society of Chemistry (RSC), v. 6, n. 14, p. 5507–5537, 2018. Disponível em: <https://doi.org/10.1039/c7ta09122b>.

FOLHA DE REGISTRO DO DOCUMENTO

¹· CLASSIFICAÇÃO/TIPO DM	²· DATA DD de mês de YYYY	³· DOCUMENTO N	⁴· N DE PÁGINAS 109

⁵· TÍTULO E SUBTÍTULO:

Compositional tuning of perovskite systems for photovoltaics: an *ab initio* study

⁶· AUTORA(ES):

Fernando Valadares Calheiros de Siqueira

⁷· INSTITUIÇÃO(ÕES)/ÓRGÃO(S) INTERNO(S)/DIVISÃO(ÕES):

Instituto Tecnológico de Aeronáutica – ITA

⁸· PALAVRAS-CHAVE SUGERIDAS PELA AUTORA:

Perovskite, Photovoltaics, Density Functional Theory

⁹· PALAVRAS-CHAVE RESULTANTES DE INDEXAÇÃO:

¹¹· RESUMO:

Haletos de perovskita AMX_3 são semicondutores de alto interesse para aplicações fotovoltaicas, tendo mostrado células solares com eficiência de conversão luminosa comparável à da bem-estabelecida tecnologia de silício. No entanto, ainda há obstáculos na comercialização desses dispositivos, como a necessidade de estabilidade a longo prazo e aperfeiçoamento da absorção luminosa. Comumente, esses problemas são abordados com a substituição completa ou parcial dos elementos nas posições A, M e X da rede cristalina. Nesse trabalho, apresentamos cálculos *ab initio* de uma serie de perovskitas incluindo correção de quasipartícula DFT-1/2 e acoplamento spin-órbita. O objetivo principal é investigar o papel de cada elemento nas propriedades eletrônicas e estruturais e estabilidade de cada material. É reportado o cálculo de 48 perovskitas em fase cúbica (A = CH_3NH_3, $CH(NH_2)_2$, Cs, Rb; M = Pb, Sn, Ge, Si; X = I, Br, Cl), das quais 16 apresentam gap de banda adequados para células solares de junção única. As tendências de gap são então explicados metodicamente com base na rede, no caráter orbital das bandas e na magnitude do acoplamento spin-órbita. Três programas foram criados em Python para o cálculo de alto rendimento de ligas multinárias. Com base no conhecimento adquirido com células puras e nas soluções desenvolvidas, são reportados os cálculos das ligas $CsPb_{1-x}Sn_xI_3$ e $CsSn_{1-x}Ge_xI_3$. Em ambos os casos, a desordem estrutural, estabilidade de fase e a estrutura eletrônica são investigados. No primeiro caso, a forte não-linearidade na evolução do band gap é quantificada e explicada em termos de alinhamento de bandas. Na segunda liga, é observada uma transição contínua entre as simetrias romboédrica e cúbica, afetando diretamente a estabilidade de fase e o gap de banda. Em resumo, esse trabalho aborda sistemas de grande impacto na literatura e de difícil descrição teórica. Desenvolve-se um programa computacional avançado que reúne várias técnicas para a modelagem eficiente de materiais, comparável ao estado da arte. São fornecidos resultados em ótimo acordo com o experimento e previsões confiáveis de novas perovskitas, evidenciando os mecanismos físicos que regem o ajuste de composição dessa classe de semicondutores.

¹²· GRAU DE SIGILO:

(**X**) **OSTENSIVO**   ( ) **RESERVADO**   ( ) **SECRETO**